A Lifting and Actuating Unit for a Planar Nanoprecision Drive System

A Lifting and Actuating Unit for a Planar Nanoprecision Drive System

Dissertation

zur Erlangung des akademischen Grades

Doktoringenieur
(Dr.-Ing.)

vorgelegt der

Fakultät für Maschinenbau der
Technischen Universität Ilmenau

von Herrn

M. Sc. Stephan Gorges
geboren am 18.10.1988 in Ludwigsfelde / Deutschland

Gutachter:

Univ.-Prof. Dr.-Ing. René Theska (Betreuer)
Technische Universität Ilmenau

Dr.-Ing. Christoph Schäffel
IMMS Institut für Mikroelektronik- und Mechatronik-Systeme gemeinnützige GmbH

Univ.-Prof. Dr.-Ing. Bernd Hans Schmidt
Hochschule Hannover

Datum der Einreichung: 10.03.2020

Datum der wissenschaftlichen Aussprache: 18.06.2020

urn:nbn:de:gbv:ilm1-2020000391

Abstract

A central driver in many of today's fields of technology is the miniaturization of electrical, optical and mechanical systems. Multi-axis devices with large travel ranges and extreme precision play a decisive role, not only in measurement and quality assurance, but also in the fabrication and manipulation of nanometer structures. The vertical movement task poses a special challenge, since the gravitational load of the moving object must be compensated permanently. This thesis proposes a vertically lifting and actuating unit and thus contributes to the further development of nanometer precision drive systems.

Basic possible kinematic integration variants are considered and compared according to application relevant criteria. The presented parallel kinematic approach is characterized by its good integrability, its minimal negative influences on the surrounding systems, as well as the distribution of the load to several actuators.
Subsequently, a constructive development process is compiled to further develop this favoured variant. During this process the unit to be developed is integrated into the overall system. Further, its requirements, boundary conditions and subsystems are defined. The vertical actuation consists of two systems: A pneumatic weight force compensation and an electromagnetic precision drive. The technical principle of the lifting unit is developed and the subsystems are arranged in the available design space.
Based on this, a detailed model of the pneumatic actuator is created, its dimensions derived and properties obtained. These dimensions define the spatial limits for the surrounding precision actuator. For the design of this actuator, the force-power ratio is chosen as the objective quantity. Using numerical simulations and optimization, geometries for various topologies are created and evaluated. The most suitable variant is designed and integrated with all other subsystems into one unit. Finally, upcoming steps for integrating the unit into a precision drive system are outlined and possible future applications in the field of nanofabrication are presented.

Zusammenfassung

Ein wesentlicher Treiber in vielen heutigen Technologiebereichen ist die Miniaturisierung von elektrischen, optischen und mechanischen Systemen. Mehrachsige Geräte mit großen Verfahrbereichen und extremer Präzision spielen dabei nicht nur in der Messung und Qualitätssicherung, sondern auch in der Fabrikation und Manipulation von Nanometerstrukturen eine entscheidende Rolle. Die vertikale Bewegungsaufgabe stellt eine besondere Herausforderung dar, da die Schwerkraft des bewegten Objektes permanent kompensiert werden muss. Diese Arbeit schlägt dafür eine Vertikalhub- und -aktuiereinheit vor und trägt damit zur Weiterentwicklung von Nanometer-Präzisionsantriebssystemen bei.

Grundlegende mögliche kinematische Integrationsvarianten werden betrachtet und entsprechend anwendungsrelevanter Kriterien gegenübergestellt. Der gezeigte parallelkinematische Ansatz zeichnet sich durch seine gute Integrierbarkeit, geringe negative Einflüsse auf die umliegenden Systeme, sowie die Verteilung der Last auf mehrere Stellglieder aus.
Folgend wird ein konstruktiver Entwicklungsprozess zusammengestellt, um diese favorisierte Variante weiter auszuarbeiten. Im Laufe dieses Prozesses wird die zu entwickelnde Einheit in das Gesamtsystem eingeordnet und ihre Anforderungen, Randbedingungen und enthaltenen Teilsysteme definiert. Die vertikale Aktuierung besteht dabei aus zwei Systemen: Einer pneumatische Gewichtskraftkompensation und einem elektromagnetischen Präzisionsantrieb. Das technische Prinzip der Hubeinheit wird erstellt und die Teilsysteme im verfügbaren Bauraum angeordnet.
Daraus wird ein detailliertes Modell des pneumatischen Aktors abgeleitet, dieser dimensioniert und dessen Eigenschaften bestimmt. Die Ausdehnung dieses Teilsystems definiert die räumlichen Grenzen für den umliegenden Präzisionsantrieb. Zur Auslegung dieses Antriebs wird das Kraft-Leistungsverhältnis als Zielgröße definiert. Mit Hilfe von numerischer Simulation und Optimierung werden Geometrien für verschiedenste Topologien entworfen und bewertet. Die geeignetste Variante wird mit allen Teilsystemen in eine Einheit integriert und auskonstruiert. Abschließend werden zukünftige Schritte für die Integration der Einheit in ein Präzisionsantriebssystem dargestellt und mögliche Anwendungszenarien in der Nanofabrikation präsentiert.

Danksagung

Bei der Erstellung dieser Arbeit haben mich viele Personen unterstützt, welche ich an dieser Stelle benennen möchte.

Als erstes möchte ich meinem Doktorvater Herrn Univ.-Prof. Dr.-Ing. René Theska für die engagierte Unterstützung und die zahlreichen fruchtbaren Diskussionen danken. Weiterhin wurde mir diese Arbeit erst durch Herrn Dr.-Ing. Christoph Schäffel ermöglicht. Er hat mich stets mit Anregungen und Denkanstöße, sowie im Krankheitsfall sehr unterstützt, wofür ich hier meinen Dank ausdrücken möchte. Herrn Prof. Dr.-Ing. Bernd Hans Schmidt danke ich ebenfalls für die Anregungen und die kritische Durchsicht meiner schriftlichen Ausarbeitung.

Zahlreiche Kollegen standen mir mit Rat und Tat zur Seite: Dankend erwähnen möchte ich Bianca Leistritz für die freundliche und gut gelaunte Gesellschaft am Arbeitsplatz, sowie die anregenden Diskussionen. Steffen Hesse hat mich bei der Prototypenfertigung unterstützt und meine Konstruktion kritisch mit mir diskutiert, wofür ich meinen Dank aussprechen möchte. Bei Michael Katzschmann möchte ich mich für die Diskussionen und die Überprüfung meiner entwickelten Modelle bedanken. Für die Entwicklung der Sensor-Platine möchte ich Sven Engelhardt meinen besonderen Dank ausdrücken.
Peter Frentzel hat bei mir seine Bachelorarbeit absolviert und hat damit einen nennenswerten Beitrag zu dieser Arbeit geleistet. Für seine gelungenen Ausarbeitungen möchte ich ihm hiermit danken.

Bei den Mitgliedern des Graduiertenkollegs *NanoFab* bedanke ich mich für die freundschaftliche Atmosphäre, unterhaltsame fachliche und fachfremde Diskussionen sowie die gemeinsame Zeit.
Außerdem gilt mein Dank meiner gesamten Familie, welche mich nicht nur bei dieser Arbeit sondern auch während meiner bisherigen wissenschaftlichen Laufbahn stets verständnisvoll unterstützt hat.

Ein ganz besonderer Dank gilt meiner Freundin Katharina Simmen, die mich über die gesamte Dauer der Arbeit sehr aufopferungsvoll unterstützt und motiviert hat.

So it has come to this!

Protip:
If you're not sure what to say, try
"So it has come to this!"
It creates instant dramatic tension
and is a valid observation
in literally any situation.[1]

Randall Munroe: XKCD 1022

[1] *"Come to what?" – "You. Me. This moment."*

Contents

Acronyms

AB air bearing

AC autocollimator

CAD Computer Aided Design

DOF degree of freedom

DUT device under test

FEM Finite Element Method

LAU Lifting and Actuating Unit

LIF laser interferometer

nd non-displaceable

PD planar drive

PM permanent magnet

RMS root mean square

WFC weight force compensation

Symbols

Sign	Description	Unit
A	Surface area	m^2
$\boldsymbol{A}$	System matrix in the state space model	
a	Acceleration	m/s^2
α	Rotational acceleration	$°/s^2$, rad/s^2
B	Magnetic flux density	T
$\boldsymbol{B}$	Input matrix in the state space model	
b	Critical pressure ratio of an orifice	
C	Sonic conductance of a valve	$m^3/(s\,Pa)$, $L/(s\,bar)$
$\boldsymbol{C}$	Output matrix in the state space model	
c	Stiffness of a spring	N/m
c_f	Copper-fill-factor of a coil winding	
$\boldsymbol{D}$	Feedthrough matrix in the state space model	
d	Diameter of a circular shape	m
δ	Short distance, small length deviation	m
ε	Relative eccentricity	
η	Dynamic viscosity	Pa s
F	Mechanical force	N
$F2P$	Ratio between force and power of a drive, see eq. (4.54)	N^2/W
f	Frequency of an oscillator	Hz
$\mathcal{G}$	Transfer function of a system in the frequency domain	dB
g	Local gravitational acceleration	m/s^2
H	Magnetic field strength	A/m
h	Height of a body or volume	m
I	Electric current in a conductor	A
i	Arbitrary counting index	
J	Moment of inertia of a body	$kg\,m^2$

Sign	Description	Unit
j	Jerk	m/s^3
k	Arbitrary constant	
L	Inductance of a coil	H
l	Arbitrary physical length	m
M	Torque	N m
m	Mass of a body or fluid volume	kg
$\dot{m}$	Mass flow of a fluid	kg/s
N	Total number of turns in a coil	
n	Polytropic exponent for polytropic processes	
ω	Angular frequency or angular rotational velocity	rad/s
Φ	Phase of a system in the frequency domain	°, rad
$\mathcal{P}$	Arbitrary point in space	
φ	Rotational or tilting angle	°, rad
ϕ	Rotational or tilting angle	°, rad
π	Ratio of circumference and diameter of a circle	
$\dot{Q}$	Heat flux	W, J/s
R	Electric resistance	Ω
RH	Relative humidity of air	%
R_S	Specific gas constant for an ideal gas: 287.058 J K/kg	J K/kg
r	Radius or radial component in cylinder coordinates	m
ρ	Density of a material	kg/m^3
s	Parameter in the frequency domain	rad/s
s_e	Absolute eccentricity	m
σ	Electrical conductivity of a material	S/m
T	Temperature	°C, K
t	Time	s
U	Electric voltage	V
$\mathcal{U}$	Input of a system in the frequency domain	
u	Input parameter	
$\vec{u}$	Input of a system in the time domain	
V	Volume of a body or fluid	m^3
$\dot{V}$	Volume flow of a fluid	m^3/s, SL/min
v	Velocity of a body or fluid	m/s

Sign	Description	Unit
w	An arbitrary width of an object	m
x	First coordinate in a Cartesian coordinate system	m
$\vec{x}$	State vector of a systems state space representation	
$\mathcal{Y}$	Output of a system in the frequency domain	
y	Second coordinate in a Cartesian coordinate system	m
$\vec{y}$	Output of a system in the time domain	
z	Third coordinate in a Cartesian coordinate system (usually the vertical component)	m

Chapter 1

Introduction to Nanopositioning and Nanomeasuring Devices

In the last decades the development of the society was strongly driven by microtechnology. Nowadays, in almost every area of life devices equipped with microelectronic, micromechanic and microoptic systems are present. Through the expanding capabilities and the rising complexity of these systems the demand for high performance nanopositioning and nanomeasuring technologies rises.
To further increase the performance of micro- and nanosystems the structure size needs to be shrinked more and more. These production processes require very cost intensive facilities, which can only operate economical by outputting very high quantities. Therefore, only large markets can be served; small lot numbers and specialized devices are not attractive.

To address these smaller markets, the process cost needs to be reduced and new fabrication equipment and methods are required [1]. At the same time the industry demands for large objects where the surface is functionalized with nanostructures. These fabrication processes rely heavily on advances in the precision motion devices. New concepts need to be developed and new approaches pursued to further follow the path of the miniaturization.

Thereby, challenges in all fields of engineering arise [2]. First off all, high precision measurement devices are needed. Here, laser interferometers (LIFs) are the most capable systems, which have a very large measurement range of multiple meters with an extremely fine resolutions in the subnano- to picometer range. Unfortunately, with this extreme relative resolution these systems are also very sensitive to disturbances. Therefore, special measures need to be taken to avoid or compensate these disturbances.

Second, the moving object needs to be guided very precisely. An extremely low guideway error and a high stiffness of the interface is required. Thus, a special focus is put on the adjustment methods and mechanisms of these components. Further, the friction force and any hysteresis effects need to be minimized.
Third, the systems, which create the motion forces (actuators) need to be specialized for this task. These forces need to be adjustable in a wide range. The high load of the corresponding stages need to be put in motion, while also very small forces are used to work against tiny disturbances.
Finally, an advanced control system is required which enables the nanometer precision. Therefore, special control methods need to be used which utilize the high precision measurement data to derive the set values for the drive systems.

This thesis focuses especially on the vertical axis of such nanoprecision devices. This axis has a very special load situation. The gravitational force acts permanently on the moving mass, thus it needs to be counteracted constantly. From this additional challenges arise and special efforts need to be made.

1.1 State of the Art

In this section some existing devices are presented, which are capable of moving objects in the centi- to decimeter range while positioning them with nanometer repeatability and accuracy [3].

To achieve such precision a very essential measurement principle needs to be obeyed: the *Abbe Comparator Principle*. According to [4] the measurement scale needs to be positioned in line with the measured length. With this setup the systematic sin-error (first order Abbe error) [5] will be avoided. For multi-axis devices every axis has to be set up this way. Furthermore, all measurement lines must also cross in the probe or tool center point to yield an Abbe error free three dimensional measurement composition [6].

Following, a selection of nanopositioning and nanomeasuring devices are presented. A special focus is set on the design of the vertical axis and the respective loads.

Table 1.1: Listing of high precision positioning devices with a three-dimensional addressable volume

Name	Fig. 1.1	Ref.	Year	Range [mm^3]	Guiding
NMM-1	a	[7, 8]	2002	25×25×5	roller
NanoCMM	e	[9]	2007	50×50×4	aeros. & elast.
NANOMEFOS	c	[10, 11]	2009	∅500×150	aeros.
IBS ISARA 400	d	[12–15]	2009	400×400×100	aeros.
TriNano N100	f	[16, 17]	2011	200 cm^3	aeros.
NPMM-200	b	[18, 19]	2013	200×200×25	roller
Mag6D	g	[20]	2015	∅100×0.1	el.mag.

1.1.1 Large Range Nanopositioning and Nanomeasuring Machines and their Vertical Axes

Many nanopositioning systems exist, some of them are available commercially. Especially short range systems with travels in the range of micrometers to a few millimeters are numerous.

This review considers only the major devices with a larger travel range and with active vertical range of motion. All following devices are also listed with their references, travel ranges and guiding methods in table 1.1 and are displayed in fig. 1.1. A extended listing can be found in [21].

NMM-1 One of the first large range nanometer precision devices was the NMM-1 [7], displayed in fig. 1.1a. The overall motion system is set up in a serial way, all three axes of motion are stacked on top of each other. On top a corner mirror is used as reference body for three LIFs which measure its position and two autocollimators which measure its orientation. On all axes roller guidings are used and electromagnetic drives create the driving forces. The overall travel is 25×25 mm^2 in the planar plane and 5 mm in the vertical direction. An adjustable spring system is used to take the static load of the weight of the vertical drives.

NanoCMM The design goal of the NanoCMM [9] from fig. 1.1e was to develop a very dynamic measurement device with very small moving mass and reduced cost of the components. Thus, most parts were made of aluminum. For the 50×50 mm^2 horizontal axes aerostatic bearing pads are used, whereas the

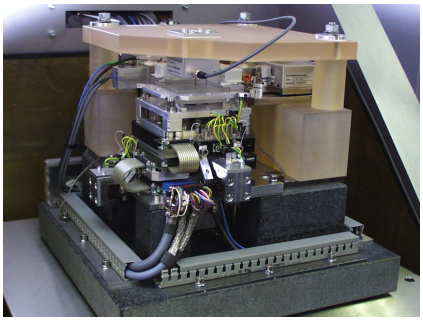

(**a**) NMM-1 [7]

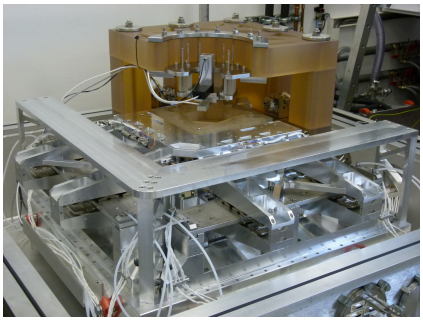

(**b**) NPMM-200 [18]

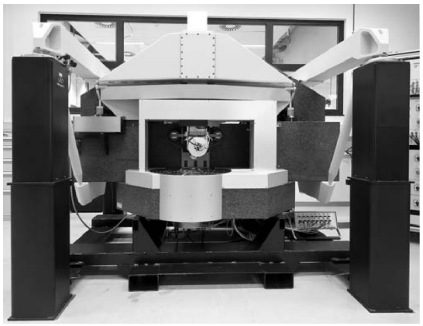

(**c**) Nanomefos [10]

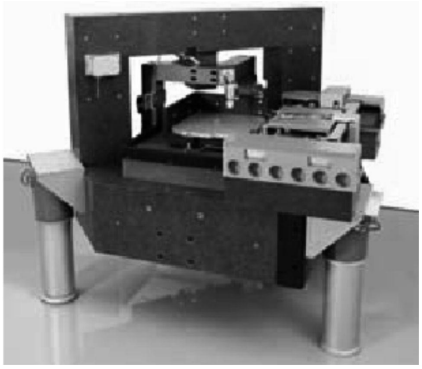

(**d**) Isara 400 [12]

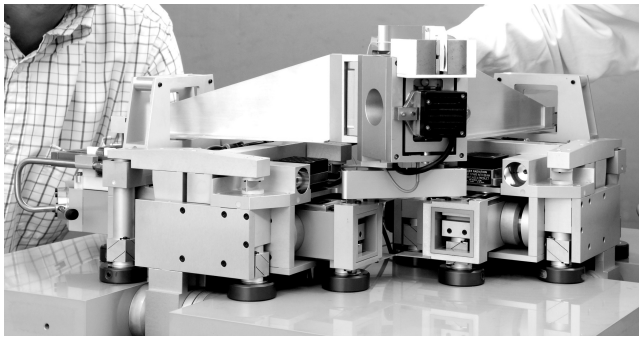

(**e**) NanoCMM [9]

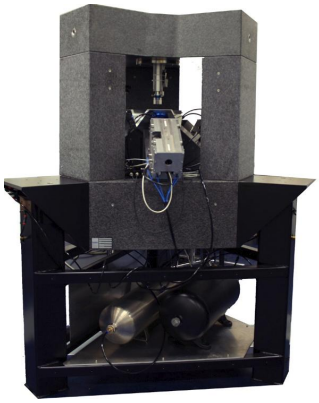

(**f**) TriNano N100 [17]

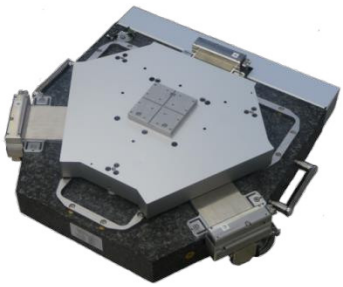

(**g**) Mag6D [20]

Figure 1.1: Photographs of the reviewed high precision positioning devices

vertical 4 mm axis is hinged with elastically deforming elements. The pressurized air is transported to the moving bodies via frictionless extending pipes. All motion is generated via electromagnetic drives, whereas the weight force of the 100 g vertical stage is reduced via lever-spring system.

NANOMEFOS The NANOMEFOS device (see fig. 1.1c) from [10, 11] is specifically designed for non-contact measuring of aspherical and freeform optics with a comparably large diameter of up to ∅500 mm. This sample is placed on a rotary table, whereas the measurement probe moves radial, vertical and can be tilted to face the sample surface. All axes are guided via aerostatic elements and driven with electromagnetic actuators. Further, the radial and vertical axes can be clamped with breaks which allows precise measurements while the sample is rotating. The vertically axis has a travel of 150 mm moves about 85 kg. This static load is taken up by a pneumatic piston. Further developments are presented in [22].

IBS ISARA 400 In [13–15, 23] the development of the IBS ISARA 400 is presented. The prototype of this device is shown in fig. 1.1d. All components are guided with air bearing pads and the driving forces are created by linear electromagnetic direct drives. It has a very large measurement range of 400×400×100 mm³ and is also set up in a mixed way: The sample is put on a two-axial horizontal stage, whereas the probe moves vertically with the whole measurement frame. Therefore, a special lightweight and stiff construction material was needed for this frame. This weight rests on a pneumatic piston setup, thus reducing load on the vertical drives. This piston is integrated into the vertical guiding elements.

TriNano N100 The TriNano N100 device, shown in fig. 1.1f, uses three identical axes which all act in parallel on a common center body, which is shaped like an inverted pyramid [16, 17]. The addressable volume is the upright pyramid above, with 200 cm³. The airguided, electromagnetically driven pushrods are angled upwards and therefore partially lift and translate the sample carrier. Thus, the weight force is distributed between all three drive systems. Each drive unit is fitted with pneumatic elements which carry this load.

NPMM-200 In [18, 19, 24] developments on the successor of the NMM-1 are presented: the NPMM-200, shown in fig. 1.1b. The stacked serial setup of the

roller guidings was maintained but the travel range increased dramatically to 200×200×25 mm³. The horizontal drives were redesigned. Long drive coils are enclosed by permanent magnets, increasing the efficiency. The larger travel requires a larger corner mirror and thus increases the weight of the vertical stage to 25.7 kg. A more advanced compensation mechanism was developed, which takes up these loads. The vertical platform is connected to a steel ribbon which is pulled via a spring. The force is adjusted via the lever length of the ribbon which is wrapped around a shaped disk.
To reduce the disturbing effect of the air on the LIF-measurement beams the system is housed inside a vacuum chamber. Thus, all components need to be vacuum compatible. Because no heat can dissipate into the surrounding air, all drive coils are liquid cooled.

Mag6D A very different approach was taken in [20]. The Mag6D in fig. 1.1g does not have any passive guiding elements, all degrees of freedom are actuated and can be controlled. Therefore, the passive moving body is levitated and driven via electromagnetic forces. The platform can move in the planar range of ∅100 mm and has a lift range of 100 µm. Six long drive coils create the lifting and driving forces on permanent magnets on the moving platform. To lift this 4.2 kg platform solely by electromagnetic forces, high coil currents are needed with result in a high power loss of up to 94 W. Therefore, the coils are housed inside a cooling system. A very advanced control system is required to calculate the six input currents from the desired forces and torques. Basically this device is also vacuum compatible, since no pressurized air is used.

1.1.2 Vertical Actuation Modules

This section describes only devices with a single vertically acting axis, specifically dedicated for micro- and nanopositioning.

Eitzenberger Lifting Module In [25, 27] a lifting module is presented. It is displayed in fig. 1.2a. It has a single axis of motion where aerostatic components are used as guiding elements. An electromagnetic drive with coils and permanent magnets is integrated and combined with a pneumatic piston chamber. Further, it can be seen, that an encoder system is integrated to measure its position. More information, like the maximum load capacity and travel range, is not given.

(**a**) Eitzenberger Lifting Module [25]

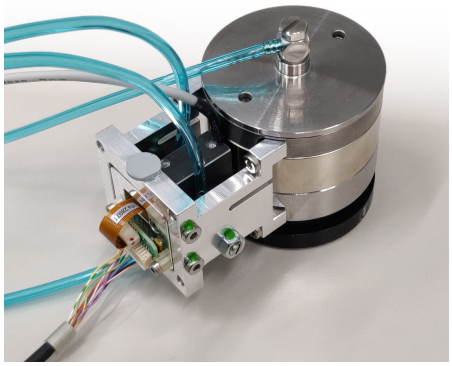

(**b**) *Aerostatisches Führungselement mit integriertem Aktor* [26]

Figure 1.2: Reviewed vertical actuation modules

Aerostatic Guiding Element with Integrated Actuator The module shown in fig. 1.2b is named *Aerostatisches Führungselement mit integriertem Aktor* and was presented in [26]. It is a proof of concept on how a lifting module will influence a planar drive system. It features a vertical travel of 10 mm and was designed to lift loads up to 3.5 kg. The vertical aerostatic guiding is integrated into an electromagnetic drive. Further, a pneumatic piston is also part of the unit. A sensitive linear encoder is used to measure the current travel position. Due to its conceptual design, a very simple electromagnetic drive was implemented. The vertical guiding is not decoupled from the piston chamber, thus these elements possibly influence each other. Most of the tubing and wires connect to the base part which possibly create frictious forces during operation. The very precise encoder requires a complex adjustment mechanism and adjustment procedure. Further, no upper end-stop is integrated, thus the device can separate itself during operation.

1.1.3 The NPPS100 Drive System in Detail

The NPPS100 is a further precision motion platform, shown in fig. 1.3. It is capable of positioning an object in a planar xy-range of ∅100 mm with a root mean square (RMS) error down to 1 nm [28]. Further specifications are listed in table 1.2. Its vertical (z) axis is not actuated. Its design fundamentals were layed out in [29] and following in [28, 30] its development and performance are presented.

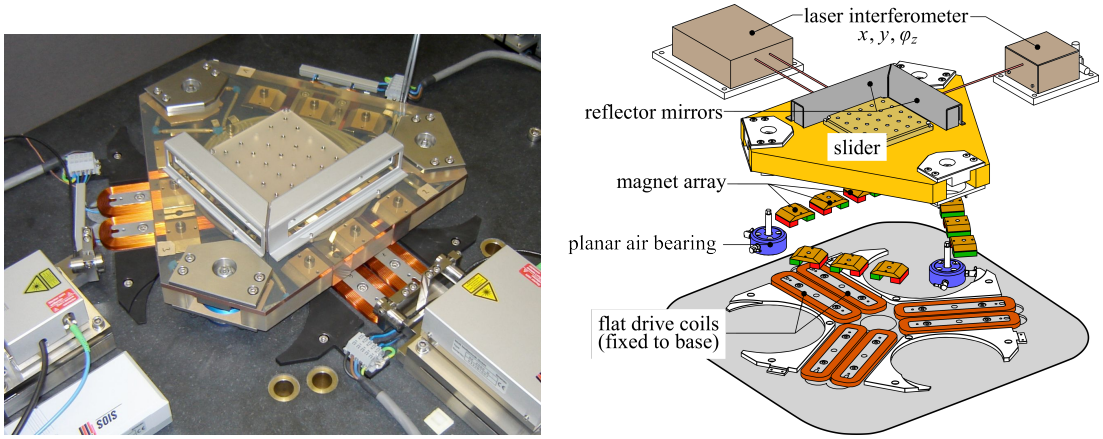

(**a**) Photograph (**b**) Explosional view

Figure 1.3: Photo and explosional view of the NPPS100 planar drive system

The system consists of two main components: The slider, which includes all moving parts and the stator assembly, which includes all frame-fixed components.
Central part of the slider is the monolithic glass-ceramic body. It is shaped like an equilateral triangle with its corners truncated (semi regular hexagon). Two plane mirrors (coated glass-ceramic blocks) are wrung on top of this part. Additionally, the bottom surface of the slider is mirror-coated as well. All three mirror surfaces are perpendicular to each other, forming a corner mirror. Inside the corner mirror a specimen carrier allows the fixation of a test sample. Three frame-fixed LIFs are used to measure their distance to the corresponding mirror

Table 1.2: Specifications of the NPPS100

Specification	Value
xy-range	∅100 mm
Moving mass (slider)	9 kg
Maximum sample mass	1 kg
Maximum acceleration	250 mm/s^2
Maximum velocity	100 mm/s
Resolution in x, y, z	10 pm
Resolution in φ_x, φ_y	65 nrad
Resolution in φ_z	5 nrad
RMS in x, y	≈1.3 nm
RMS in φ_z	15 nrad

surface. Each LIF has a position resolution of 10 pm. From these distance signals the spatial position (x, y, z) of the slider can be calculated. The virtual extension of the x-, y- and z-beams behind the mirrors intersect each other perpendicular in one point, thereby fulfilling the Abbe-principle. The y-LIF is constructed as a double beam LIF. Therefore, the rotational angle φ_z can be derived from the length difference between the primary and the parallel secondary laser beam. An autocollimator is mounted below the slider, next to the z-LIF. Both systems utilize the bottom mirror to measure the vertical position z and the two tilting angles φ_x, φ_y. Since the slider body with the mirrors forms the reference for all spatial measurement devices Zerodur was chosen as the material, because of its thermal expansion coefficient being close to zero [31]. Because of the same material of mirrors and slider body, the already small thermal expansion of these parts will be equal. Therefore, no special suspension for the mirrors is needed to accommodate for thermal expansion differences.

On all three corners of the slider body an air bearing pad is mounted. These pads have a porous surface, where pressurized air flows out to create an air gap of about 5 µm between the bearing pad and a smooth surface below it, thus acting as a guiding element. Here the Newway S205001 pads [32] are used, which have an additional vacuum port (pressure below atmospheric pressure). By discharging air from that port the guiding is preloaded, therefore the stiffness of the air gap increases. Using these aerostatic guiding elements allows the slider to move virtually frictionless and free of stick-slip effects in the planar xy-plane. The stator, a precision machined block made from natural stone, serves as the reference surface. The natural stone is chosen because it has very little residual stress. Also this body has both a large mechanical and thermal inertia, decreasing the sensitivity to external disturbances. Its mass is about 300 kg. Further, all other non-moving components are fixed to it. The whole stator is seated on top of a damped machine bed, which weights about 3 tons. The NPPS100 is situated in a laboratory and is set up under a cover, enclosing the measurement space. The cover reduces acoustic noise and air flow from the outside.
The slider body is connected to the air bearing pads via cardan joints. These are necessary to allow the pads to adjust initially to the their individual angular difference with the underlying surface. The air bearings are preloaded by the mass of the slider.
On the bottom of the slider, a magnet array is mounted on each edge of the triangular shape. Opposite to each magnet array a pair of long, flat drive coils is mounted on the stator surface. Together with the corresponding magnet array, each pair of coils forms one drive unit. Since the magnet arrays are passive components, no wires need to be routed to the slider. The tubing for the air supply

are the only physical connection between slider and stator, reducing friction and hysteresis effects to a minimum.
The signals from all measurement devices are fed into a control system, where the sliders position and orientation, as well as their time derivatives, are calculated. This control system controls all six drive coils via purpose-built analog current controllers. A planar controller is implemented to achieve the low position noise in x and y. The rotational angle around the z-axis φ_z is permanently controlled to zero. An angle above $\pm 1.5'$ would result in the laser beams not reflecting back into their LIFs and therefore losing the respective position signal [33].

1.2 Motivation and Goals

The stators surface of the NPPS100 is machined with a flatness error of 1 µm. This means that all points of the surface deviate vertically (positive or negative direction) from a perfect middle plane by a maximum of 0.5 µm, resulting in the total deviation range 1 µm. This is the economical limit for machining such large surfaces with todays technology. Additional static and dynamic deflections may occur. Therefore, this reference plane will be imperfect, introducing a guideway error into the slider. The slider will tilt and deviate in the vertical direction slightly, while moving over this stator surface [34]. Figure 1.4 illustrates the tilting of the slider for the worst case situation in a simplified two-dimensional model (neglecting the pad and gap height). The distance between two air bearing (AB) pads l_{AB} is ≈230 mm (see fig. A.1), therefore a vertical difference Δz_{AB} of 1 µm results in:

$$\sin\left(\varphi_y\right) = \frac{\Delta z_{\mathrm{AB}}}{l_{\mathrm{AB}}} \tag{1.1}$$
$$\varphi_y \approx 1'' \approx 5\,\mu\mathrm{rad}$$

If all bearing pads are at the same height, no tilting error occurs. But the height level can theoretically be anywhere inside the 1 µm flatness range, thus the maximum z-error may be 1 µm.

In [35] the z-error was measured over the full travel region, see fig. 1.5. It can be seen, that the maximum actual peak-to-peak error is about 65 nm.

One future goal is to use the NPPS100 for manufacturing of nanometer-scale structures. The demand from the industry for nanometer-scale structures on

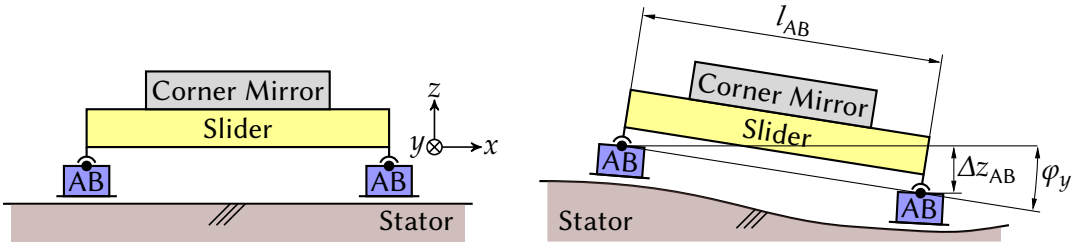

(**a**) Ideal flat surface (**b**) Non flat surface

Figure 1.4: Schematic side view of the NPPS100 slider, showing its idealized representation in (a) and an exaggerated view in (b) of the actual tilting, due to the flatness error of the guiding surface. The air bearings are marked with AB.

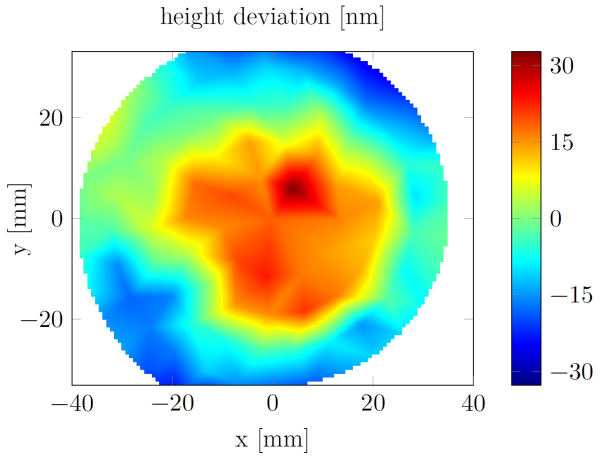

Figure 1.5: Measurement data of the height deviation of the slider over the full Ø100 mm xy-range [35]

macroscopic areas originates mostly from the field of micro stystems technologies. A variety of fabrication methods are conceivable, which can benefit from large travel ranges in all three translational axes. Another domain in need for such structures is the field of precision optics.

To use the NPPS100 as a nanofabrication platform, the vertical error needs to be addressed, to achieve the same precision in z as in x and y. For large range manipulation, such as nanoimprinting on wafers, the tilting errors in φ_x and φ_y could result in incomplete imprinting. A certain travel range in z is needed for the manipulation of non-flat surfaces, such as lenses. A macroscopic vertical travel range will also be advantageous for fabricating on flat objects. By

introducing vertical actuation, the functionality of the NPPS100 in a fabrication environment could be increased, e.g. for loading and unloading a wafer.

1.3 Outline of this Thesis

As stated in the previous section, the NPPS100 needs an actuation system, to compensate the φ_x, φ_y and z-error. Additionally, the z-travel range should be macroscopic so the drive system can be used for nanofabrication.

Therefore, in this work a system should be developed, with which the NPPS100 can be upgraded to precisely move its sample in z and compensate the tilting errors, while minimizing negative effects on the planar drive and the achieved precision. In essence, the currently not actuated three degrees of freedom (DOFs) should be added, to allow a manipulation of the slider in all six DOFs.

In chapter 2 different concepts are investigated on how to upgrade a planar xy-drive to additionally actuate the remaining DOFs. This investigation results in the necessary upgrade: The inclusion of three remaining Lifting and Actuating Units.
Chapter 3 describes the preliminary steps and methodology of the constructive development process and studies the necessary functional components of the Lifting and Actuating Unit.
Mathematical models of the major components are derived and developed in chapter 4. These models are then used to obtain central design parameters from the given loads and requirements.
All these components are integrated into one unit. The shape and dimensions of the necessary mechanical parts, their joining methods and significant design decisions will be presented in chapter 5.
Chapter 6 concludes and evaluates the work from the preceding chapters. Finally, an outlook is given on which fields and topics future work could be conducted to further develop the system under the scope of nanofabrication.

Chapter 2

Methods for Extending a Planar Drive System to 6 Degrees of Freedom

In this chapter the NPPS100 is considered as a rigid body model. Because the measurement system captures all six DOFs of the slider, the focus is set on the guiding and drive system.
The guiding system consists of elementary pairs of parts forming a joint. Each joint allows relative motion in one or multiple spacial directions (translation, rotation). In the bound DOF force or torque is transferred between the two parts. The drive system can be viewed similarly: Between a pair of parts a force, a torque or both can be actively created, acting on both parts with opposing direction.

In general two types of arrangements are known for these pairs: serial and parallel. If two elementary pairs connect from a frame to the same final body it is called parallel arrangement. If one elementary pair connects from the frame to an intermediate body, from which the second pair continues to the final body it is called serial arrangement. Additionally, both methods can also be combined. [36]
Serial arrangements usually have the benefit of allowing a larger travel, because the final body is only constrained by one elementary pair. Whereas parallel arrangements benefit from the additional connections by being stiffer and more dynamic.

Following, the kinematic setup of the NPPS100 is investigated and possible variants on how to integrate the desired additional DOFs are compared.

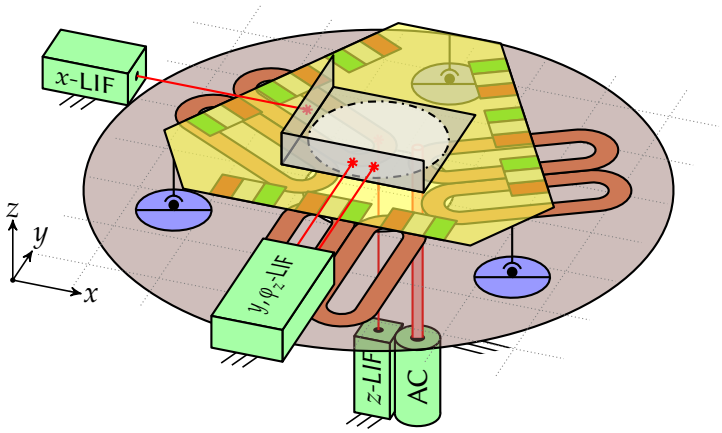

Figure 2.1: Technical principle of the NPPS100

2.1 Existing Planar Drive System

This section investigates the arrangement of the guiding, drive and measurement devices of the NPPS100. In contrast to many coordinate measurement machines the NPPS100 presented in section 1.1.3 is arranged completely parallel, which can be seen from its schematic representation displayed in fig. 2.1.

The yellow truncated triangle represents the slider body, on top of which the corner mirror (three perpendicular gray rectangles) is mounted. Inside the corner mirror a sample or device under test (DUT) can be placed. The circular dashed region depicts the available area of motion, which can be addressed. Around the slider the stator-fixed measurement devices (green boxes and cylinder) are arranged with their measurement beams drawn as red lines. The air bearing pads are shown as blue circles. The stators reference surface is represented by the underlying dark gray circular shape. On this surface three pairs of flat drive coils are shown as long brown rings. Furthermore, the corresponding magnet arrays are shown as green and red rectangles on the underside of the slider.

The functional structure for this drive system can be seen in fig. 2.2. In these block diagrams every box represents a functional component which exchange matter, energy or information with each other [37, 38]. Here the blocks are colored in the corresponding object colors from fig. 2.1.
The solid lines without arrows represent a solid connection between the two components. So all non-moving components are fixed to the stator and all moving components are fixed to the slider. One exception is the planar guiding which interfaces the stator, but not all DOFs are fixed. The solid lines with an

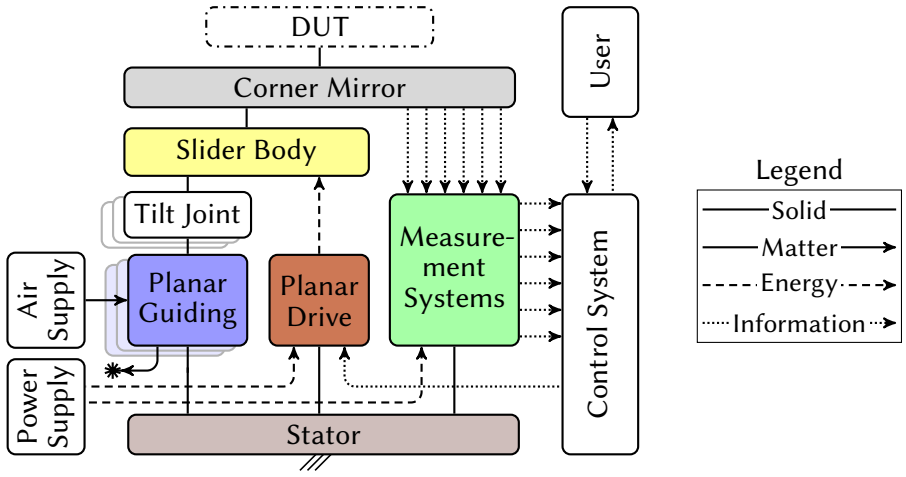

Figure 2.2: Structure with functional elements and their interaction of the NPPS100

arrow display transport of matter, in this case it is always air. The planar guiding (air bearing pads) is supplied with pressurized air and discharges it to the environment during operation. All electric devices, such as the measurement systems and the planar drive, are fed with electrical power from the power supply. The planar drive box, which incorporates the power amplifier, transforms this electric energy to mechanical energy, which acts on the slider. Whereas the measurement systems need the energy for their operation. Transported information is drawn as a dotted line. The measurement systems get their information from the corner mirror then transform and transport it to the control system. This control system sends its set values to the planar drive and communicates about the current state of the machine with the operator.
Matter transport always includes a transport of kinetic energy. The same applies for the transport of information on electric lines. These energy lines are left out to simplify the graph.
In the following sections details on the three functional groups are given.

2.1.1 Measurement System

In fig. 2.3 only the measurement components of the NPPS100 are shown. Three LIFs measure the spacial position coordinates x, y and z of the corner mirror. Whereas the spacial orientation $(\varphi_x, \varphi_y, \varphi_z)$ is determined via an autocollimator (AC) and the y-LIF. It can be seen that all measurement devices are fixed to the

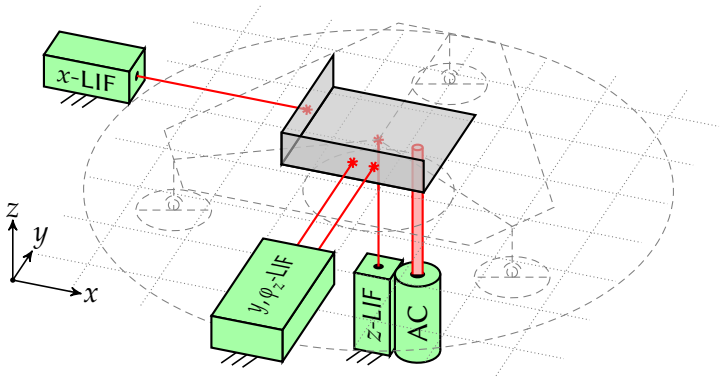

Figure 2.3: Technical principle of all measurement devices of the NPPS100

frame, the stator. Thus, it acts as the machine frame and the metrology frame. Additionally, all six DOFs are measured in parallel to each other.

2.1.2 Guiding System

This section investigates the rigid body model of the guiding system of the NPPS100. In such a model infinitely stiff beams are connected with different kinds of joints. In fig. 2.4 an overview from [39] of all possible elementary joints can be found.
The slider body can be abstracted in the rigid body model in fig. 2.5 as a structure of such infinitely stiff beams.

These beams connect the cardan joints of each air bearing pad to their simplified center of mass. A cardan (or spherical) joint is a joint with three rotational free-

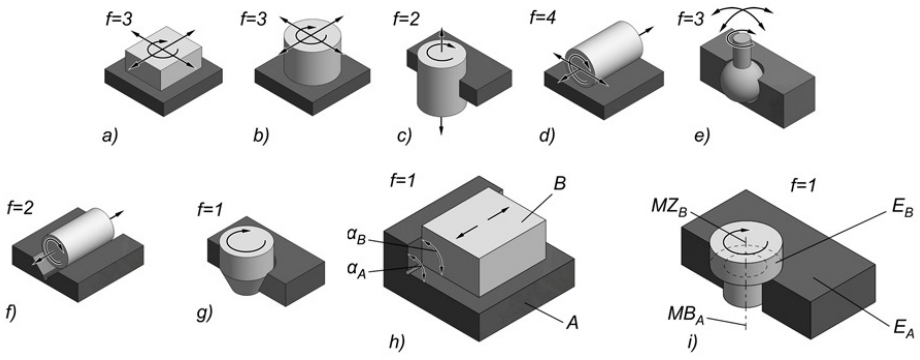

Figure 2.4: Selection of elementary pairs of mechanical joints, from [39]

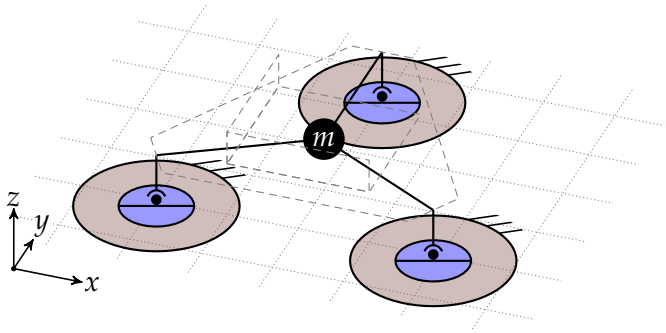

Figure 2.5: Technical guiding principle of the NPPS100

doms, whereas the translational freedoms are constrained to the center of the joint, see fig. 2.4e. Therefore, the bearing pads can rotate around the joint relative to the slider body. The pads (blue circles) represent a joint with translatory freedom in x and y (planar) and rotational freedom around φ_z relative to the reference surface, see fig. 2.4a or b. If the reference surfaces (brown circles) of the three planar guiding elements would be perfectly flat and at the same z-level, the pads could be adjusted in a way so no cardan joints would be required. As soon as one reference surface is slightly tilted or not at the same z-height with the other surfaces, the whole system would be overconstrained and could not move anymore. Thus, each air bearing needs to be able to adjust its orientation to the underlying surface. Depending on the flatness of the reference surface, the air bearings vertical position may change. Therefore, at different positions the slider may tilt around the x- and y-axis, as well as slightly lift or drop along the z-direction.
Overall, the slider is free to move in x, y and φ_z (DOF $= 3$), whereas φ_x, φ_y and z are determined by the reference surface.

2.1.3 Drive System

In fig. 2.6 the drive components of the NPPS100 are displayed. Along each edge on the bottom of the triangular slider a magnet array is fixed. Each magnet array faces a pair of long, flat drive coils which are fixed on the natural stone base. When a coil is energized a Lorentz-force is acting on the electrons which are moving through the magnetic field, created by the permanent magnet arrays. The frame will take up these forces acting on the coils. The reactant forces act on the permanent magnet arrays, which results in a total force and torque on the slider body, therefore directly actuating the corner mirror. Depending on

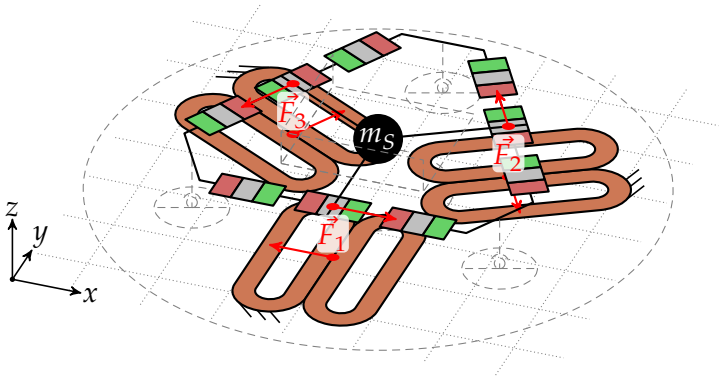

Figure 2.6: Technical principle of the planar drive system of the NPPS100. For each drive unit an exemplary force vector and the respective counter force is shown.

the position of the coil wire inside the magnetic field, the force direction and intensity changes for a given coil current. All coils are controlled in a way that each pair creates no vertical force components. So the resulting force vector has only x- and y-components.
A coil pair and its corresponding magnet array form one drive unit. All three of these drive units act independently and in parallel on the slider body. The drive controller can create drive forces in the xy-plane, as well as torque around the z-axis, by superposing the drive forces from all three drive units. The rotational freedom around the z-axis is controlled to zero by the control system via the torque M_z, thereby effectively locking this DOF of the slider body.

2.2 Variants for Integrating the Additional Freedoms

This section will give a brief overview of the investigated variants, on how to upgrade the planar to a six DOF system. In the NPPS100 all three coordinates and all three orientational angles are already measured, therefore this section will focus on the guiding and drive systems.

To actuate the tilting angles φ_x, φ_y and the vertical position z additional freedoms need to be introduced, as well as drives, which actuate these freedoms. This lifting and tilting system can be introduced at different places in the kinematic order.

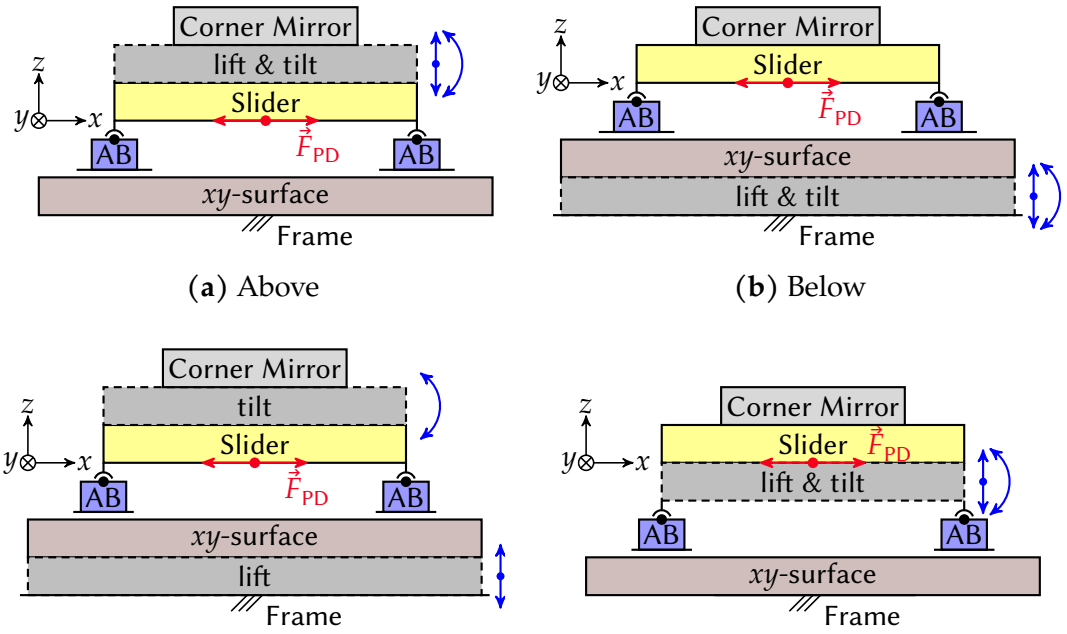

(**a**) Above (**b**) Below

(**c**) Exemplary splitting (**d**) Between

Figure 2.7: Schematics of the four most promising integration variants for the lifting and tilting functionality

There are many possible variants, on where to implement the tilting and lifting functionality in the kinematic order. But there are only three points in the kinematics, where additional DOFs can be integrated. These are:

- Between the corner mirror and the slider body
- Between the slider body and the planar bearing pads
- Between the frame and the planar *xy*-surface of the natural stone base

In this section only the four most promising variants will be investigated. Their implementation is shown in the schematics in fig. 2.7.

The following criteria are used to compare and evaluate the proposed variants:

- The expected performance of the whole system for nanopostitioning and fabrication application
- The complexity of the additional system, which correlates to effort, design expense and price
- The necessary modifications, which need to be made to the existing system

For this evaluation criteria weighting and rating tables are omitted, since it is a preliminary investigation and not the main focus of this thesis.

Figure 2.7a shows a very common approach for upgrading an existing system: the additional freedoms and joints are added on top. Since the corner mirror is the measurement reference, it has to be kept in the last spot of the kinematic chain. Therefore, the tilting and lifting functionality follows after the planar drive, before the corner mirror. From this schematic viewpoint the biggest advantage of this configuration is that the least redesign is necessary. But it would result in separating the corner mirror from the slider. The bottom mirror of the corner mirror is formed by the mirrored bottom surface of the slider body, so it cannot be detatched. Therefore, a new slider and an additional corner mirror would be necessary which is not feasible, since these are two of the most costly components of the NPPS100.

A similar option is to lift and tilt the whole planar system, therefore introducing the new functionality before the planar system (see fig. 2.7b). In this variant the slider does not need to be altered. The major downside is that the xy-surface is part of the natural stone block, which has a large mass. To achieve precision motion in the same order of magnitude as the planar drive, high dynamic positioning of this large inertia is necessary, increasing the load and complexity of the control and power supply systems. Further, by actuating the stone base, unwanted deformations may be introduced, further increasing the flatness error of the reference surface.

Another variant is to introduce parts of the additional DOFs at different locations. Figure 2.7c shows an exemplary schematic. These split-variants are presumably less complex than other variants, since the single subsystems will be integrated at different places and therefore can be designed independently of each other. A large disadvantage in contrast, is that by not combining the lift- and tilt-functions into one unit, more guiding components and discrete masses will exist between the corner mirror and the source of the driving forces. This increases the oscillation sensitivity of the whole system and reduces controllability, which will have negative effects on the achievable precision. Further, to split the functions to different locations either the natural stone block has to be actuated or the corner mirror has to be separated from the slider. Hence, the disadvantages from the previously described variants are adopted.

For the remaining variant in fig. 2.7d the additional devices are integrated between the air bearings and the slider body. The major downside is that when lifting the slider, the permanent magnets of the planar drive move away from the drive coils, decreasing the maximum available drive forces. This disadvantage

is weakened by the fact that for precision positioning the slider the maximum forces are not necessary. The major advantage of this variant is that the design principle of having one rigid body on which all driving forces act can be maintained, increasing the probability of reaching the projected precision goals. Due to these conditions this variant is the most favorable for the application in the NPPS100, therefore its development is pursued in the following section and chapters.

2.3 Details on the Favored Integration Variant

The variant from fig. 2.7d is favorable because of its integrability into the existing drive system. In eq. (1.1) the expected worst case tilting angles were estimated to be approximately 1″. Due to this very minor angular travel requirement, the application of a parallel kinematic setup is very attractive. Therefore, the new system can benefit from the advantages in stiffness and dynamics. The lifting and tilting system will then be composed of multiple Lifting and Actuating Units (LAUs), see fig. 2.8. Since the air bearings are only connected to the lifting unit, they will be incorporated into it.

By paralleling the setup three identical LAUs can be used, simplifying the design and development process, as well as their operation, service and maintenance. Each unit needs to actuate only part of the load and just one DOF (vertical z-position) reducing the design complexity further.

In the following chapter the framework for the constructive development process for one LAU will be layed out.

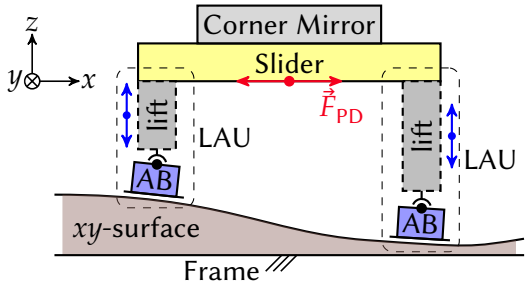

Figure 2.8: Parallel kinematic setup for the lifting and tilting functionality, introducing the Lifting and Actuating Units. By extending the LAUs differently the tilting error can be compensated.

Chapter 3

Framework of the Constructive Development Process for a Lifting and Actuating Unit

This chapter documents the preparatory steps in the constructive development process. This process is not a fixed routine, different guidelines are described in [37–44]. The overall structure is very similar for most listed processes, as can be seen from [45, fig. 3.1].

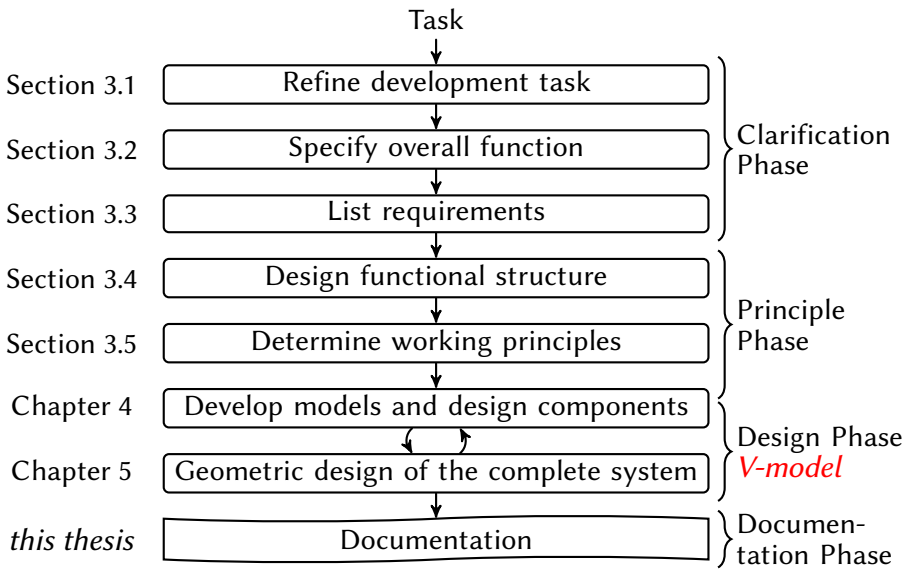

Figure 3.1: The constructive development process used for this development; merged from [39–41].

For the following development of an LAU an adapted process is used, shown in fig. 3.1. Its foundation are the processes from [39] and [40]. Additionally, the V-model from [41] is integrated, since it is very well suited for integrated mechatronic systems, such as the LAU. Especially this V-model is iteratively performed. The first five steps of the whole process are described in the following sections of this chapter, whereas the V-model strategy is applied in chapters 4 and 5.

3.1 Clarification and Definition of the Development Task

The development assignment is to create a drive system with vertical travel in the millimeter range. Three identical units of this system have to be integrable into the slider of the NPPS100, one on every corner. With these additional systems it shall be possible to precisely lift the slider vertically while allowing a precision controlled tilting of it in the range of few angular seconds. During the initialization process of the NPPS100 the LAUs need to be available to tilt the corner mirror in a way that all measurement beams get reflected into their respective sensor housing. While the slider is moving over the stator, the LAUs need to permanently adjust to the stators local surface error. Further, the influence of the LAUs on the existing planar drive should be minimal, to not disrupt the already achieved planar precision. The whole system operates in a laboratory environment. Additionally, the known drawbacks from the second described system in section 1.1.2 (such as lift-off protection, dragging wires and tubing) should be overcome.
The overall functionality of the device might be of use at some other place in the framework of precision positioning devices. So in the future a similar device might be needed e.g. with higher load capacity or larger travel ranges. Hence, it is beneficial to set up the design process in a way, that the intermediate development steps are easy to adapt for future applications. Therefore, this process should result in a set of utilities which simplify altering the design.

3.2 Overall Function

In section 2.1 all major functional components of the planar drive system have been described. Introducing the LAUs results in the functional structure which

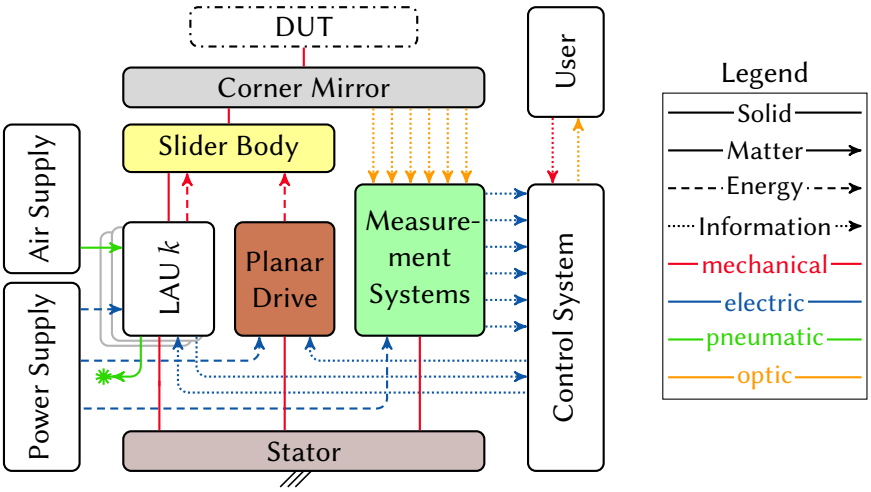

Figure 3.2: Functional structure NPPS100 with included LAUs

is shown in fig. 3.2. The displayed line colors correspond to the physical domains. The major difference to fig. 2.2 is that the air bearing-box is replaced by the LAU, since the bearing pad is incorporated into it. The LAU is supplied with electrical energy which is transformed and put as mechanical energy into the slider. Further, it exchanges information with the control system, which may be data from internal measurements, as well as setpoint information.

From this upgraded graph the overall function for one LAU can be derived. Figure 3.3 shows this blackbox model, including all input and output quantities to the LAU. Compared to the functional structure the connections are listed in a greater detail and include environmental in- and outputs. Again it is distinguished between matter, energy and information transport. In this case not the matter or energy type is written but the most significant parameter of the used effect. Furthermore, the thermal domain is introduced with purple lines.

At first glance one can see, that there are many input quantities. This is due to the nature of precision devices being very sensitive. A lot of surrounding parameters can possibly have an effect on the device, both positive and negative, therefore they are taken into account. Further the system is set up in a laboratory environment, where a lot of other devices and energy sources are available, but not all drawn inputs have to be used.
The first and most important input is the signal representing the force F_{set}, which is the vertical force of the LAU, requested by the external control system. The next inputs arise from the connection to the NPPS100 drive system. The main load on the LAU will be the inertia of the slider with the DUT on it. This total inertia is represented by the mass m_S and moment of inertia J_S. Further,

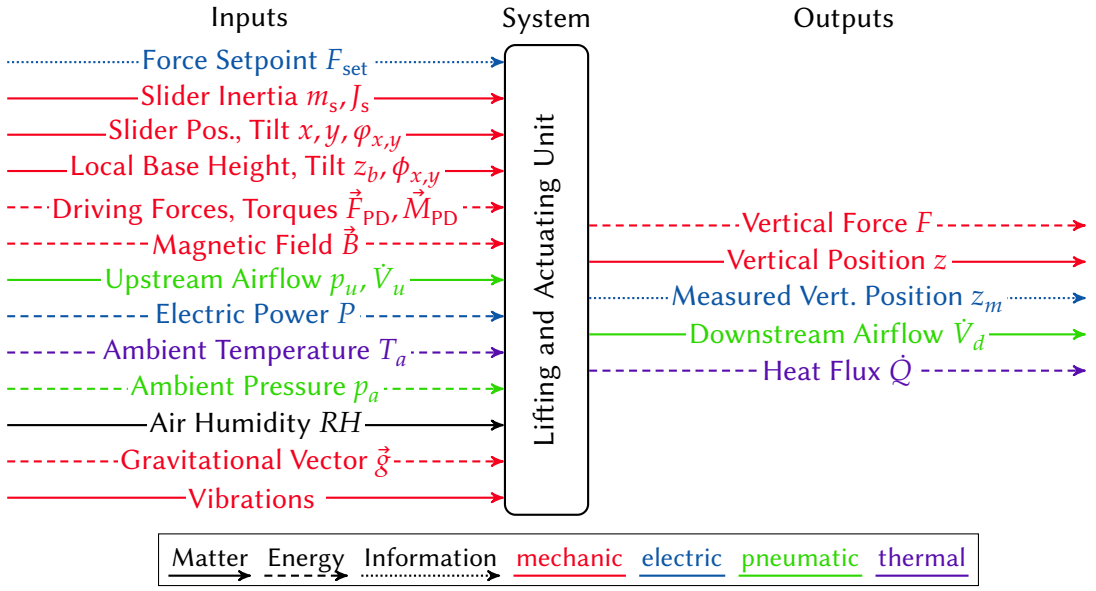

Figure 3.3: Overall function with input and output parameters of one LAU. The three line types represent matter (solid line), energy (dashed line) or information (dotted line) transport. The line color corresponds to the physical domain.

the slider moves along in x- and y-direction and tilts around φ_x and φ_y. The planar air bearing in the LAU interfaces the stators reference surface. Therefore, the local vertical position z_b acts on the lower end of the LAU. In the same way the local slope of the reference surface, denoted with ϕ_x and ϕ_y, are introduced. The planar drive (PD) creates a driving force $\vec{F}_{PD}$ and torque $\vec{M}_{PD}$, which will act on the LAU through the slider. Since the NPPS100 uses electromagnetic drives a magnetic field $\vec{B}_{PD}$ will be present which might result in forces on the LAU, therefore it is classified as a mechanical energy.
Because the machine is situated in a laboratory, different energy sources are available. Air pressurized to the upstream pressure p_u can be drawn from a wall supply unit. When the air flows, an air mass $\dot{V}_u$ is transported. Electrical energy is available via different wall sockets. The drawn electrical power is denoted as P.
The following input quantities derive from the surrounding laboratory conditions. They can be described with a couple of parameters, the most important one being the thermal influence of the ambient air temperature T_a. Further the surrounding air has a certain pressure p_a which may introduce forces onto the system. This ambient air is also capable of dissolving water vapor, with the corresponding parameter being the relative humidity, denoted as RH. The LAU

is supposed to lift a mass, therefore has to act against the local gravitational vector $\vec{g}$.
The last listed input are external mechanical vibrations. These disturbances are introduced via the machine bed into the planar drive and therefore the LAU. Aerodynamic forces may occur by moving the slider but are neglected since they are assumed to be extremely small for the sliders velocity regime.

The first outputs reflect the desired functionality: The actual vertical force F is the major output of each LAU. Through the external control system the vertical position z is adjusted. If an internal measurement system is present in a LAU, the measured vertical position z_m can be fed to the control system. The pressurized air, which is put into the system, has to exit at some point. This downstream flow is denoted as $\dot{V}_d$.
The remaining outputs are side effects of using electrical power: In every electrical system the used power is dissipated as thermal energy, primarily specified by the heat flux $\dot{Q}$. Further, flowing electric current in a conductor results in a magnetic field $\vec{B}_{\mathrm{LAU}}$ in the surroundings.

3.3 Requirements

Based on the overall function, the requirements (req.) were compiled and listed in tables 3.1 to 3.3. These claims derive mostly from the projected functionality, the constraints on precision drive systems, as well as the available resources for the design.

Thus, the requirements are separated into three groups: The first group relates to the *function* of the LAU. The second group are requirements which derive from the *environmental* conditions, whereas the third group concerns the *design* freedoms and limitations for the Lifting and Actuating Units. In each group the entries are sorted by importance.
Further, it is distinguished between these three different types:

Fixed (F) requirements have to be satisfied exactly as noted.
Minimum (M) demands have to be fulfilled at least as noted.
Desired (D) claims are favorable but do not necessarily have to be met.

3.3.1 Functional Requirements

The functional requirements are listed in table 3.1, with the most important ones being number 1 and 2. They contain that three LAUs together must be able to lift the sliders mass m_S and tilt its angular mass (moment of inertia) J_S. For each claim two values are given, representing the lower and the upper bound. For the mass that means that the lower 9 kg limit is the mass of the unmodified slider. The maximum projected mass is composed of two additional masses: The DUT mass is specified as 1 kg. The total mass of one LAU should not exceed 1 kg. With three LAUs it results in a worst case total mass of 13 kg. The same approach was used for the angular mass limit approximation: The lower 45 000 kg mm² was derived from the Computer Aided Design (CAD) data of the unmodified slider. The worst case mass of 13 kg results in a J_S of 100 000 kg mm² due to the LAUs mass being far away from the center of mass. For initializing the NPPS100 all measurement beams need to be reflected back into their interferometer. Therefore, the corner mirror needs to be adjusted which requires a measurement system that is available from the start. Thus, req. 3 demands an internal measurement device to which the controller can respond. Further, this measurement system is used as a fallback if the signal of the z-interferometer is lost. Due to these use cases only a relative position signal

Table 3.1: List of functional requirements for the LAU

№	Type	Requirement	Symbol	Value
1	F	Lift slider and sample mass	m_S	9–13 kg
2	F	Tilt sliders and samples moment of inertia	J_S	$(45\text{–}100)\cdot 10^3$ kg mm^2
3	F	Measurement resolution of vertical position	z_m	22 µm
4	M	RMS deviation from the sliders z-position	z_S	$\lessapprox 1$ nm
5	M	Compensate error in slider tilting angles	$\varphi_{x,y}$	$1''$
6	M	Vertical travel range	z_t	0–10 mm
7	M	Minimum vertical acceleration	a_z	250 mm/s^2
8	M	Minimum vertical velocity	v_z	1 mm/s
9	D	Improve tilt measurement resolution	$\varphi_{\mathrm{mres}_{x,y}}$	$< 1''$

is required. The required resolution is derived from the angular resistance of the LIFs and the arrangement of the LAUs, see appendix A.1.1.
The req. 4 and 5 relate to the achieved positioning precision. Vertically the slider should reach a precision in the range of its x- and y-precision, previously given in table 1.2. For the tilting motion the equivalent goal will not be reached. This is due to much more precise measurement of φ_z (via the double beam y-LIF) than φ_x and φ_y (via an autocollimator). Thus, the goal was set to compensate the tilting error due to the limited stator flatness.
The projected vertical travel is set to at least 10 mm. This results in a possible DUT aspect ratio of 10 : 1, which fits very well to the intended sample geometries like lenses. By lifting the slider, the distance of the magnet arrays to the drive coils increases, thereby decreasing the effectiveness of the planar drive. Simulations show that the force-to-current ratio is reduced by about 70 % when the slider is moved 10 mm upwards, making this a feasible range.
Req. 7 and 8 describe the wanted dynamics of the LAUs. The vertical available acceleration should be at least as big as in the planar direction ($250\,\mathrm{mm/s^2}$). For the vertical velocity $1\,\mathrm{mm/s}$ appears to be enough for the travel range. The last functional requirement is desired but not a necessity: As stated above the autocollimator does not achieve the angular resolution as the differential y-LIF for φ_z. Therefore, it would be beneficial to implement a very precise vertical measurement system at every corner of the slider from which the tilting angles can be calculated.

3.3.2 Environmental Requirements

All requirements concerning the LAUs technical and ambient surroundings are listed in table 3.2. Most importantly the system to be developed must be compatible with the existing systems. This means that the LAU must be mechanically compatible with the NPPS100 (req. 10) and electrically compatible with the control system (req. 11). These two requirements may also fit the design-related list but are listed here since they primarily derive from the technical environment.
Introduced heat has several negative effects. Therefore, the req. 12–to minimize the heat dissipation–has a very high priority [6]. First of all, introduced heat results in a temperature change in the surrounding air and the physical bodies. Especially changes in the shape and size of the reference body (corner mirror) result in errors in position orientation. Secondly, temperature gradients in different parts result in tension and deformation of the slider and corner mirror, as well as the stator and the metrology frame. The change in air temperature in the measurement space effects the refractive index of the air and results in free

Table 3.2: List of environmental requirements for the LAU

№	Type	Requirement	Symbol	Value
10	F	Compatible with the NPPS100		
11	F	Operable from the existing control system		
12	M	Minimize dissipated heat in operation	$\dot{Q}$	µW
13	F	Maximum available absolute upstream pressure	p_u	5 bar
14	M	Maximum air consumption	$\dot{V}_u$	3 SL/min
15	M	Maximum electric power consumption	P	500 W
16	M	Magnetic flux density the LAU is subjected to by the planar drive	B_{PD}	≈100 mT
17	M	Maximum allowed magnetic stray field	B_{LAU}	≈10 mT
18	M	Ambient temperature in operation	T_a	21.0 ± 0.2 °C
19	M	Ambient temperature for mounting and storage	T_a	20^{+20}_{-10} °C
20	M	Absolute atmospheric pressure	p_a	890–1 060 hPa
21	D	Vacuum compatible	p_a	≈200 mbar

convection, influencing the beam path of the LIFs [6–8, 46]. Thirdly, the whole measurement space can be seen as a thermal system. Due to the large mass and low heat conductivity of the stator this system has a high thermal time constant. Therefore, after exiting this system it takes a long time to reach its equilibrium again. Due to these different effects a specific maximum heat flux $\dot{Q}$ can not be given. From the NPPS100 and other existing systems it is known, that a constant heat flux in the µW-range should not induce relevant heat-related errors.
The constraints set by the supply system follow in req. 13, 14 and 15. The available pneumatic upstream pressure is about 4 bar (gauge pressure). The air consumption limit is set to 3 standard liters per minute (SL/min). Each of the currently used bearing pads has an air consumption of 1 SL/min [32]. So for the whole LAU the maximum for continuous operation is set to be three times this value. The air flow is limited since additional airflow may disturb the beam path of the LIFs, resulting in measurement errors. Further, an extremely high air consumption might lead to a reduction of the upstream pressure. The electric power consumption was also limited since high power usage results in many issues such as excessive heat, triggering fuses and additional wiring effort to provide more power. Additionally, thicker wires leading to the slider add con-

straining forces.
Req. 16 and 17 concern the magnetic compatibility between the LAU and planar drive. Since the coils and magnets of the planar drive are not encapsulated the magnetic flux is distributed in the space around these components. Simulations of the magnet arrays show that the expected absolute magnetic flux density B in the LAUs design space will not exceed 100 mT. If any magnetic components are used in the LAU, it should not influence the planar drive components. Because of the open design of the planar drive the restrictions on the tolerable flux density created by the LAU are tighter by one magnitude.
The following requirements describe different ambient conditions. The ambient temperature in operation (req. 18) is in the range of 21.0 °C$\pm$0.2 °C, which is very close to the standard laboratory conditions. This temperature stability is achieved by air-conditioning the laboratory room. In req. 19 the temperature range is a lot higher: 10 °C to 40 °C. This is the expected temperature range for the mounting process and includes possible temperature extrema from storage and transportation of the units. The surrounding pressure conditions are summarized in req. 20 and 21. The system usually operates at atmospheric pressure which changes with the altitude and weather. The laboratory where the system is set up is situated at circa 530 m above sea level. Therefore, the pressure ranges from 950 hPa to 1 013 hPa, calculated with the barometric formula [47, 48]. Additionally, the range is increased in both directions by weather-dependent pressure changes [49]. In future applications, this unit might be used under low class vacuum conditions [50]. Therefore, req. 21 suggests a lower ambient pressure range of 200 mbar [51].

3.3.3 Design Requirements

The requirements concerning the geometric design are tabulated in table 3.3. These are no scientific constraints as they derive from the available space and economical limitations. First the design space is limited by the slider and the surrounding stator-fixed components, denoted in req. 22, 23 and 24. The slider body has pockets on every corner, which are available as design space. These pockets have the volume of a slotted hole (or an extruded stadium shape), as shown in fig. 3.4. The major limiting dimensions are the height with 60 mm and the width with 50 mm.
In req. 1 the lifting mass was already addressed. There the derived maximum mass for one LAU was set to 1 kg. Since this is a very relevant design parameter it is specified in req. 25 specifically.
The NPPS100 is the only short term application for the LAU. Therefore, the

Table 3.3: List of design-related requirements for the LAU

№	Type	Requirement	Symbol	Value
22	F	Available design space in width direction	$w_{\max}$	50 mm
23	F	Available design space length-wise	$l_{\max}$	≤94 mm
24	F	Available vertical design space	$h_{\max}$	60 mm
25	F	Maximum mass per unit	m_{LAU}	1 kg
26	F	Production processes suitable for prototypes		
27	F	Suitable for manual assembly		
28	M	Lot size (number of units to produce)		3 pcs
29	M	Maximum cost per unit		10 000 €
30	D	Reusable design		
31	D	Completely enclose the unit		

lifting devices have a prototype character, so processes for series or mass production are not available (req. 26). The same applies for the assembly of the LAUs, see req. 27. Req. 28 lists that only three units are needed and the available financial resources (req. 29) for each are about 10 000 €.
The last design relevant requirements are desired demands. For future applications it would be beneficial if the developed device could be reused in the nanopositioning framework, which is reflected in req. 30. Further, for moving and extending devices it is always desirable to have a design, where no objects can enter into the device (req. 31). So no wires, tubes or other parts can get stuck between moving parts and no dust can accumulate inside the device. This is relevant for the future integration of the LAU in industrial (fabrication) systems. Additionally, enclosed systems appear to be more appealing to most observers.

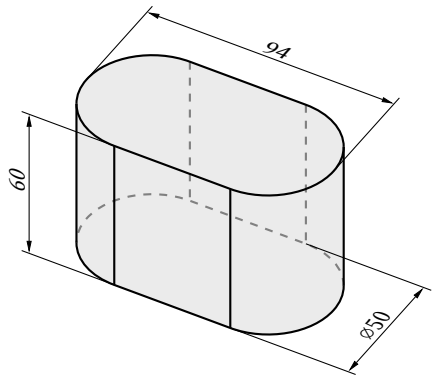

Figure 3.4: Available design space for one LAU with the dimensions given in millimeters

3.4 Functional Structure and Subunits

From the previous investigations the functional components and their organization were derived. In fig. 3.5 the arrangement of all functional units for the LAU is shown. Each unit is composed of the five functional elements inside the dash-dotted line. The bottom two components, planar guiding and tilt joint, are already known from the NPPS100 setup and form the basis of the LAU.
On top three components are added in parallel. The guiding allows relative vertical motion between the slider body and the basis but limits it in all other DOFs. The measurement system is used to initialize the NPPS100 via the control system. The third element is the drive system, which actuates the slider body relative to the LAUs base. To drive the actuator an amplifier is usually needed which is supplied with electric power and gets its set-value from the control system. Usually with actuators it is possible to not only put mechanical energy into the object (slider) but also draw energy from it (damping). The fig. 3.5 is valid for almost all kinds of electric actuators.
Since pressurized air is available, the actuator does not necessarily have to be driven by electricity. For using a pneumatic actuator the amplifier needs to be exchanged by a valve, which has to be supplied with air. Then the valve controls the airflow to and from the drive.

To further elaborate the internals of the LAU the available physical effects for the guiding and the drive will be investigated in the following sections 3.5 and 3.7. Since the demands on the internal measurement system are not as strict, the

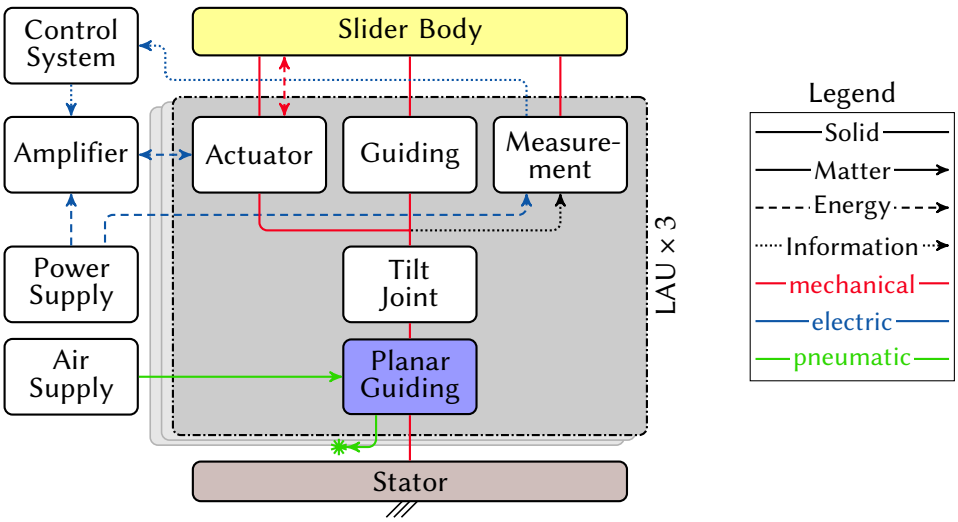

Figure 3.5: Structure with functional units and their interaction of one LAU

measurement method will be selected later in the design process. Additionally, many compact of-the-shelf products are available which can be integrated with little effort.

3.5 Comparison and Evaluation of the Physical Actuation Effects

The drive system needs to create a motion which is translational and one dimensional. Thereby, the sliders mass is a constant load (force) on the drive system during one operation cycle. This constant force may change with different sample masses. Some additional forces need to be created by the actuator to move the slider vertically and to dampen external disturbances. The detailed investigation of the load forces can be found in section 4.1.

This section compares available physical actuation effects in the scope of nanometer-scale precision positioning of the described load. Following the evaluation criteria are investigated, before listing and comparing the different available force creation methods.

3.5.1 Criteria for choosing an Actuation Effect

The criteria for the selection of the actuation type are described in the listing below. For their usage in the evaluation table 3.4 their abbreviations are introduced in parentheses.

Precision Evaluates, what precision and accuracy can be expected from the actuation effect.

Transmission Actuation principles may need an additional transmission to transform the actuator motion into the desired output motion.

Heat Estimates how much heat will be generated during operation.

Design Freedom Determines how much constrained or freely the actuator can be designed.

Integrability Describes how well the drive can be integrated with other components.

Dynamics Describes what range of velocities, accelerations, as well as jerks, can be achieved.

Energy Transformation Summarizes how complex the transformation of the input energy is, to drive the actuator.

Control Complexity Describes how much effort is necessary to control the actuator (linearity, hysteresis, etc.).

3.5.2 Physical Actuation Effects and their Evaluation

The following investigation is based on the large variety of actuation forms listed in [45] and [52].
Due to this large number, very exotic methods [53, p.68] are sorted out with a preselection. Most of these forms cannot be realized since they are very weak (dielectric, radiation). Others are not feasible because they require an extensive amount of heat (bimetal, Shape-Memory-Alloys). A liquid-based method (hydraulic, electro-, magnetorehologic, chemical) is not suitable since a whole new medium processing cycle would be necessary and any leakage could damage the equipment. Some effects cannot be designed in the scope of this work due to their complexity or the required materials or components are hard to obtain (magnetostriction, superconductivity). The remaining competitive types are pneumatic (PN), piezoelectric (PZ), LORENTZ-force (LF) and reluctance (RL) actuators, shown in fig. 3.6. They will be compared and evaluated in table 3.4 where the mentioned acronyms are used in the column headers.

For every criterion scoring points between -2 and $+2$ are awarded. If the actuation method excels in comparison to the other methods, it is evaluated with $+2$. If it is very unfavorable compared to the other methods it receives -2 points. Methods which lie between the two extremes are evaluated -1, 0 or $+1$ according to their degree of fulfillment. The points for the *Precision* criterion will be doubled, since it is of major importance for the application.

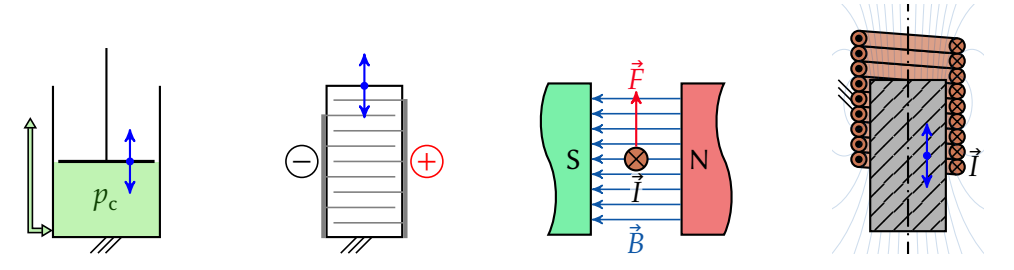

(**a**) Pneumatic (**b**) Piezo (**c**) LORENTZ (**d**) Reluctance

Figure 3.6: Possible actuation methods for the vertical drive

Table 3.4: Evaluation of the physical actuation effects with points ranging from −2 to +2. The abbreviations stand for the following effects: *PN*: pneumatic, *PZ*: piezoelectric, *LF*: Lorentz-force, *RL*: reluctance

Criteria	PN	PZ	LF	RL
Precision ×2	−2	+2	+2	+1
Transmission	+2	−2	+2	+2
Heat	+2	+1	−1	−2
Design Freedom	0	−2	+1	+2
Integrability	0	+2	−2	−2
Dynamics	−2	+2	+1	−1
Energy Transformation	+2	−2	0	0
Control Complexity	0	−2	+2	−2
Manufacturing Cost	+2	−2	0	+1
$\sum$	+4	−3	+5	−1

All points are added up for each method. From these values the overall suitability can be read.

Piezo stages achieved sub-nanometer precision [54], whereas pneumatic stages do not reach a comparable result.
Piezo drives by themselves have a very small travel range (small strain). It can be increased by stacking more piezoelectric layers onto of each other. The inchworm motor arrangement is not investigated since no continuous motion can be achieved. Further, these actuators usually need a preload. To tackle both of these problems they are usually combined with a compliant mechanism. This mechanism acts as a transmission to increase the output travel compared to the input displacement. All other listed actuation methods do not need a transmission. They can act directly on the output, therefore they are evaluated +2 points.
Pneumatic actuators can be designed in a way to avoid local thermal energy dissipation. Depending on the drive mode, piezoelectric drives create only minor amounts of heat [55]. Whereas both Lorentz-force and reluctance actuators rely on electrically powered coils, which dissipate heat due to their resistance. With reluctance actuators an additional effect acts as a heat source: The change of the magnetic flux in the yoke results in eddy currents, due to the conductivity of the material. In Lorentz-force actuators this is only a very minor effect due to the usually very little flux change in the ferromagnetic material.
Piezoelectric drives are available in different shapes (cuboids, cylinders, rings)

and sizes. But compared to the other actuation methods they are very limited in the design freedom due to material limitations and the required preload and amplification mechanism. Pneumatic actuators are limited in the design by their sealings, whereas Lorentz-force drives are constrained by the shape of the permanent magnets. Therefore, reluctance actuators are the most versatile design-wise.
For integrating the drive system with the other components their geometric size plays a central role. Piezo drives can be minimized very well and are therefore simple to implement into a design. A pneumatic actuator only needs a surface on which the airs pressure can act. The shape is irrelevant but an lateral surface is needed to which the working pressure is sealed from the ambient pressure. The electromagnetic actuators are harder to integrate, since they need a spatially extended coil, an air gap and geometrically corresponding pole surfaces.
For the application in the NPPS100 a pneumatic actuator needs very little adjustment of the input energy (pressurized air). One controllable valve is sufficient. Electromagnetic drives usually need very moderate voltages but a bidirectional controllable current, which increases the complexity of the amplifier. Whereas piezoelectric actuators need very high voltages, a lot larger than the voltage of regular laboratory power sources.
Both, reluctance and piezoelectric drives are known for their hysteresis and non-linear behavior, therefore increasing the complexity of the control system. Controlling of pneumatic pistons is not trivial but nowadays the technology is wide spread in industry applications and valves with integrated controllers are readily available. The friction of the piston sealing is subjected to the stick-slip effect, which increases the control complexity. But other non-conventional and non-contact sealing methods with reduced friction are possible [56, 57]. In contrast, common Lorentz-force actuators are characterized by an inductance and a parabolic position dependency of the force-to-current ratio [58]. From a control perspective these effects can be addressed rather easily.
The expenses for a pneumatic drive are very low, since the parts are simple to machine and sealings are available of the shelf. The prices for the reluctance actuator components are also not very high since coils and iron yokes are low cost materials. Strong permanent magnets for Lorentz-Force drives used to be very costly but are offered by more and more suppliers, reducing the prices a lot. Piezoelectric ceramics and the production process for multilayer actuators are the highest, compared to the other drive methods, resulting in the -2 rating.

The summed evaluation points reflect, that for the defined criteria set the Lorentz-force effect seems to achieve the best results. The pneumatic actuation scores second, due to its simplicity. Unfortunately the dynamics are very lim-

ited, reducing the expected overall performance. The piezo drive principle is a proven method in micro- and nanoactuation. But for customizing an actuator with a macroscopic travel it requires the highest design effort. Reluctance actuators are used a lot in automation due to the available design freedom. Apparently, this effect is not well suited for precision motion applications.

3.6 Introduction of a Weight Force Compensation in Parallel with the Precision Drive

In the previous section the Lorentz-force actuation method scored best. The biggest shortcoming of this effect is the heat emission, thus it needs to be investigated prior to the design process.
The average emitted heat can be estimated from the permanent load on one LAU. This permanent load is the weight force of the slider, which results in a force of about 43 N. Detailed calculations are presented in section 4.1. An exemplary linear Lorentz-force actuator is the Bei Kimco LA28-22-001A [58], which fits the requirements of force and stroke very well. With an actuator constant of $10.4\,{}^{\mathrm{N}}/\sqrt{\mathrm{W}}$ this drive would dissipate about 17.3 W permanently (see eq. (4.54)). Since its diameter of $\approx$ 70 mm and length of $\geq$ 50 mm already exceed the available design space, it is not possible to implement methods to mitigate the introduced heat. Therefore, a single Lorentz-force drive is not feasible.

3.6.1 Methods for realizing a Weight Force Compensation

An approach realized in other precision devices (see section 1.1.1) is to introduce two actuation methods in parallel: One drive system counters only the weight force of the lifted stage, subsequently referred to as the weight force compensation (WFC) system. This weight force compensation (WFC) has to have high load carrying capacities but does not need to achieve the dynamics, necessary for the precision motion. Therefore, the second, more dynamic drive system is utilized. Hence, it does not need to have the high force output and can be specialized for the dynamic loads.

A methodological similar but physically different concept is to use a coarse and fine stage, as described in [59]. Often a self-locking coarse stage (e.g. spindle drive) with a precision drive on top is used. The downside of this setup is that

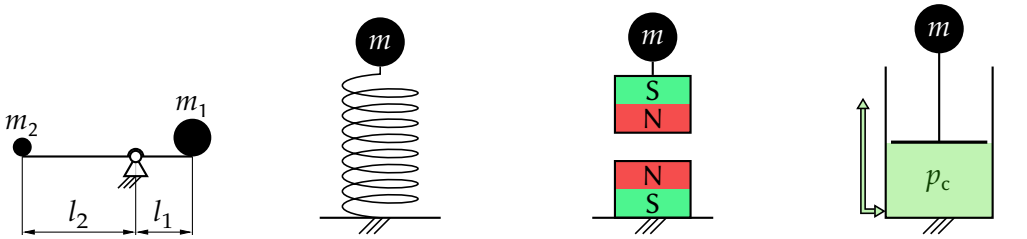

(**a**) Counter weight (**b**) Mechanic spring (**c**) Magnetic spring (**d**) Pneumatic

Figure 3.7: Possible methods for a weight force compensation system

the flow of drive forces needs to pass through many components. Therefore, this multi-mass system is prone to oscillations. Furthermore, in a vertical application both drives need to be powerful enough to carry the weight force.

For the WFC most of the constraints and criteria of the actuation investigation from section 3.5.2 apply. One difference is that only force creation methods are investigated which have no local thermal losses (passive). Further, as specified, the dynamics are not crucial but the position and force needs to be adjustable to accommodate sample objects with different heights and weights. Because of the reduced number of compared effects and criteria this evaluation is described here without a numeric rating. The corresponding evaluation table can be found in appendix A.1.3.

Figure 3.7 shows schematics of the following possible WFC effects. Using a counter weight is the simplest method (see fig. 3.7a). To adjust the force of the counter weight either the weight or the length of one lever needs to be adjustable.
Therefore, a lever mechanism and its local actuation is required. The biggest downside is, that additional large masses are required. This further increases the inertia of the whole system, thereby having a negative impact on the dynamics of the slider in all spacial directions.

Mechanical springs as in fig. 3.7b are a reliable method to reduce the load on certain systems. Using a regular linear spring the equilibrium is different for every weight. Leaving this equilibrium results in an increasing load on the precision drive. Therefore, the base point of the spring needs to be adjustable vertically to move the equilibrium through the whole stroke. This resembles partially the *coarse-fine-stage* concept but with parallel drives. To move the base point, another drive is needed, partially negating the power savings. With specialized shapes like cup springs or rolled steel strip springs a constant force can be achieved on a certain part of their stroke. The downside of these springs is

that the force level can not be adjusted, so to cover different mass ranges a lever mechanism is needed where the lever length can be adjusted [7, 18]. These adjusting mechanism needs additional space, further actuators, introduces more mass and parasitic motions. Overall the complexity of the design is increased significantly.

The same arguments apply for magnetic springs in section 3.6.1. They consist of a fixed magnet unit and a moving permanent magnetic part. In general, they have a very progressive behavior which means that the force imbalance changes dramatically while moving away from the equilibrium [60]. As with mechanical springs the base point would need actuation. Further, magnetic springs are available with a partially constant force along their travel [61]. Unfortunately, as with mechanical constant force springs their force can not be adjusted directly.

As described before, a pneumatic WFC is a fully capable actuator (see fig. 3.7d). By itself it can travel the whole stroke by loading or unloading an air chamber with pressurized air via a controlled valve. Therefore, motions with a reduced dynamic can be introduced with the pneumatic system, possibly taking load of the precision drive. If the DUTs mass changes the equilibrium pressure changes. So the chamber pressure has to be controlled to the new level. The valve has to be outside the measurement space, since its operation also introduces thermal energy. The air chamber acts like a spring but its stiffness can be adjusted by its design and pressure.

All in all the counter weight method in itself is very simple but introduces complexity when the force needs to be adjusted. The spring based variants (mechanical, magnetic) can only negate the weight force for one mass at a single point in the stroke, resulting in static non-zero loads in the rest of the stroke. An additional internal adjustment system is needed to make the whole travel weight force free. A pneumatic WFC has also a spring-like behavior but it is fully adjustable from the outside. The complexity and mass of the adjusting components is offloaded from the slider. The local components on the LAU can be kept very simple and they do not induce local thermal emissions.
Therefore, a pneumatic WFC will be used, since it has the most benefits of the evaluated WFC methods.

3.6.2 Topologies for the Pneumatic WFC

A variety of different design topologies and variants for a pneumatic WFC are shown in fig. 3.8. First, the location of the piston and the cylinder can be ex-

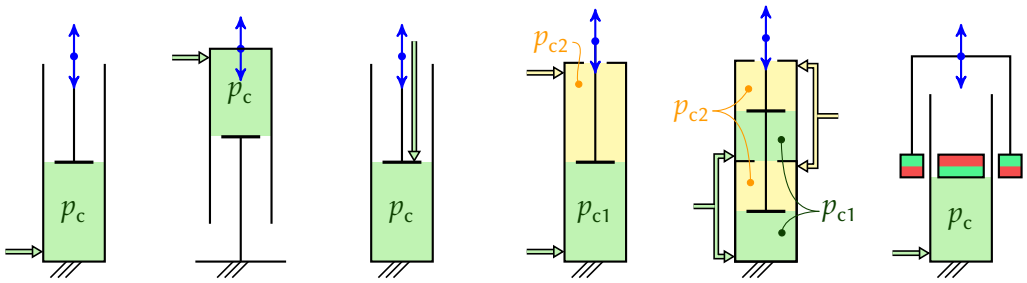

(**a**) Normal (**b**) Upside down (**c**) Piston inlet (**d**) Double acting (**e**) Double piston (**f**) Rodless

Figure 3.8: Possible principle topologies for including a pneumatic WFC

changed (figs. 3.8a and 3.8b). At this point of the design process it is unclear, which variant is best suited for this application.
Figure 3.8c shows an alternative method of feeding air into the chamber. Since the pressure tube connects from the stator to the slider, it is best to feed the air into the chamber via the slider-fixed assembly. In this way it is possible to avoid additional flexing and moving tubes.
The next variant describes a common piston setup in industrial applications: the double acting cylinder fig. 3.8d. Here two pressure chambers act on one common piston. This method allows significantly greater dynamics and stiffnesses, as both chambers brace against each other with a high pressure. Despite its desirable properties, this method will not be realized due to the doubled number of pneumatic hoses.
The topology from fig. 3.8e shows two pistons with one common rod, resulting in four chambers. This kind of setup is suitable, when a large piston area is needed but radial space is limited, whereas axial space is available. Due to the large number of sealings this method will not be implemented.
The last presented topology element is the rodless piston, see fig. 3.8f. With this method the stroke is maximized while the whole device keeps its axial dimensions. To not use a sealing along the cylinders wall, the piston can drive the outside parts via magnetic forces. This magnet will influence and complicate the electromagnetic drive system, further a method has to be found to keep the magnet from contacting the cylinder wall. Since the required travel is very small compared to the axial available space, the given disadvantages outweigh the spatial advantage.

3.6.3 Frictionless Sealing

To keep the pressurized air inside the air chamber it needs to be sealed against the cylinder wall. Contacting seals with elastomeric sealing rings are wide spread but are subjected to a parasitic friction force [57]. In comparison sealings with ferrofluids [62] have a much reduced friction. As an electromagnetic drive will be implemented into the device a proper sealing performance can not be ensured. Sealing the chamber with a membrane (diaphragm or bellow) introduces disturbing forces, which–depending on the membrane material–are expected to be nonlinear and time-variant through the creeping of the material. Contactless seals can overcome the above downsides. Unfortunately, they always result in a certain leakage of the fluid. For rotary systems many advanced designs exist [57, 63], whereas for translational systems only one major principle is available: the gap seal. There, a gap between the moving part and the resting part assures a contact-free motion. Through this gap parts of the pressurized chamber air will leak out. Therefore, this sealing gap needs to be minimized.

3.7 Discussion of the Vertical Guiding

In each LAU there are two assemblies which need to be able to move vertically to each other: a top assembly which connects to the slider and a base assembly which rests with the bearing pad on the stator. To allow this single translational DOF a well constrained linear guiding needs to be introduced. Since this guiding axis is vertical, no weight force is acting on the guiding parts. Only the dynamic forces of the base assembly of the LAU need to be transmitted.

3.7.1 Possible Guiding Methods

The possible mechanical guiding principles are displayed in fig. 3.9. Further insight can be found in [39].

The simplest method is shown in fig. 3.9a a sliding guiding. There a surface of the moving part directly interfaces with a surface of the resting part. Hence, this method can carry very large loads due to this large direct contact. But these contacts result in very high and non-linear friction forces despite the usage of lubrication like grease or oil. Additionally, the usually large guideway error is

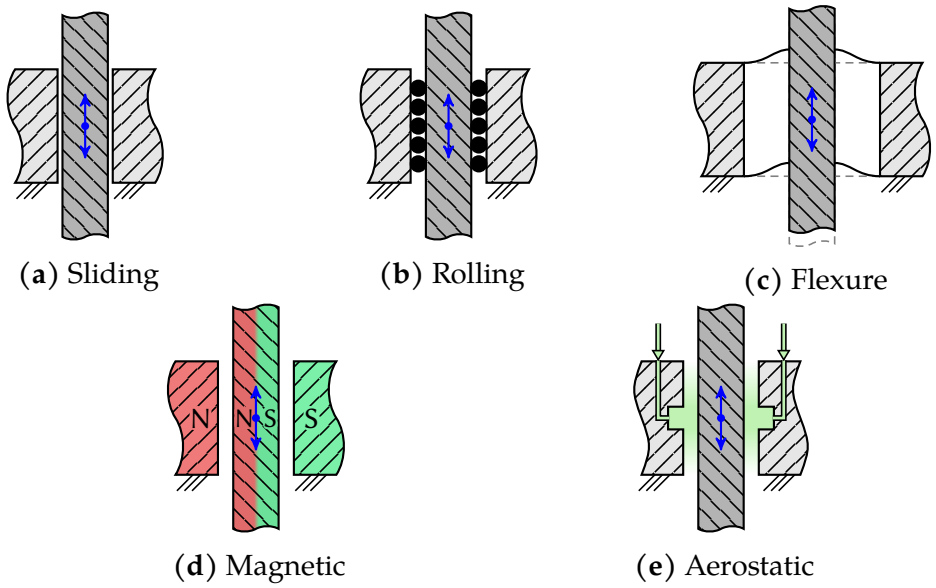

(**a**) Sliding (**b**) Rolling (**c**) Flexure

(**d**) Magnetic (**e**) Aerostatic

Figure 3.9: Possible methods for the linear guiding

problematic. Therefore, these guidings and bearings are not recommended and not used in precision devices.

The most common guiding type is displayed in fig. 3.9b: the roller guiding. Between the moving parts are elements, e.g. balls or cylinders, on which the guiding components roll. The friction is reduced a lot compared to the sliding guidings, but the rolling friction remains. Especially the effects between resting and rolling need to be addressed with advanced control methods [64].

A third linear guiding method is based on compliant mechanisms, exemplarily illustrated in fig. 3.9c. The moving shaft is constrained by flexible bodies. E.g. leaf springs or flexure hinges are connected with rigid beams which yield a mechanism with the desired DOFs. These setups are free of friction and hysteresis but introduces a spring-like behavior. Further, these mechanisms have a comparably low stiffness in the constrained directions. Usually they allow only very limited motions. [65, 66]
To increase the travel range large levers need to be introduced, resulting in high spatial demands. Additionally, due to the very small thickness of the joint bodies, measures need to be taken to prevent the mechanisms from overloads. Because of these numerous downsides, this method is not realized.

Figure 3.9d shows a next guiding method which uses the repelling forces of permanent magnets. The guiding elements move without contact, so no friction force is introduced. These guidings are not available of the shelf and need to be

designed for the specific application. Further, they have a low stiffness compared to e.g. roller guidings. Due to the magnetic field distribution of permanent magnets additional parasitic axial forces are introduced. These forces, as well as the constraining forces, behave very nonlinear. [67]
When introducing coils to manipulate the magnetic flux these guidings and bearings can achieve a very high stiffness and damping coefficient. But these coils will introduce further thermal emissions into the system. Because of the low stiffness and non-linearities of the passive guidings and the heat dissipation of the active guidings this method is not implemented. [68]

Fluid guidings have the most similarities with sliding guidings. A small gap between the parts is introduced, which is completely filled with a pressurized fluid. Therefore, the guiding components should never come into direct contact with each other, resulting in virtually frictionless motion without any wear. The fluid can be a liquid (water, oil) or a gas (usually air). The variant using a liquid will not be investigated because the translationally loaded sealing will leak minor amounts of the fluid which endangers the equipment.
Using air as a fluid, two variants are possible to pressurize it: static or dynamic. Dynamic pressurization will not be investigated, since it requires constant and high relative speeds between the parts, which is not the case in the application. For aerostatic guidings, as seen in fig. 3.9e, the fluid is pressurized externally and then fed into the gap. Due to the small size of the air gap and the high pressure of the air the guidings are very stiff and have a good damping behavior. Thereby it does not matter whether the air is supplied via the resting or the moving part. Some catalog products are directly available from different manufacturers. The major downside of aerostatic guidings is the required permanent feeding with processed and pressurized air. Otherwise, the aerostatic guiding method is superior and therefore was chosen for this application. [69]

3.7.2 Aerostatic Linear Guiding Topologies

Aerostatic guiding elements have usually multiple degrees of freedom. Bushing elements have one rotatory and one translational, whereas bearing pads have two translational and one rotational DOFs. Some of-the-shelf integrated prismatic guidings exist [70] but only in dimensions which exceed the available space. So to create a well constrained one dimensional guiding multiple of the above elements need to be combined. Three general possible arrangements are presented in fig. 3.10.

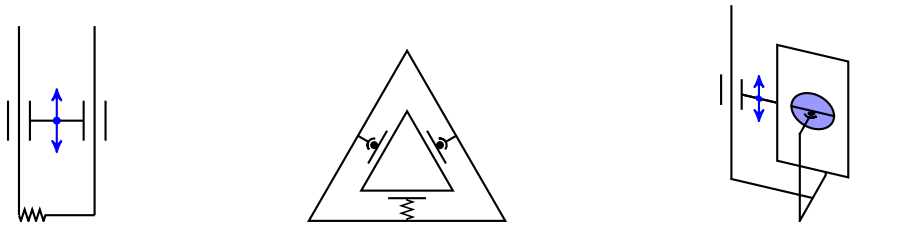

(**a**) Two parallel bushings

(**b**) Three or more bearing pads (top-down view)

(**c**) Off-center bearing pads (exemplary)

Figure 3.10: Possible aerostatic linear guiding topologies

In fig. 3.10a two bushings are used in parallel. The advantage of this setup is, that two identical elements are used and the load capacity is increased because the increased effective area. Either both bushing axis need to be adjusted very well in parallel or a soft coupling is required to not overconstrain the mechanism.
Further, multiple planar bearing pads can be used to guide a prismatic body, as seen in fig. 3.10b. This topdown view does not show, that additional pads are needed in another layer, to lock all tilting freedom. The miniaturization of this method is limited by the minimum pad size.
Another method is to mix the two above variants, exemplary shown fig. 3.10c. One bushing serves as the vertical guiding and off-center planar bearing pads are used to lock the rotation. By using two bearing pads opposed to each other no additional loads will act on the bushing. Coupling these pads with a cardan joint only a coarse adjustment of one pad is needed, since they adjust themselves to the counter surface. The planar coupling surface needs to be adjusted to the bushing axis, otherwise a vertical motion will be accompanied by a rotation.

The third configuration is favored because it allows a more compact setup. Since no rotational load is to be expected, the rotational locking system can be kept very simple and it can be positioned freely in the design space.

3.8 Resulting Technical Principle

In section 3.4 all essential functional components have been derived. Throughout the subsequent sections the drive and guiding components were investigated. The drive functionality was split into two components: The static load of the weight force is counteracted by a pneumatic WFC, whereas the dynamic precision motion is performed by a Lorentz-force drive. For the single-axis guiding the aerostatic method was chosen. The measurement system will be

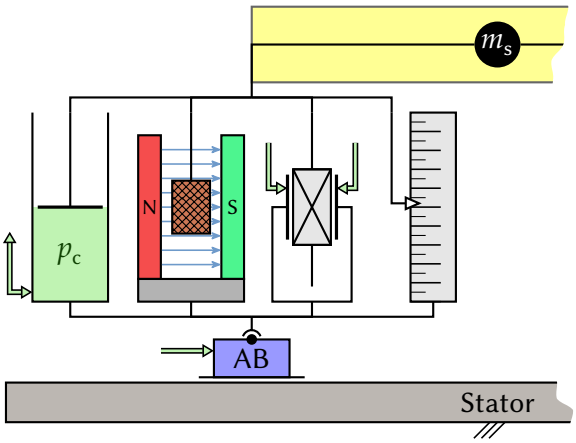

Figure 3.11: Technical working principle of the LAU, from left to right are the components: pneumatic WFC, precision Lorentz-force drive, aerostatic guiding, measurement system

investigated later in the process.
The derived technical principle for the LAU with all the named components is shown in fig. 3.11. All components have a slider-fixed part and a part that belongs to the LAU-base assembly which rests on the stator. The pneumatic WFC on the left is supplied via an external controlled pressure. It can be fed into the chamber via the chamber wall or the piston. The WFC symbolizes only vertical forces and can not transmit radial ones. The brown crossed box between the magnetic north and south poles resembles the cross section of a coil. It moves in the magnetic flux created by permanent magnets. To the right the non-rotating aerostatic linear guiding is shown. Also here it is technically possible to feed the air in either from the inside part or the outside part. On the right a scale and a measuring element are displayed. All these setups can also be turned over, by exchanging moving and resting part. Their arrangement will be decided in the following dimensioning process.

3.9 Discussion of the Shapes of the Components

The majority of industrial linear pneumatic drives feature a circular bushing (cylinder) and piston. The simple geometry enables the fabrication of parts with better accuracy, reduces the cost and improves the sealing performance while reducing the friction.
For linear Lorentz-force drives there are two popular types. The first type is

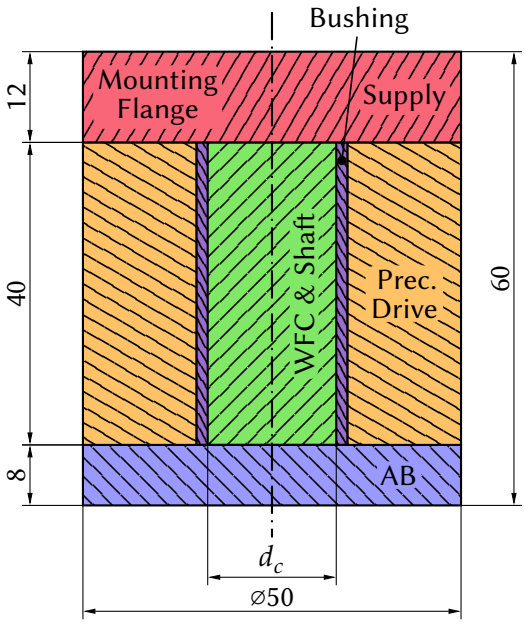

Figure 3.12: Cross section of the design space distribution of the rotational symmetric functional components; scaled 1 : 1

similar to the planar drive of the NPPS100. Plates with elongated flat drive coils run inside a long U-shaped yoke in which permanent magnets are mounted [71]. These drives are used for very long travel ranges, since multiple of these yokes can be strung together. The second type, the so called voice-coil drives, are more suitable for the application in the LAU. There a cylindrical coil moves inside a rotational symmetric yoke [58]. This type has very simple geometries and can be miniaturized very well. Further, all components can be obtained and manufactured very easily.
For the vertical guiding an aerostatic bushing with an external rotational locking system will be implemented.

All the named components will evince a rotational symmetric design. Since the angular orientation around the vertical axis between these functional components is irrelevant, very simple joining techniques can be applied, thereby reducing spatial demands. Further, the components can be integrated into each other, so the whole design space can be used effectively. Also rotational symmetric parts are known for their high stiffness and strength to weight ratio as they can withstand high loads. Therefore, the design goals can be achieved with reduced space and mass needs. This is a very big advantage for this application, since the available space is relatively small for the number of required functional components.

The draft design space distribution can be seen in fig. 3.12. The AB needs to be the bottom component. Here a very thin variant with just 8 mm height is implemented. By placing the WFC in the center, the leakage of the chamber is minimized, since only one sealing between the piston and the cylinder is required. Since the piston already runs in a cylinder its wall can be reused as an interface for the bushing. This means that cylinder, sealing wall and bushing will be integrated into a single part with one uniform diameter. Therefore, the sealing performance will benefit from the tight tolerances which are dictated by the aerostatic bushing. An additional channel with atmospheric pressure will be necessary between the sealing and the bushing so the chamber pressure will not influence the guiding pressure and vice versa.
Around this setup the voice coil drive can be integrated since the central design space is not relevant for its proper operation. Thus, the design is simplified and the number of components and their spacial demands reduced. All slider-fixed components are connected to a top mounting flange, which is also the hub for the air and power supply.

Chapter 4

Model Based Development of a Lifting and Actuating Unit

This chapter investigates the development, setup and application of mathematical models for the functional components of the LAU. These models are used to simulate the behavior of the modeled component. By varying different design parameters in the model the best performing configuration can be found. The parameter sets are verified to conform with all design constraints and requirements.

The basis for the following model compositions is the investigation of the load situation on one LAU. It is presented in the upcoming section. The subsequent sections describe the models of the WFC, the precision drive and the aerostatic guiding.

4.1 Load Situation

This section derives the different loads which can occur for one LAU. These estimations will usually assume the worst case situation.

The basis for all dynamic force calculations is the Newton's second law [48]

$$\vec{F} = m\,\vec{a} \tag{4.1}$$

which states that the force $\vec{F}$ is coupled to the acceleration $\vec{a}$ via the mass m.

In section 2.3 it was derived that each LAU has only one active DOF. Therefore, only the z-components of the vectorial values will be considered. As seen in

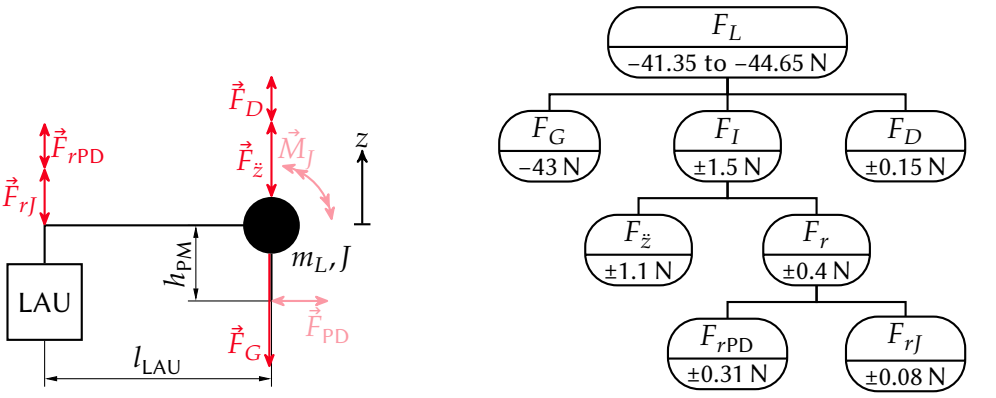

(**a**) Load forces on one LAU (**b**) Composition and values of the load

Figure 4.1: Load forces and their composition for one LAU

fig. 4.1 the total load force F_L is composed of three major components:

$$F_L = F_G + F_I + F_D \tag{4.2}$$

The gravitational force F_G is permanently present. It changes only when different samples are placed on the slider. The force component F_I reflects the inertia of the slider which needs to be overcome to accelerate and move it to a new requested position or along a set path. It can change very rapidly. The component F_D reflects the required force to counteract disturbances which have to be overcome to keep the slider on its desired path or position. This component can usually not be predicted in advance, so the drive system has to act instantaneously. Thereafter, the components will be investigated individually.

The most prominent component is the gravitational or weight force F_G. The gravitational acceleration is given in [48] approximately as:

$$g = 9.81\,\mathrm{m/s^2} \tag{4.3}$$

The sliders mass is given in table 3.1, req. 1. Assuming that the sliders center of mass is in the middle of all three LAUs, its gravitational force is distributed equally. Thus, the load mass on each LAU m_L is one third of the total slider mass. This gives for the gravitational force:

$$F_G = m_L\, g = \frac{m_S}{3} g \approx 43\,\mathrm{N}$$

The component F_I itself is composed of a translational part $F_{\ddot{z}}$ and a rotational part F_r. The desired translational acceleration was set in req. 7. Again each LAU needs to accelerate only one third of the sliders mass resulting in the translational component:

$$F_{\ddot{z}} = m_L a_z = \frac{m_S}{3} a_z \approx 1.1\,\mathrm{N}$$

The rotational part F_r is induced by two different torques. In a simplified way, a general torque equals a force F times its perpendicular distance l to the axis of rotation [48]:

$$M = F\,l \tag{4.4}$$

This rotational axis usually passes through the center of mass. The first torque is introduced by accelerating the slider with the planar drive. Using the values from table 3.1 in eq. (4.1) gives the acceleration force F_{PD} of 3.25 N. This force vector acts on the permanent magnets (PMs) at about $h_{\mathrm{PM}} = 25.5\,\mathrm{mm}$ below the sliders center of mass. The resulting torque of 83 mN m creates a load on the LAUs as the force $F_{r\mathrm{PD}}$. Moving the slider along the x-direction is the worst possible load case. There only two LAUs can counter the torque since the third LAUs lever length is zero in the xz-plane. With a lever length l_{LAU} of about 134 mm (see fig. A.1) the resulting force $F_{r\mathrm{PD}}$ for one unit is 0.31 N. The second part of F_r results from the torque needed to tilt the rotational inertia J_S, which was specified in req. 2 in table 3.1. The torque to accelerate a rotational inertia J is given by the Newton's second axiom for rotational motions [48]:

$$M = J\,\alpha \tag{4.5}$$

In the list of requirements no rotational acceleration α was specified. Therefore, a reasonable estimation is made: Presuming the slider experiences the maximum tilt of 1″. Requesting it to return and fully stop at zero deflection in 10 ms exceeds the expected tilt-error dynamics. Given these boundary conditions the angular acceleration results in (derivation given in appendix A.1.2):

$$\alpha = 11.1\,^{\circ}/\mathrm{s}^2$$

Here the worst case lever length is the same as above resulting in only a small required force:

$$F_{rJ} = 0.08\,\mathrm{N}$$

The required disturbance force F_D can be approximated from previous measurements and their empirical values on the planar drive. Approximating the

disturbing forces to be 10 % of F_I is a very conservative estimation, since the measures taken to prevent disturbances on the slider are numerous and effective (outlined in section 1.1.3).

The gravitational force F_G points always in the negative z-direction. Whereas F_I and F_D can change between $\pm 1.5\,\mathrm{N}$ and $\pm 0.15\,\mathrm{N}$ respectively. Due to Newton's third axiom [48] each LAU has to be capable of creating the respective counter forces.

4.2 Weight Force Compensation System

In this section the components of a pneumatic WFC are described with mathematical models. They are based on the works from [48, 72–75] and [76]. The goal is to identify the most important design parameters and to find feasible values for them.

4.2.1 Model Components

The WFC is composed of multiple components, as shown in fig. 4.2. On the left is the upstream pressure supply with its pressure p_u. It is assumed infinitely large so the pressure p_u will be constant. This reservoir is connected via a pneumatic line to a valve. This is a two-way valve. It controls the air flow into and out of the pneumatic cylinder. Therefore, it can direct the air flow either from the supply to the chamber or from the chamber to an ambient outlet. The valve feeds air

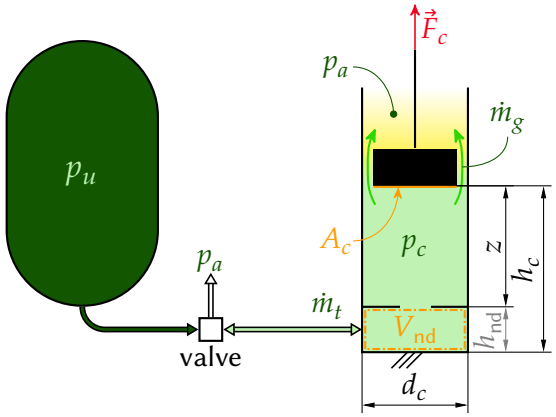

Figure 4.2: Schematic of the pneumatic WFC-model

into the chamber via a long pneumatic tube, the mass flow $\dot{m}_t$. The resulting pressure inside the cylinder p_c acts on the surface of the piston A_c, generating the force F_c. The height of the chamber is described with h_c. The volume of the piston which is non-displaceable (nd) is called V_{nd}. The air flow $\dot{m}_g$ leaks through the gap past the piston into the surroundings due to the imperfect sealing.

4.2.2 Force of a Pneumatic Piston

The central force equation for a pneumatic actuator is

$$p = \frac{F}{A} \tag{4.6}$$

where p is the absolute air pressure, A the surface and F the overall resulting force, that acts on this surface [48]. For pneumatic actuators this relevant surface is the pistons area A_c on which the inside chamber pressure p_c and the outside ambient pressure p_a act. The resulting force of the piston equals:

$$F_c(p_c) = A_c(p_c - p_a)$$

The area of a circular surface is defined as

$$A = \frac{\pi}{4} d^2 \tag{4.7}$$

with respect to its diameter d [77]. Since the piston and cylinder are circular its force is calculated as:

$$F_c = \frac{\pi}{4} {d_c}^2 (p_c - p_a) \tag{4.8}$$

Figure 4.3a displays the relation between p_c and d_c while setting F_c to the weight force F_G. The highest available pressure is the upstream pressure, given in table 3.2, req. 13. By filling the cylinder with this pressure a piston with a diameter d_c of 11.7 mm would be enough to reach equilibrium with the weight force F_G. This is not feasible since no margin for unforeseen future processing loads is left. To take load off the precision drive further force reserves are necessary. Choosing a larger diameter with a lower equilibrium pressure enables the drive to use the pressure reserves to carry larger loads or accelerate in the $+z$-direction. These acceleration reserves can be derived from the force equilibrium of the

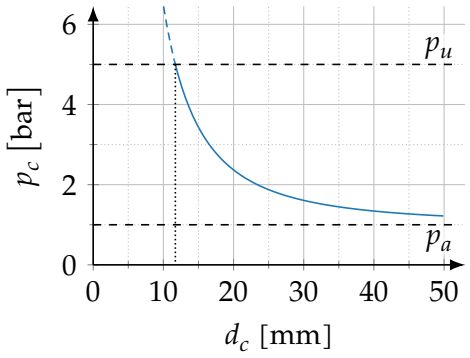

(**a**) Pressure which is necessary to counter the weight force for a given chamber diameter.

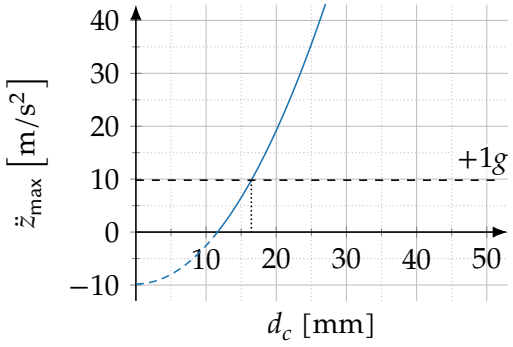

(**b**) Acceleration reserves for different chamber diameters, while pressurizing the chamber with p_u

Figure 4.3: Equilibrium chamber pressure and available maximum acceleration for different piston diameters

pneumatic piston:

$$\begin{aligned} 0 &= \quad F_c \quad - F_G - F_{\ddot{z}} \\ 0 &= A_c(p_c - p_a) - m_L g - m_L \ddot{z} \end{aligned} \tag{4.9}$$

Applying p_u to the chamber gives a maximum acceleration $\ddot{z}_{\max}$:

$$\ddot{z}_{\max} = \frac{A_c}{m_L}(p_u - p_a) - g \tag{4.10}$$

The theoretical acceleration reserves are shown in fig. 4.3b. Since the minimum chamber pressure is p_a the theoretical maximum negative acceleration equals $-1g$. To achieve a symmetric drive with a maximum positive acceleration of $+1g$ a chamber with a diameter d_c of 16.5 mm is needed.

Investigations on possible further diameter constraints follow in the next sections.

4.2.3 Stiffness and Eigenfrequency of an Ideal Pneumatic Cylinder

Since air is a compressible medium the air chamber will have a spring-like behavior. To find out, what dynamic components the pneumatic actuator can achieve its bandwidth needs to be estimated. Its bandwidth is limited by the first natural frequency, which is derived in this section.

For this approach it is assumed the cylinder is a closed volume V_c, where no additional air enters or leaves. Therefore, the inside air mass m_c is constant. Under the expected operating conditions (table 3.2) it is safe to assume that air behaves like an ideal gas. With its absolute pressure p_c and its temperature T_c its equation of state, the ideal gas law, is set up as follows [72]:

$$\begin{aligned} p_c V_c &= R_S T_c m_c \\ p_c &= R_S T_c \rho_c \end{aligned} \tag{4.11}$$

where R_S is the specific gas constant for an ideal gas. The airs density ρ_c is calculated via its mass and volume:

$$\rho = \frac{m}{V} \tag{4.12}$$

If the piston moves the volume changes and with it the gas temperature and pressure, which is called a polytropic process. This is a general process which can reflect the behavior of the other thermodynamic processes by adjusting its exponent n [72]:

$$pV^n = \text{const.} \tag{4.13}$$

The initial state of the gas is indexed with a 0, whereas the current new state (after compression or expansion of the cylinder) is not indexed. This means for the polytropic process:

$$p_0 {V_0}^n = pV^n \quad \text{or} \quad \frac{p}{p_0} = \left(\frac{V_0}{V}\right)^n \tag{4.14}$$

The general cylinder volume is given as

$$V = Ah \tag{4.15}$$

with its cross-sectional area A and its height h [77]. That means that in eq. (4.14) A can be crossed out and rewritten with p_c as a function of h_c:

$$p_c(h_c) = p_{c0}\left(\frac{h_{c0}}{h_c}\right)^n \tag{4.16}$$

From it the force function with the pressure definition from eq. (4.6) is set up (ambient pressure neglected):

$$F_c(h_c) = F_{c0}\left(\frac{h_{c0}}{h_c}\right)^n \tag{4.17}$$

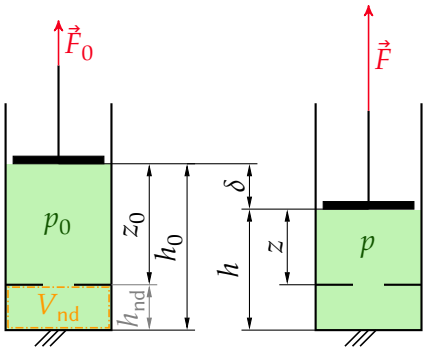

Figure 4.4: Compression of an ideal air volume

By compressing the cylinder from h_{c0} to h_c the piston is displaced by the distance δ, as shown in fig. 4.4, while the force on the piston increases. So h_c can be exchanged by $h_{c0} - \delta$:

$$F_c(\delta) = F_{c0}\left(\frac{h_{c0}}{h_{c0} - \delta}\right)^n \tag{4.18}$$

The stiffness is defined as the displacement derivative of the force:

$$c = \frac{\mathrm{d}F}{\mathrm{d}\delta} \tag{4.19}$$

Hence, the stiffness of the pneumatic cylinder can be derived

$$c_c(\delta) = F_{c0} n \frac{{h_{c0}}^n}{(h_{c0} - \delta)^{n+1}} \tag{4.20}$$

resulting in a hyperbolic relation between c_c and δ. With $\delta = 0$ the stiffness at the initial height h_{c0} is given:

$$c_c(h_{c0}) = F_{c0} n \frac{1}{h_{c0}} \tag{4.21}$$

or alternatively with respect to the vertical position z_0 of the LAU:

$$c_c(z_0) = F_{c0} n \frac{1}{(z_0 + h_{nd})} \tag{4.22}$$

For a harmonic oscillating mass with z as its single DOF the following differential equation is given [48] (neglecting damping):

$$F = m\ddot{z} + cz \tag{4.23}$$

with its angular frequency ω_0 and its natural frequency f_0:

$$\omega_0{}^2 = \frac{c}{m} \qquad f_0 = \frac{1}{2\pi}\sqrt{\frac{c}{m}} \tag{4.24}$$

From eq. (4.22) and eq. (4.24) the natural frequency of this pneumatic piston at its initial equilibrium state ($z_0, F_{c0} = F_G = mg$) is derived.

$$f_{c0}(z_0) = \frac{1}{2\pi}\sqrt{\frac{gn}{z_0 + h_{\mathrm{nd}}}} \tag{4.25}$$

In fig. 4.5 the eqs. (4.22) and (4.25) are plotted for different parameter sets. Three lines show pneumatic cylinder variants with different non-displaceable heights h_{nd}. With $h_{\mathrm{nd}} = 0$ the pneumatic cylinder has no additional volume. The largest stiffness and eigenfrequencies can be achieved along the whole travel. Increasing h_{nd} and therefore V_{nd} reduces both parameters dramatically. The dashed line shows the cylinder with $h_{\mathrm{nd}} = 0$ but with an F_G reduced by the DUTs mass. This displays the parameter change for the NPPS100 without a sample. Here the stiffness is only marginally decreased, while f_0 does not change at all since the mass crosses out in eq. (4.25).
The above described variants assume that the compression and expansion is an adiabatic process. During this process all thermal energy remains in the gas volume, further n is set to 1.4. The dotted line reflects the behavior for $n = 1$, thereby assuming an isothermal process where the gases temperature

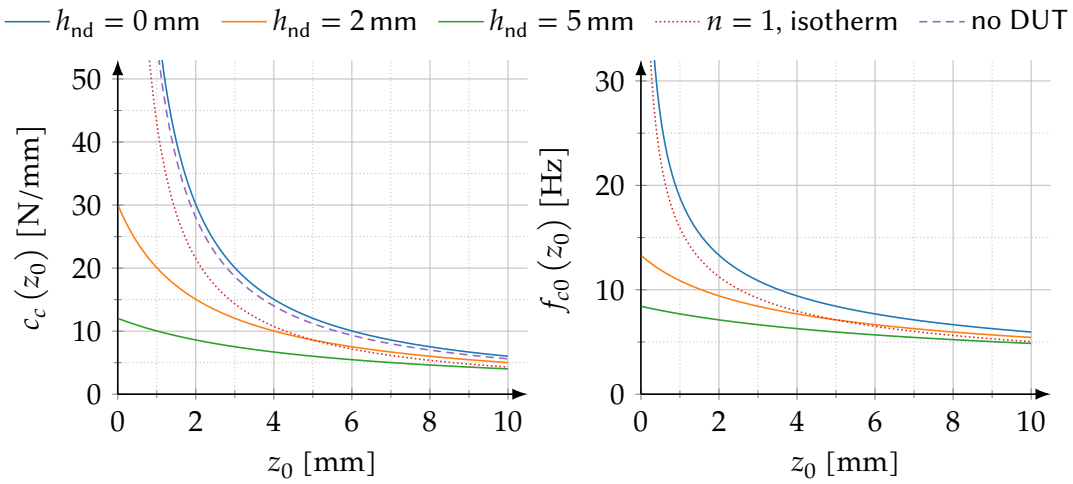

Figure 4.5: Stiffness and natural frequencies for a pneumatic chamber at different positions in its travel

does not change. Here the stiffness and natural frequency are slightly reduced. Both of these processes are ideal processes, empirical observations suggest the polytropic index to be in the range of 1.2. [72]

In general only lower dynamic components can be actuated with this single chamber pneumatic piston. A non-displaceable volume V_{nd} with its representative height h_{nd} lowers the accessible frequency region significantly. Therefore, this volume should be minimized in the design. But for all presented variations the lower limit is about 5 Hz. This is still enough to counteract the vibrations that can not be damped by the machine bed (seismic, building).

4.2.4 Piston Sealing

Motivated by the results of section 3.6.3 a throttling leakage sealing will be realized. Its geometry variables are shown in fig. 4.6. The gap between the piston and the cylinder wall has a ring-shaped cross section, where the inner diameter is the piston diameter d_c. It has a length of l_g and a width of w_g. The basic equation for its volume flow $\dot{V}_g$ is found in [57, 78]. An extended equation for the mass flow $\dot{m}_g$ from [63] is adapted for this use case.

$$\begin{aligned} \dot{m}_g(p_c) &= \underbrace{\frac{1}{24}\frac{1}{R_S T_a \eta}}_{\text{gas properties}} \underbrace{\frac{\pi d_c {w_g}^3}{l_g}}_{\text{gap}} \underbrace{\left(1+\frac{3}{2}\varepsilon^2\right)}_{\text{eccentricity}} \underbrace{\left({p_c}^2-{p_a}^2\right)}_{\text{pressures}} \\ \dot{m}_g(p_c) &= k_g\left({p_c}^2-{p_a}^2\right) \end{aligned} \tag{4.26}$$

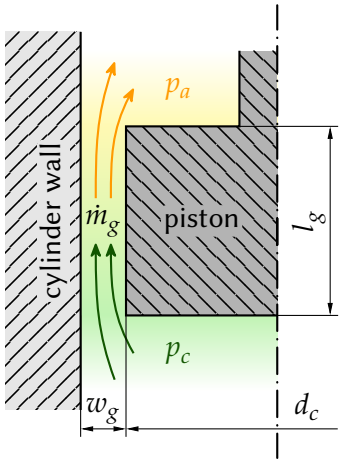

Figure 4.6: Geometry of a leakage sealing

The parameters are ordered by type. The first term includes gas properties of the ambient air. Here η is the dynamic viscosity of air. In [79] it is given as $18.3{\cdot}10^{-6}$ Pa s for laboratory conditions. The next term includes the squared chamber and squared ambient pressure, whereas the third term includes all geometric properties of the gap. The gap width w_g has a very strong influence on the leakage flow since it occurs with the third power. Hence, the gap should be kept small to minimize the leakage flow. The last term describes the eccentricity of the piston inside the cylinder. The relative eccentricity ε is defined as

$$\varepsilon = \frac{s_e}{w_g} \tag{4.27}$$

where s_e is the distance between the cylinders and the pistons axis, so it corresponds to the guideway error. Since an aerostatic guiding will be used this value is expected to be in the range of a single micron and can therefore be neglected. Additionally, due to the quadratic correlation a rather large eccentricity of 25 % results in an increase of the leakage flow of just below 10 %.

4.2.5 Pneumatic Transmission Line

The pneumatic tube connects the valve with the pressure chamber. When the valve opens, the pressure gradient between upstream and chamber pressure will induce a flow of air into the chamber. The transient mass flow of air in a pneumatic line is derived in [74] as:

$$\dot{m}_l(t) = \begin{cases} \exp\left(-\frac{R_t R_S T_u}{2 p_u} \frac{l_t}{v_s}\right) \dot{m}_v\left(t - \frac{l_t}{v_s}\right) & \text{if } t > \frac{l_t}{v_s} \\ 0 & \text{otherwise} \end{cases} \tag{4.28}$$

The exponential part resembles a damping due to the friction of air on the tube wall. Here the length of the pneumatic line l_t is introduced. Further, it depends on the pneumatic resistance R_t and the sonic velocity in air v_s. With R_t the complexity increases a lot since it depends on friction effects in the tube, which have a discontinuity when changing between laminar and turbulent flow [72, 74]. For the expected line length, this damping component has only a minor influence on the dynamics. In the delay part $\dot{m}_v(t)$ is the input flow function of the valve. The sonic velocity v_s describes how fast a pressure change travels through the air. So l_t/v_s is the time constant, which describes how long it takes a pressure change to travel from the input of the line to reach the outlet.

4.2.6 Valve Model

In [80] the general international standard model for round valves and outlets is given:

$$\dot{m}_v = p_h k_v \, \psi(p_h, p_l) \tag{4.29}$$

The parameter k_v and function ψ are defined as:

$$k_v = C\rho_{\text{ref}}\sqrt{\frac{T_{\text{ref}}}{T_h}} \tag{4.30}$$

$$\psi(p_h, p_l) = \begin{cases} \sqrt{1 - \left(\frac{\frac{p_l}{p_h} - b}{1-b}\right)^2} & \text{if } \frac{p_l}{p_h} > b \quad \text{(subsonic flow)} \\ 1 & \text{otherwise} \quad \text{(choked flow)} \end{cases} \tag{4.31}$$

Thereby, p_h and p_l are the high upstream and the low downstream pressure, whereas T_h is the air temperature of the upstream reservoir. The parameters indexed with $\square_{\text{ref}}$ are fixed values for air at reference conditions [72]. C is the sonic conductance and b the critical pressure ratio; both are characteristic values of the outlets geometry. The critical pressure ratio of air has a theoretical maximum of about 0.528 [72]. For pressurizing the chamber a valve with three ports is needed: the upstream inlet, the outlet to the chamber and the ambient outlet. Assuming that $p_u \geq p_c \geq p_a$ there are two variants of eq. (4.29) depending on the valve setting [73]:

$$\dot{m}_v(u) = \begin{cases} u\, p_u\, k_v \, \psi(p_u, p_c) & \text{for } 1 \geq u \geq 0 \\ u\, p_c\, k_v \, \psi(p_c, p_a) & \text{for } -1 \leq u < 0 \end{cases} \tag{4.32}$$

The upper variant represents the mass flow from the pressure source to the pressure chamber, where the control input u of the valve is ≤ 1 and ≥ 0. The lower term describes the flow from the chamber to the ambient outlet on the valve for $-1 \leq u < 0$. The qualitative mass flows of the loading and unloading process for different pressures are shown in fig. 4.7.

For the steady state at an operational point the valve needs to feed in as much air as is lost via the gap. With these equations all major pneumatic components have been described and can be linked to a complete pneumatic model.

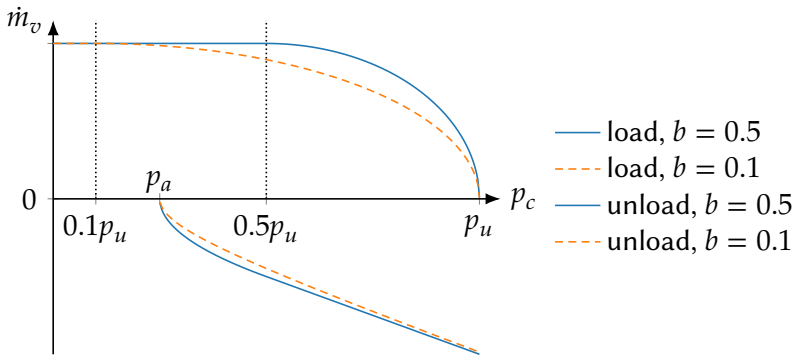

Figure 4.7: Qualitative loading and unloading mass flow for a valve, based on eq. (4.32). Two exemplary different critical pressure ratios are displayed: $b = 0.5$, $b = 0.1$

4.2.7 State Space Representation

For precision positioning the systems behavior around an operating point is of interest. A common tool to investigate the dynamics is the state space representation of the system [81]. A linear system with the inputs u and outputs $\vec{y}$ is represented as [82]:

$$\begin{aligned} \dot{\vec{x}}(t) &= \boldsymbol{A}\ \vec{x}(t) + \boldsymbol{B}\,\vec{u}(t) \\ \vec{y}(t) &= \boldsymbol{C}\ \vec{x}(t) + \boldsymbol{D}\,\vec{u}(t) \end{aligned} \tag{4.33}$$

In this application u is the input u from the valves mass flow eq. (4.32). From this the transfer function can be set up, which gives insight about the dynamics of the system. With this correlation, the influence of all design parameters can be analyzed.

The governing equations for this system are the ideal gas law from eq. (4.11) for the pressure chamber and the sum of forces on the piston.

$$p_c(t) = R_S T_c\, \rho_c(t) \tag{4.34}$$

$$m_L\, \ddot{h}_c(t) = A_c\, p_c(t) - A_c p_a - m_L g \tag{4.35}$$

Here an isothermal process is assumed (T_c is independent of the time t). This is a reasonable approximation for investigations considering only an operating point [83]. Otherwise, an additional energy equation would be necessary.

The systems state vector $\vec{x}$ is set to

$$\vec{x} = \begin{pmatrix} p_c \\ \dot{h}_c \\ h_c \end{pmatrix} \tag{4.36}$$

The output of the system is the pistons position h_c, hence the output equation is set to:

$$\vec{y} = \begin{pmatrix} 0 & 0 & 1 \end{pmatrix} \vec{x} + 0\,\vec{u} \tag{4.37}$$

The time derivative $\dot{\vec{x}}$ is derived from eqs. (4.34) and (4.35):

$$\dot{\vec{x}} = \begin{pmatrix} \dot{p}_c \\ \ddot{h}_c \\ \dot{h}_c \end{pmatrix} = \begin{pmatrix} R_S T_c \dot{\rho}_c \\ \frac{A_c}{m_L}(p_c - p_a) - g \\ \dot{h}_c \end{pmatrix} \tag{4.38}$$

The change of the airs density $\dot{\rho}_c$ is composed of its mass and volume change, see eq. (4.12):

$$\dot{\rho}_c = \frac{\mathrm{d}}{\mathrm{d}t}\left(\frac{m_c}{V_c}\right) = \frac{\dot{m}_c h_c - m_c \dot{h}_c}{A_c {h_c}^2} \tag{4.39}$$

The continuity equation states, that the change of an air mass $\dot{m}$ in a chamber equals the input minus the output mass flow. Here the valve feeds air into the cylinder and through the leakage air is discharged from the cylinder:

$$\dot{m}_c = \dot{m}_t - \dot{m}_g \tag{4.40}$$

Neglecting the transmission line effects, these two mass flows are given in eq. (4.26) and eq. (4.32). Further, m_c is replaced by the ideal gas law from eq. (4.11). This gives for $\dot{\vec{x}}$:

$$\dot{\vec{x}} = \begin{pmatrix} \frac{1}{A_c h_c}\Big(R_S T_c\Big(\dot{m}_t(u, p_c) - \dot{m}_g(p_c)\Big) - p_c A_c \dot{h}_c\Big) \\ \frac{A_c}{m_L}(p_c - p_a) - g \\ \dot{h}_c \end{pmatrix} \tag{4.41}$$

To set up the state space representation of this nonlinear system, it needs to be linearized at the point of operation. This point is set at an arbitrary height $h_c = h_c^*$, where the piston should rest ($\dot{\vec{x}} = \vec{0}$). The pressure at this point p_c^* is

derived from eq. (4.35) with $\ddot{h}_c = 0$:

$$p_c^* = p_a + \frac{m_L g}{A_c} \tag{4.42}$$

To keep the pressure and chamber height constant, the total air mass m_c can not change. Therefore, from eq. (4.40) follows

$$\dot{m}_v^*(u^*, p_c^*) = \dot{m}_g^*(p_c^*) \tag{4.43}$$

Therefore, these investigations are only valid for the loading case of eq. (4.32). Next, the partial derivative of $\dot{\vec{x}}$ at the operational point is set up. [82]

$$\boldsymbol{A} = \left.\frac{\partial \dot{\vec{x}}}{\partial \vec{x}}\right|_{\vec{x}^*, u^*} \qquad \boldsymbol{B} = \left.\frac{\partial \dot{\vec{x}}}{\partial \vec{u}}\right|_{\vec{x}^*, \vec{u}^*} \quad \text{with} \quad \vec{x}^* = \begin{pmatrix} p_c^* \\ 0 \\ h_c^* \end{pmatrix} \quad \text{and} \quad \vec{u}^* = u^* \tag{4.44}$$

Due to the large terms, $\boldsymbol{A}$ and $\boldsymbol{B}$ are generalized. Then the complete linearized state space representation is given

$$\boldsymbol{A} = \begin{pmatrix} a_{11} & a_{12} & 0 \\ a_{21} & 0 & 0 \\ 0 & 1 & 0 \end{pmatrix} \quad \boldsymbol{B} = \begin{pmatrix} b_1 \\ 0 \\ 0 \end{pmatrix} \quad \boldsymbol{C} = \begin{pmatrix} 0 & 0 & 1 \end{pmatrix} \quad \boldsymbol{D} = 0 \tag{4.45}$$

and the transfer function in the frequency domain $\mathcal{G}(s)$ is established via the input $\mathcal{U}(s)$ and the output $\mathcal{Y}(s)$: [82]

$$\mathcal{G}(s) = \frac{\mathcal{Y}(s)}{\mathcal{U}(s)} = \frac{a_{21} b_1}{s^3 - a_{11} s^2 - a_{12} a_{21} s} \tag{4.46}$$

From this equation the overall structure, like the integrating behavior, as well as the poles of the system can be read. Because of the definition by cases of $\dot{m}_v$ and ψ from eq. (4.32), a_{11} includes different terms depending on the pressure ratio. Further, the derivative $\mathrm{d}\psi/\mathrm{d}p_c$ is included in this term. The fully expanded state space representation can be found in appendix A.1.5.
This model depends on a large number of parameters, most of which have not been set yet. Using it to derive physical dimensions is difficult, due to the complex interaction of the terms. Estimations of these parameters may include high uncertainties but can give an overall idea of the system behavior. For a set of estimated parameters bode plots are shown in fig. 4.8. In the following design and development process this model is used and the behavior reestimated, when certain parameters were chosen.

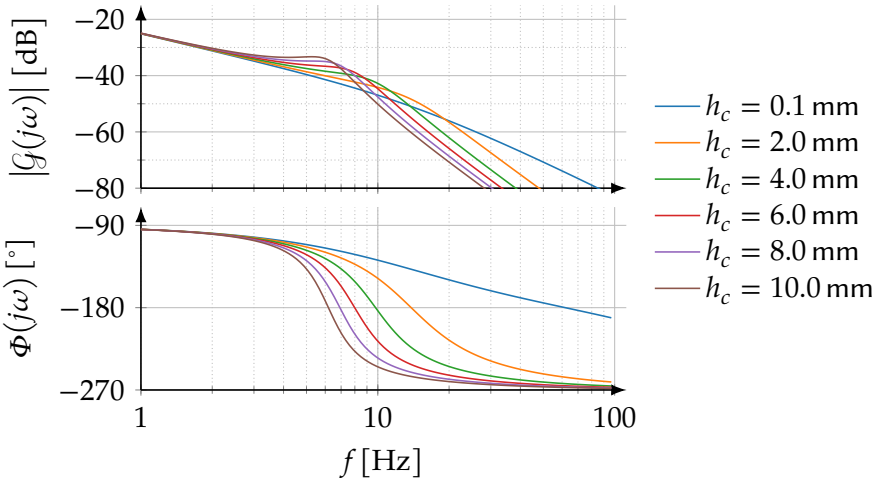

Figure 4.8: Magnitude $|\mathcal{G}|_{\text{dB}}$ and phase Φ plotted for a set of estimated exemplary parameters. With this set the chamber height has been varied.

4.2.8 Resulting Dimensions of the WFC

Through the stiffness and eigenfrequency analysis it was found that the non-displaceable volume V_{nd} should be minimized to increase the dynamics of the pneumatic actuator. The chamber diameter has no influence on these parameters.
An efficient throttling sealing is achieved by minimizing the width of the gap w_g. A long sealing gap also helps to reduce the leakage air flow but not as effectively as a reduced gap width. Increasing the chambers diameter d_c increases the area of the opening around the piston but also reduces the operation pressure, which drives the leakage flow. Therefore, no universal statement can be made.
The pneumatic transmission line damps and delays the air flow from the valve into the cylinder. Many parameters of the tube and its material are needed to determine this damping coefficient, whereas the delay is only proportional to the line length.
The throughput of a pneumatic valve is specified by its characteristic parameters C and b. Further the mass flow depends on the pressure ratio of upstream and downstream pressure. Large pressure differences result in large mass flows. To accomplish an equally large air flow for both loading and unloading processes of the cylinder, the operational pressure p_c^* should be situated somewhere in the middle between ambient and upstream pressure.
The study of available forces and accelerations suggested a piston diameter d_c

of 16.5 mm to realize an actuator with symmetric available maximum accelerations. For this configuration the equilibrium absolute pressure is about 3 bar. This complies very well with the valve flow goal on an intermediate equilibrium pressure since the upstream pressure is 5 bar and the ambient pressure about 1 bar. This dimension enables the device also to take up processing loads from future fabrication processes, which have not been specified yet. Finally the diameter was rounded up to 17 mm.

The cylinder also functions as the bushing for the vertical guiding. During operation this guiding experiences forces, which result in a bending of the bushing. This displacement needs to be small enough to not result in a crash between shaft and bushing. After investigating this load situation the wall thickness was set to 1.5 mm. Therefore, the minimum inner diameter for the upcoming voice coil design results in 20 mm.

4.3 Precision Drive

The precision drive component is used to dynamically actuate the load mass. These are the force components F_I and F_D from eq. (4.2) resulting in an expected load on the electromagnetic drive of $\pm 1.65\,\mathrm{N}$. The objective of this design task is to create a drive with minimal electrically dissipated power P for this given load. Following, the power equation for the Lorentz-force drive is derived and examined.

4.3.1 Derivation of the Force-to-Power Ratio

To minimize the power, its mathematical representation needs to be found, as it will give insight on what the important design parameters are.
Through the examinations from section 3.5.2 it was found that a voice coil drive with permanent magnets shall be used. In such an electromagnetic drive a coil is used to create the driving forces. This coil acts like a resistor, with its electrical power defined by

$$P = U I \tag{4.47}$$

where U is the voltage drop over the coil and I the electric current in the coil wire. Via Ohms law the electrical resistance is defined. It can also be calculated

from the wire length l_w, the wire cross-sectional area A_w and the electrical conductivity σ_w of the wire material [48]

$$R = \frac{U}{I} = \frac{1}{\sigma_w} \frac{l_w}{A_w} \tag{4.48}$$

This changes the power equation to

$$P = I^2 R \tag{4.49}$$

To create the required force a certain current in the coil is required. For these kinds of actuators (see fig. 3.6c) this relation is expressed in the Lorentz-force equation:

$$\mathrm{d}\vec{F} = I \int \mathrm{d}\vec{l} \times \vec{B} \tag{4.50}$$

The integral form describes what total force $\vec{F}$ acts on all differential wire pieces $\mathrm{d}\vec{l}$ which are situated in a magnetic field with the flux density $\vec{B}$ while conducting the current I. The local flux density can be different for every piece of wire. [48]
As in section 3.9 described a rotational symmetric drive is favored. To maximize the z-force component in such a drive the coil has to be wound around the z-axis. Thus, in this cylinder coordinate system a vertical force is created by the radial flux component B_r. Assuming the whole wire of the coil is subjected to the same (average) magnetic flux density, the equation simplifies to

$$F_z = I\, l_w\, B_r \tag{4.51}$$

The force sensitivity (or machine constant) k_F is given by the ratio of the output force to input current:

$$k_F = \frac{F}{I} = B_r\, l_w \tag{4.52}$$

It can be implemented in eq. (4.49):

$$P = \left(\frac{F_z}{k_F} \right)^2 R \tag{4.53}$$

Therefore, the output power depends on the required force. Bringing force and power to one side gives a central parameter of the drive:

$$F2P = \frac{{F_z}^2}{P} = \frac{{k_F}^2}{R} \tag{4.54}$$

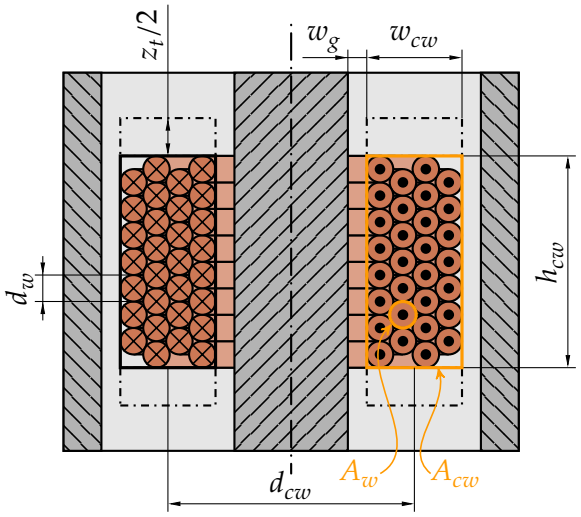

Figure 4.9: Geometry parameters of a coil. The dash-dotted line resembles the range of motion of the coil. w_g is the gap between the coil and surrounding parts and z_t the travel range of 10 mm. Here a orthocyclic winding type in the width direction is shown.

This parameter reflects how much electric power is needed to create a given force. There is no consistent convention, whether this quantity [10, 60, 71] or its square root [58, 84, 85] is named motor constant, actuator constant or actuator steepness. Following, the above defined variant is used as it is simpler to calculate the power from a given force and it gives non-square-root units. Further, it is named the force-to-power ratio or F2P, since the non-constant behavior is relevant for the upcoming analyses.
Hence, to minimize the power for a given force the F2P needs to be maximized. With eq. (4.48) and eq. (4.52) a more detailed representation is:

$$F2P = {B_r}^2 l_w \sigma_w A_w \tag{4.55}$$

The rectangular cross section of the whole coil is called the coil window. It has an area of $A_{cw} = w_{cw}\, h_{cw}$ as displayed in fig. 4.9.

The number of turns of the wire which fit into the coil window is denoted as N. The fill factor c_f is a ratio which describes how well the coil window is filled with the N wires:

$$c_f = \frac{N A_w}{A_{cw}} \tag{4.56}$$

Further the total wire length in the magnetic field l_w can be represented by adding the length of all wire loops. Here one average wire loop length is used.

This loop has a circular shape, thus its length is derived from the circles circumference [77]:

$$l_w = N \pi d_{cw} \tag{4.57}$$

where d_{cw} is the average diameter of the coil. With these additions F2P becomes

$$F2P = \pi \sigma_w c_f d_{cw} w_{cw} h_{cw} {B_r}^2 \tag{4.58}$$

Thus, the number of turns of the coil has no direct influence on the force-to-power ratio. The most relevant parameter is the radial flux density B_r since it is squared. Therefore, to maximize the F2P the highest priority has the increase of B_r. For circular wires the fill factor c_f is usually maximized using an orthocyclic winding scheme. It has a theoretical limit at $\approx$0.91. Further, the coils width, height and diameter should be maximized to improve the F2P. The conductor material with the highest σ_w is copper, the standard material for wires and coils.

In reality, the wire loops have different lengths and are subjected to different flux densities B_r. Additionally, B_r changes with the coils travel position z. Therefore, the integral from eq. (4.50) is transformed into a sum of all wire loops N. This results in:

$$F2P(z) = \pi \sigma_w c_f A_{cw} \frac{\sum_{i=1}^{N} \left(B_r(r_i, z_i)\ d_i(r_i) \right)^2}{\sum_{i=1}^{N} d_i(r_i)} \tag{4.59}$$

To further develop this equation for every turn i the B_r needs to be known. B_r can only be calculated via the application of Maxwell's equations [48, 86]. Therefore, the drive geometry has to be given.

In the following sections different drive topolgies are investigated. Thereby, different approaches are presented to calculate B_r and ultimately F2P for a given drive.

4.3.2 Preliminary Considerations of the Drive Optimization

In section 4.3.1 it was found that to minimize P the F2P-ratio needs to be maximized. From eq. (4.59) it can be seen that it only depends on variables of the drive. Thus, it can be used in a numerical optimization as the objective function. Due to B_r not being constant along the z-travel the F2P needs to be investigated over the full range. The goal is to create a drive with a minimum power output along the full range, therefore each variant is rated for their worst $F2P(z)$.

In section 3.9 the available design space for the precision drive is given. It is shaped like a hollow cylinder with a height $h_{\max}$ of 40 mm, an inner diameter $d_{\min}$ of 20 mm and an outer diameter $d_{\max}$ of 50 mm.

This examination is limited to topologies with only one coil to reduce the complexity of the required amplification electronics and the control system. Further, there is no technical difference whether the coil or the magnetic circuit is fixed to the slider. Mounting the coil to the slider has the advantage that the passive magnetic circuit is moving relative to the slider, resulting in no drag forces from the wires.
Still, many design options remain available. Only topologies with axial or radially magnetized magnet shapes are examined. Other arbitrary magnetizations are technically possible but need specialized fabrication methods and equipment and therefore, are not feasible for such drive systems. Radially magnetized ring magnets are not widely available in custom dimensions and magnetization strengths. But they can be composed of multiple identical ring segments, resulting in only very minor overall flux differences [87]. All investigations will assume permanent magnets with a remanence of 1.3 T, since these are widely available in customized shapes. Flipping the polarity of all magnets in one configuration has no effect on the absolute force, so they do not need to be investigated. But by turning a topology inside-out the F2P-ratio can possibly improve, so they are included in the examination.
Figure 4.10 shows the flux components B_z and B_r for an exemplary cylinder magnet. The axial component is strongest directly above the pole surfaces, whereas the radial component is strongest at the corners of the poles. Hence, placing the coil in these regions will result in the strongest forces.

Since the drive will be rotationally symmetric the model equations can be simplified. Via preliminary investigations it was found that the optimization tends to use the whole available design space. Therefore, the number of optimization variables (the dimension of the optimization problem) can be reduced significantly, but additional constraints need to be introduced. This also results in the gap between the coil and surrounding parts being minimized. The gap was set to 0.5 mm to accommodate geometric part and mounting tolerances.
Further, it was found that vertically symmetric topologies are beneficial. When a topology is asymmetric usually one of the coils extremal position (zero or 10 mm) has an inferior F2P than the other. By using a symmetric geometry this poorer extremal is improved, while the other is worsened. Hence, for both positions the F2P will have the same intermediate value, improving the total performance. Additionally, only one half of the travel range has to be investigated.

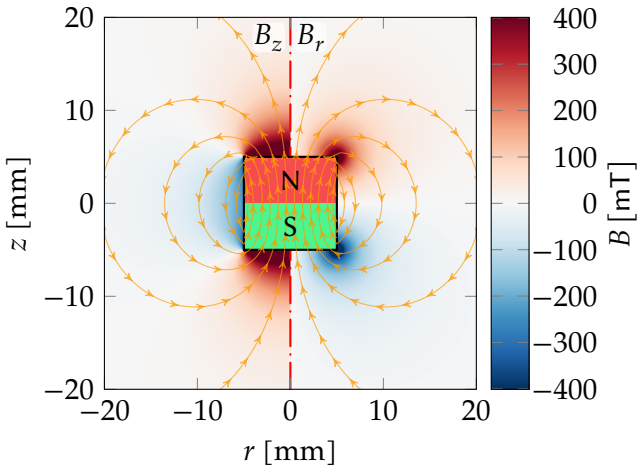

Figure 4.10: Axial B_z and radial component B_r of the magnetic flux density for a ∅10×10 mm² permanent magnet with 1 T remanence.

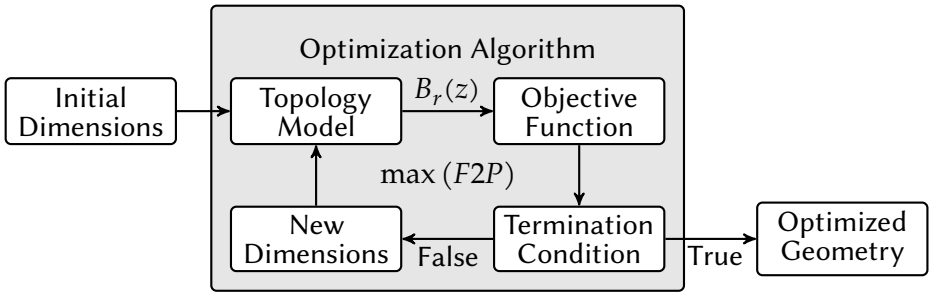

Figure 4.11: Optimization procedure of one drive topology.

In fig. 4.11 the general optimization procedure for one topology is shown. The topology model is fed with an initial set of dimensions for its design parameters. After the radial flux $B_r(z)$ in the coil window was calculated eq. (4.59) is evaluated as the objective function. Then the optimization algorithm decides, whether its termination condition is met. If not, it generates a new set of dimensions, based on the previous sets and their results. Then the procedure is re-run.

The upcoming graphics 4.12 and 4.15 display one half of the cross-sectional view of the rotational symmetric arrangement. The available design space is marked with an orange dashed line. Due to its ring-shaped space, all permanent magnets will be ring magnets. The magnetic north poles are colored in red and the south poles in green. The coils cross section (coil window) is patterned with a crosshatch. Additionally, all modifiable geometry dimensions are marked. The dash-dotted line shows the upper and lower travel position of the coil.

For permanent magnets analytic equations were developed in [88] and more compiled in [60, 85]. With these the flux density can be calculated in the vicinity of the permanent magnets. These equations can only be applied for drives without ferromagnetic materials (iron-free).
For electromagnetic drives with iron, magnetic equivalent circuit models [86, 89, 90] are a common tool to estimate their performance. Their accuracy depends primarily on the correct modeling of the air gap and the fringing flux. These equivalent circuit models can only consist of the limited number of elements which have been developed. Most of these elements are merely a rough estimate for the actual flux distribution [89]. Further, no standard method exists to model the changing flux in a moving coil.
With the Schwarz-Christoffel mapping a conformal transformation [60, 91] can be applied to estimate the flux density in an air gap [92]. This method does not model any saturation effects in the ferromagnetic material.

Due to these limitations of the named methods, the Finite Element Method (FEM) will be used since it is a proven and precise (but computationally heavy) tool.

4.3.3 Iron-Free Topologies

Iron-free topologies have the advantage of making the whole design space available to the flux creating magnets and the force creating coil. Additionally, the drive will not be subjected to any hysteresis effects. The downside is that the flux can not be focused as effectively as with ferromagnetic parts. Furthermore, the stray flux may disturb the planar drive (described in req. 17).

The variants in fig. 4.12 are considered for the precision drive application. Some of these variants were investigated in [93] for loudspeaker applications.
As from fig. 4.10 can be seen, the strongest field is above the pole surfaces. To utilize this field region for force creation a radial magnetized ring sits either inside or outside the drive coil, see figs. 4.12a and 4.12b. This is the most basic topology since only one magnet is used.
The radial flux from axial magnets can be used by positioning the coil left or right of a pole surface, as in figs. 4.12c and 4.12d. The radial flux density is increased by opposing two identical magnets with the same pole.
The above described variants can be combined by applying a radial magnet inbetween the axial magnets. This resembles a segment of a Halbach array structure in a rotational symmetric way [94, 95], which is known for its high flux densities.

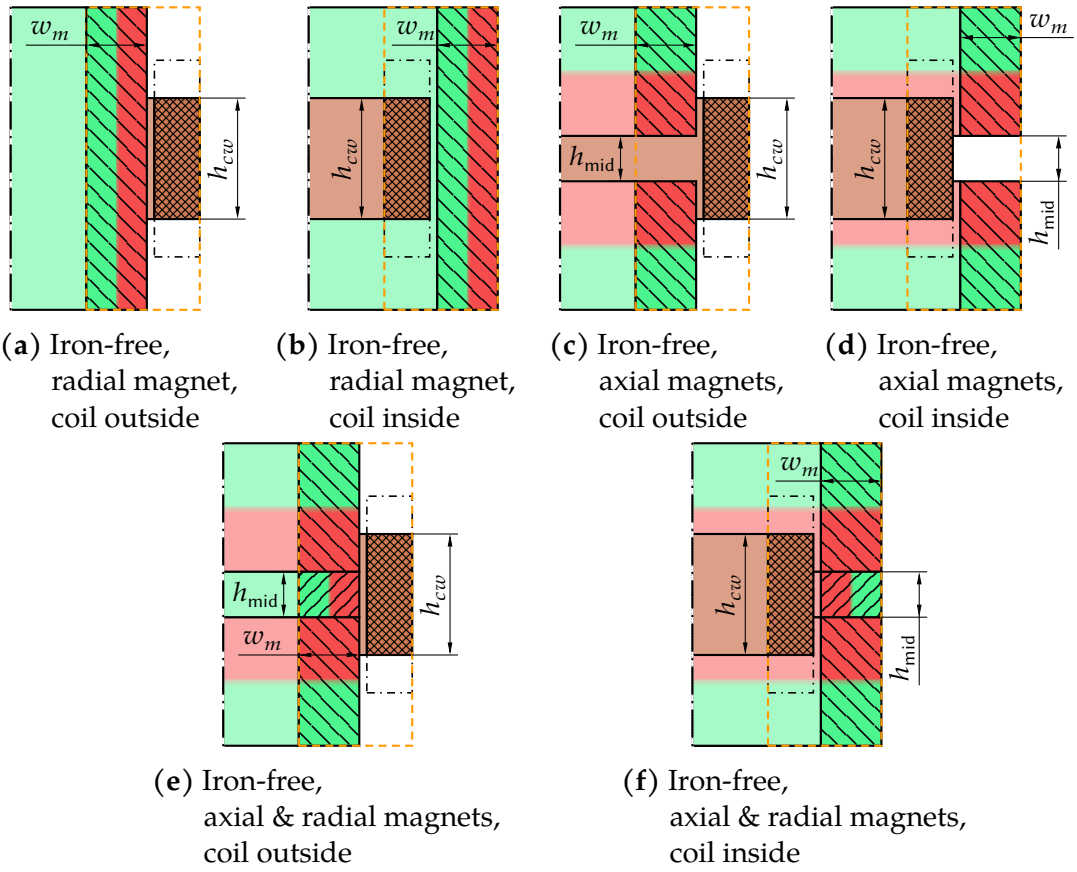

(**a**) Iron-free, radial magnet, coil outside

(**b**) Iron-free, radial magnet, coil inside

(**c**) Iron-free, axial magnets, coil outside

(**d**) Iron-free, axial magnets, coil inside

(**e**) Iron-free, axial & radial magnets, coil outside

(**f**) Iron-free, axial & radial magnets, coil inside

Figure 4.12: Possible iron-free drive topologies

All these variants are shown with either the coil or the magnets on the inside. Further, a coil could be enclosed by magnets on both sides e.g. merging fig. 4.12a and fig. 4.12b. These variants were not investigated, because the magnets and coil will have very small wall thicknesses and widths, which makes them difficult to manufacture.

In [88, 96] the equations for the flux density components B_r and B_z of radially and axially magnetized ring magnets are given for an arbitrary point $\mathcal{P}(r, z)$. The equations for the axial magnetized magnet require the calculation of the complete elliptic integrals of the first and second kind, as well as the Heuman's Lambda function, while the radially magnetized magnets equations include additionally the elliptic integral of the third kind. Using analytic models over FEM is very attractive, because a deeper insight into the systematic relations can be obtained. Further, using analytic equations for numerical optimization gives a larger variety of feasible algorithms (e.g. gradient based) which possibly converge faster. In general the computational load is dramatically smaller

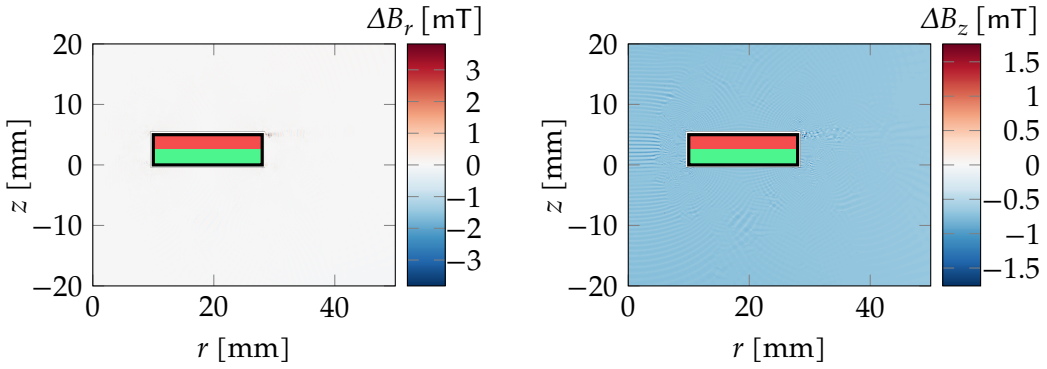

Figure 4.13: Difference in B_r and B_z between an analytic and an FEM calculation. In B_r the deviates are only small local spots. In B_z a deviation of about $-0.5\,\mathrm{mT}$ can be seen in the whole investigated region.

compared to FEM, allowing the optimization of more variants in the same time. This is because in analytic models only the radial flux component inside the coil window has to be calculated, whereas in FEM all magnetic quantities have to be determined in the whole spacial region on a fine mesh. Therefore, analytic models in optimizations converge dramatically faster and are not prone to numerical noise introduced by a quantified mesh. This faster calculation time enables the usage of optimization algorithms which require a more frequent calculation of the objective function, possibly increasing speed benefit.
The implemented equations were validated with FEM simulations, resulting in a very good agreement (see fig. 4.13) with overall deviations being below 1 mT.

The analytic field calculation of the radial magnetized magnets was (due to the calculation of the third elliptic integral) very time intensive, negating the run time benefit compared to FEM. Different numerical implementations of this integral [97, 98] have been tested but did not result in a speed-up of the calculation while maintaining the required precision.

For the axial topologies (figs. 4.12c and 4.12d) the *Sequential Least Squares Programming* [99] optimization algorithm was used. This gradient-based method is very well suited for such nonlinear constrained optimizations [100] and has proven to be the fastest converging and most robust algorithm, compared to other available methods [101]. Multiple optimization runs with randomized initial values are shown in fig. 4.14 with different colored lines. Taking different starting points in the feasible region is a practice to make sure, that the global optimum is found instead of a local one. [100]
As stated above, with the first iteration the optimizer fills out the design space. It minimizes the inner diameter of the magnet d_{im}, maximizes the magnet height

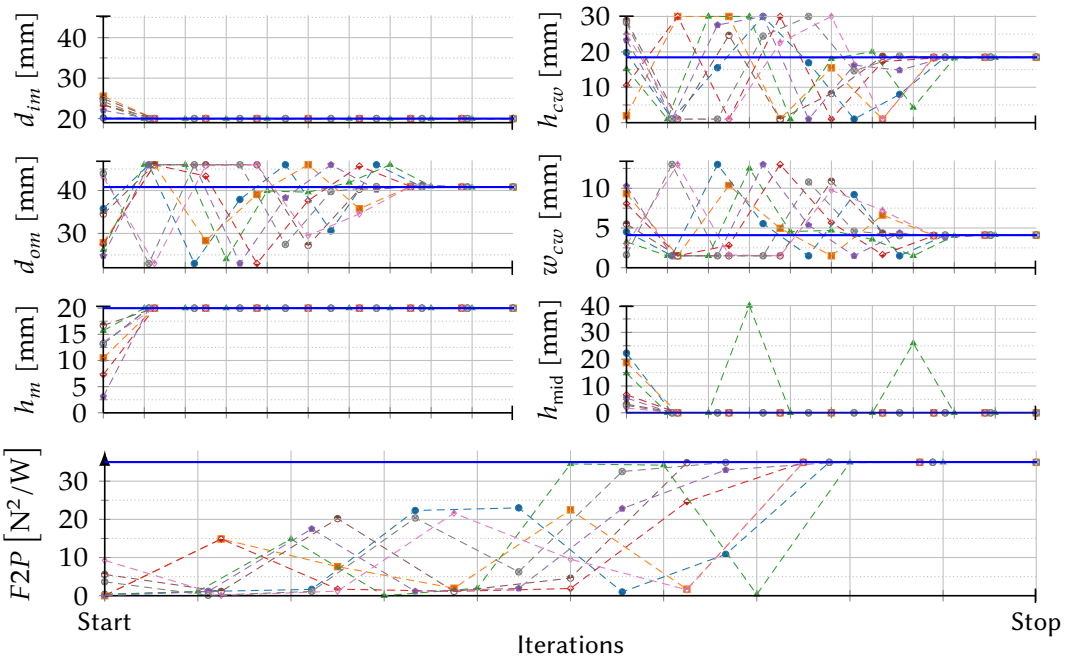

Figure 4.14: Eight optimization runs with different random initial values of the topology from fig. 4.12c. The blue lines show the optimal value for each variable. Every marker resembles one iteration step. The total calculation time was about 70 s.

h_m and reduces the gap between the magnet poles h_{mid} to zero. After the first few iterations, the optimizer tries to find the best fit for h_{cw}, d_{cw} and d_{om}. With only a few further iterations it quickly converges to the global optimum (blue lines for every parameter). Some outliers appear (dashed green iteration in h_{mid}), which happens most likely due to numerical noise in the gradient calculation.

As displayed for the axial magnets inside the coil (fig. 4.12c) the best F2P is 35 N²/W. The variant from fig. 4.12d with the coil inside the magnets achieves a best F2P of 9.7 N²/W (not displayed). Compared to the first topology it is significantly worse because of the very small radial field inside the rings. The field is so low because the radial components of opposing magnet parts cancel out inside each ring, which is especially significant for small diameters.

For the remaining topologies (fig. 4.12a, b, e, f) magnetostatic finite element models were set up. Here the mesh design needs to be considered especially in the coil, the gap and high flux gradient regions such as corners of permanent magnets. Since the field calculation of the objective function is computationally

Table 4.1: Resulting dimensions from the optimization of the iron-free topologies. The magnet types are *R* for radial and *A* for axial magnetization. The magnets position is given with *i* for inside and *o* for outside of the coil.

In fig. 4.12	Magnet	Dimension [mm]			*F2P* [N²/W]
		w_m	h_{cw}	h_{mid}	
a	Ri	3.6	19.5	—	1.9
b	Ro	8.4	8.4	—	1.8
c	Ai	10.4	18.5	0	35.0
d	Ao	8.3	17.0	0	9.7
e	ARi	10.4	18.5	0	35.0
f	ARo	8.3	17.0	0	9.7

intensive, the gradient free optimization algorithm Nelder-Mead was used. Further, it is very robust and well suited for such continuous problems.

The variants with radial magnets from figs. 4.12a and 4.12b are not competitive. The single radial magnet with the outside coil reaches an optimized F2P of only 1.75 N²/W. Whereas the optimized variant with the coil inside the magnet results in approximately the same 1.78 N²/W.
For the Halbach-like topology from fig. 4.12e depending on the initial geometry a local optimum was found where the inner radial magnet is 4 mm high. This results in an F2P of 28.2 N²/W, whereas the global optimum is found by reducing the inner magnet height to zero. Thus, the topology becomes identical to the one with only axial magnets. The same applies for the variant with the coil inside from fig. 4.12f. It has the same global optimum as the topology with only axial magnets resulting in 9.7 N²/W.

The resulting dimensions and the global maximum F2P of all these topologies are listed in table 4.1.

4.3.4 Optimization of Topologies with Back Iron

Utilizing ferromagnetic parts in a voice coil drive allows a better shaping and focusing of the magnetic flux [102]. Further, stray flux outside the drive can be reduced dramatically. But hysteresis and saturation effects from the ferromagnetic parts need to be considered, as they may disturb the performance of the drive. By introducing iron on the inside of the coil the inductance of the coil

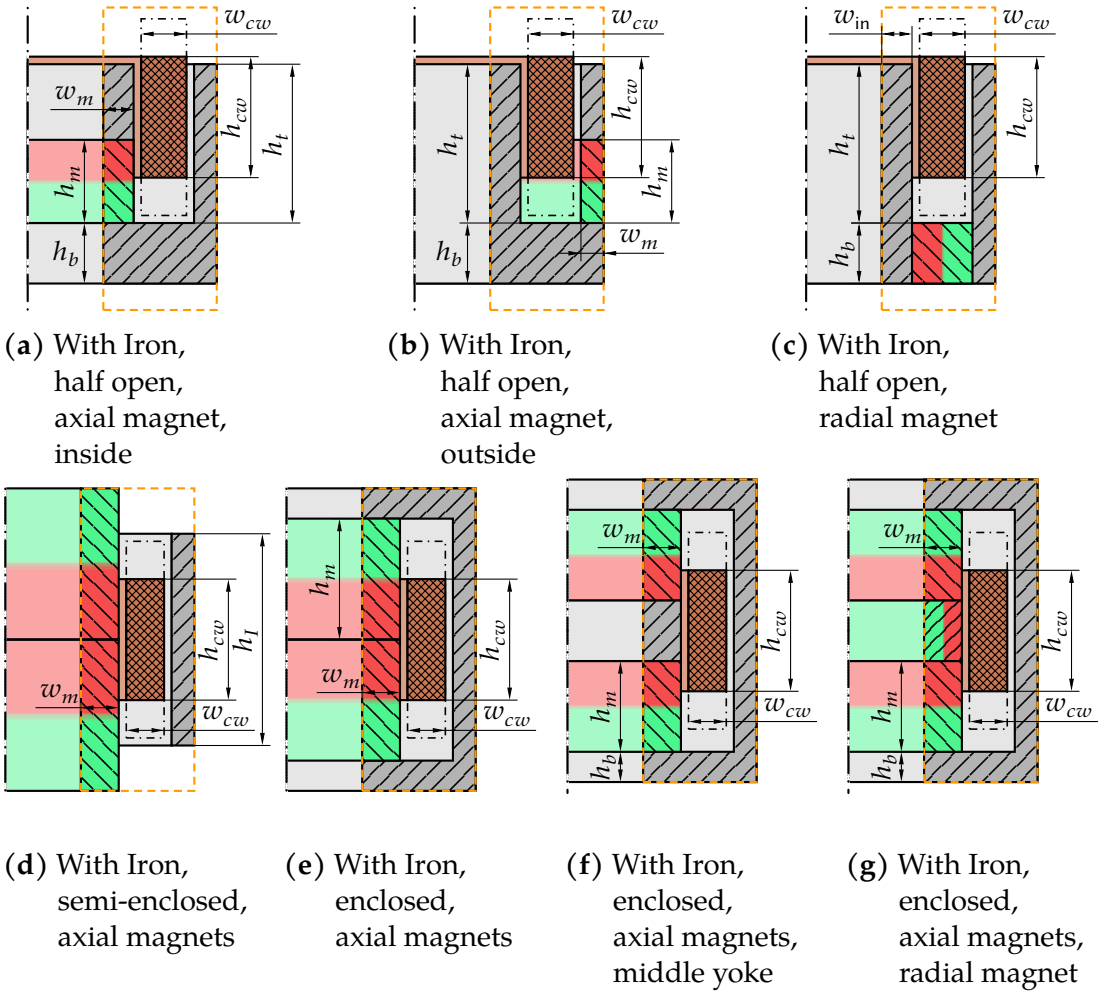

(**a**) With Iron, half open, axial magnet, inside

(**b**) With Iron, half open, axial magnet, outside

(**c**) With Iron, half open, radial magnet

(**d**) With Iron, semi-enclosed, axial magnets

(**e**) With Iron, enclosed, axial magnets

(**f**) With Iron, enclosed, axial magnets, middle yoke

(**g**) With Iron, enclosed, axial magnets, radial magnet

Figure 4.15: Investigated drive topologies with ferromagnetic parts

increases dramatically, raising the load on the drive electronics and decreasing the dynamics (see appendix A.1.6). If the inductance changes with the vertical position, for high currents nonlinear force components are introduced [86, eq. 3.62]. Therefore, topologies with little to no iron inside the coils are preferred.

All examined topologies are shown in fig. 4.15. The variants from figs. 4.15a to 4.15c resemble more classic voice coil actuators like [58], as they can be obtained preconfigured from suppliers. From the iron-free topologies the variant in fig. 4.15d is derived. It is an intermediate step to the fully enclosed variants: The figs. 4.15e to 4.15g show variants in which the coil is surrounded by magnets and iron parts. Compared to the classical voice coil variants they are vertically symmetric. By enclosing the coil in iron the magnetic circuit is closed and the outside flux leakage reduced.

For these investigations the same magnetostatic optimization and FEM modeling is used as in section 4.3.3. In contrast to the previous variants, a lot more geometry parameters are free to chose, increasing the dimension of the optimization problem. Additionally, a material for the ferromagnetic parts needs to be set up. A generalized soft iron material is used, with a saturation at about 1.5 T (B/H-curve in fig. 5.3). The exact material will be selected later in the design process (see section 5.1.2 and fig. 5.3). Due to the saturation effect an iterative flux calculation is needed, which increases the calculation time, resulting in an average optimization time of about 15 min.

The optimized classic half open voice coil variant from fig. 4.15a results in a maximum F2P of 20.2 N^2/W, whereas the topology with the magnet on the outside (fig. 4.15b) converges to 15.2 N^2/W. In both topologies the optimizer creates very large coils with heights above 21 mm and very large magnets with heights above 22 mm. The pole piece above the magnet is left quite small with a height between 4 and 7.5 mm. The region with the highest flux density is always at this poles surface facing the coil. So in both variants the coil overhangs the pole piece and covers this high flux density region at every point in the z-travel. Apparently, it is more beneficial to concentrate the flux into a smaller region, in which it penetrates only few windings, than to spread the flux over more windings but with a reduced density. Further, the iron piece that is opposed to the magnet is reduced in width down to the point where it saturates. Therefore, the remaining width is maximized and split between the magnet and the coil.

The half open topology with the radial magnet (fig. 4.15c) achieves a larger F2P of 26.1 N^2/W. Surprisingly, it performs a lot better than the iron-free topologies with a single radial magnet. Due to the iron the flux is kept from leaking over to the opposing side of the magnet. Therefore, instead of possibly reducing the axial flux there, it contributes to the higher flux density in the coil.

The topology from fig. 4.15d originates from the best iron-free variant. To further focus the flux and to reduce the stray flux in the environment the magnets and the coil are surrounded by an iron shell. Due to this additional part and the second gap the available width for the magnet and coil are reduced. Therefore, it performs worse with 18.5 N^2/W than the iron-free alternative.
The logical next step is to close the magnetic circuit with iron parts on the top and the bottom, as shown in fig. 4.15e. The disadvantage of the reduced available space for coil and magnets is compensated completely as an F2P of 35.7 N^2/W is reached. A spot with a very high B_r is created at the magnets outside diameter, where both magnets meet with their poles.

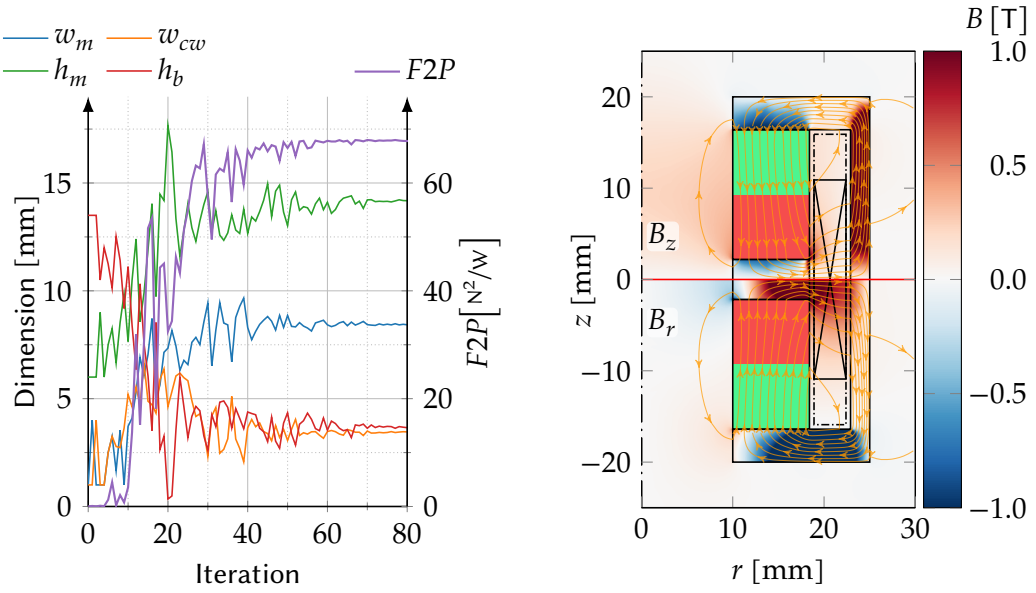

(**a**) Optimization procedure

(**b**) Resulting dimensions and flux distribution

Figure 4.16: Optimization process and resulting field distribution of the topology from fig. 4.15f with middle iron yoke

To further increase this flux the enclosed variants with a middle iron yoke (fig. 4.15f) and a middle radial magnet (fig. 4.15g) were investigated. The implementation of an iron ring between the magnets helps to reduce the stray flux on the insides of the rings and leads it through the coil as well. The optimization takes about 60 iterations for this topology to find the maximum F2P, which can be seen in fig. 4.16a. The following iterations achieve only minor improvements. With this middle ring (height of 4.4 mm) two hot spots are created with a B_r on the coils surface of up to 1.3 T. This can be seen in fig. 4.16b, where the top part displays the B_z component and the bottom part the B_r component. With this setup the F2P is dramatically improved to 68 $\mathrm{N^2/W}$.
Replacing the iron ring with a radial magnet results in the topology from fig. 4.15g. It converges to a very similar optimum with an F2P of 73.6 $\mathrm{N^2/W}$. The height h_b of the top and bottom iron are reduced significantly, resulting in the saturation of these parts, which leads to a larger stray flux.
The resulting geometries and final objective values for the iron topologies can be found in table 4.2.

The topology from fig. 4.15g achieved the best F2P by just a slight margin. But its complex magnet setup creates difficulties to fix the repelling magnets together.

Table 4.2: Resulting dimensions from the optimization of the topologies with iron parts. The *Iron*- and *Magnet*-columns describe, where the magnets and iron parts are situated relative to the coil. The following shorthands are used: *i*: inside, *o*: outside, *a*: above, *b*: below.

In fig. 4.15	Magnet	Iron Pos.	Dimension [mm]						*F2P* $[\mathrm{N^2/W}]$
			$w_{m/\mathrm{in}}$	h_m	w_{cw}	h_{cw}	h_b	$h_{t/I}$	
a	Ai	iob	8.7	24.7	3.7	21.8	9.3	29.1	20.2
b	Ao	iob	4.5	22.8	3.4	25.0	4.4	30.2	15.2
c	Rb	io	5.2	—	6.7	16.1	18.9	17.9	26.1
d	Ai	o	8.0	—	3.7	18.2	—	32.6	18.5
e	Ai	oab	8.3	16.7	3.7	—	—	—	35.7
f	Ai	ioab	8.4	14.2	3.5	—	3.6	—	68.0
g	ARi	oab	8.2	11.7	3.7	—	2.5	—	73.6

Additionally, the increased stray flux will influence the planar drive. The magnet setup from topology fig. 4.15f has dramatically reduced repelling forces (see section 5.1.2). Further, the stray flux is comparably low. The magnetic field outside the enclosure drops logarithmically: At 10 mm outside of the shell the absolute flux density B is 10 mT and ≈1.5 mT at 30 mm (the approximate distance to the planar drive magnets). Due to these reasons the topology in fig. 4.15f is selected as the best overall suitable for the precision drive.

4.3.5 Parameter Study on the Coil Wire

After finding the best topology the magnet and iron dimensions are set. With these conditions the size of the coil window is found but the wire size needs to be selected. This wire size has an influence on various drive parameters, including the F2P. An specialized analog amplifier is used to drive the coil. It has a current output of −1.3 A to +1.3 A and a voltage range of −20 V to +20 V.

The wire diameter d_w can be selected from a list of available wires [103]. Each wire is coated with a thin layer of electrical isolation, so the true diameter of the conductor is slightly smaller than d_w.
Further, different methods to wind the wire into the coil window are possible. The simplest method, the wild winding, reaches only very minor filling factors c_f and is not considered. The simplest but organized method is the rectangular winding, where every wire sits exactly on top of the underling turn. The winding

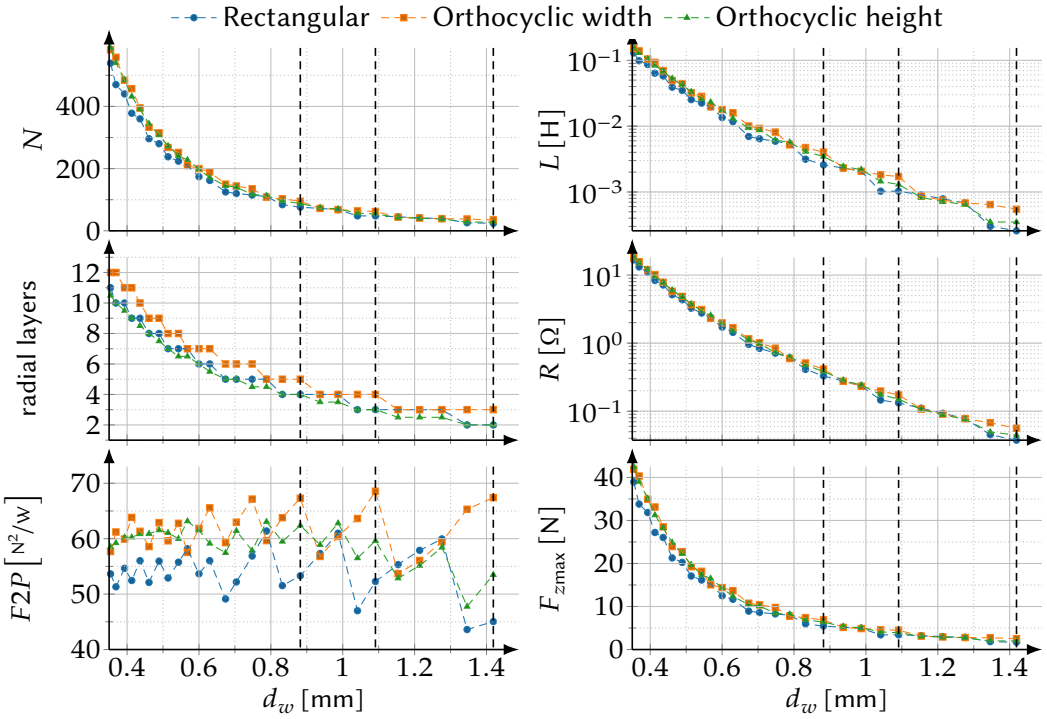

Figure 4.17: Selected coil parameters calculated via a parameter sweep of all available wire diameters and the three winding variants.

method which usually achieves the highest filling is the orthocyclic winding, as previously shown in fig. 4.9. Further, the orthocyclic winding can be layed into an rectangular winding window in two orientations. These three variants are investigated and their resulting parameters are shown in fig. 4.17.

First and foremost with a larger wire diameter d_w fewer windings fit into the coil window, reducing the number of turns N. Thus, c_f can be determined which correlates strongly with F2P; the three wire diameters with the best F2P are marked with dashed lines. Since only an integer number of wires fit into the coil window, the function is discontinuous. The wire length l_w is accountable for the resistance R eq. (4.48) and the inductance L. With these parameters the dynamic behavior of this drive can be modeled. For a given power amplifier with a maximum current output $I_{\max}$ and voltage output $U_{\max}$ a limiting driveable resistance can be determined. From L and $U_{\max}$ the current loading can be simulated. This rate of change in current $\dot{I}_{\max}$ directly gives a force rate ($\dot{F}_z$) and with the load mass m_L the maximum jerk $j = \dot{a}$ (rate of acceleration change) can be determined, see appendix A.1.6. This maximum jerk is a measure for how fast the drive can react on random disturbances. The wire length l_w further

influences the drives force sensitivity from eq. (4.52). With the amplifiers $I_{\max}$ the maximum output force can be calculated. This has to exceed the minimal requirement of 1.65 N from fig. 4.1b, giving another constraint.
For most wire dimensions the orthocyclic width-wise winding is the superior one. It is also the simplest and proven winding method. Further, the wire diameter $d_w = 1.091\,\text{mm}$ was selected. With its good fill factor of 70 % it achieves one of the highest F2P while also having low resistance and inductance. One important criterion for the implementation of the coil in the design is the number of winding layers of the coil. If a coil has an uneven number of layers, one of the contacting wires will end up at the bottom, the other at the top side. To route them together, it is beneficial to have a even number of layers, so both leads contact the coil on the same face.

With this resulting coil and the maximum amplifier current the load can be driven with a force of up to 4.5 N. This force translates to an acceleration of $1\,\text{m/s}^2$ ($\approx 0.1g$), while introducing 0.3 W of heat.

4.3.6 Investigations on the Thermal Behavior

During operation the electric resistance of the copper wire results in a heat flow. A small cooling channel shall be integrated into the design to keep this heat from dissipating into the environment. Since, the coil sits between the inner magnet stack and the outer iron shell, the only place to contact the coil is the top or bottom surface. To estimate the effectiveness of this cooling system, its thermal behavior was modeled.
The single wire loops are separated by a thin layer of electrically isolating material, which also acts as a thermal insulation. Modeling each wire and the insulation inbetween is not feasible. The whole coil volume can be abstracted into a single homogeneous domain with the equivalent model parameters from [104, 105]. The single domain is set up with an equivalent thermal conductivity in axial and radial direction of $\approx 1\,\text{W/m K}$. The thermal capacity is not relevant, since only stationary analyses are conducted. Thermal parameters for the used Neodymium-Iron-Boron magnets are found in [106]. Convection and radiation were not modeled, making this a worst case simulation. The ambient and coolant temperature was set to 21 °C.
For the analysis shown in fig. 4.18 the highest possible load was assumed: The coil domain was set to the maximum power output of 300 mW. In this unlikely case the hottest point of the coil will heat up about 2.2 K. The heat flux $\dot{Q}$ into the cooling channel is determined from the simulation. It was identified that

about 46 % of the induced heat can be discharged via the cooling system, even though only 9 % of the coil windows outer surface are directly in contact with the cooling system. This is most likely due to the insulation effect of the air surrounding the coil, which hinders the heat from leaving the coil domain via its surface.
Assuming, that the coil needs to permanently generate the dynamic components of the total load ($\pm 1.65\,\mathrm{N}$, see section 4.3) the maximum temperature increase in the system is just 0.3 K. The most realistic case is that the coil only needs to counter the disturbances, estimated with about 0.15 N. This results in the hottest point (inside the bottom of the coil) heating up by just 2.5 mK. This is still a conservative assumption since the disturbance force is a random quantity and not a permanent one.

No additional design space is available to accommodate the cooling channel, thus the coil height needs to be reduced. Therefore, the magnet system is adapted and the optimization rerun with the new geometry and constraints. The final resulting parts are shown in chapter 5.

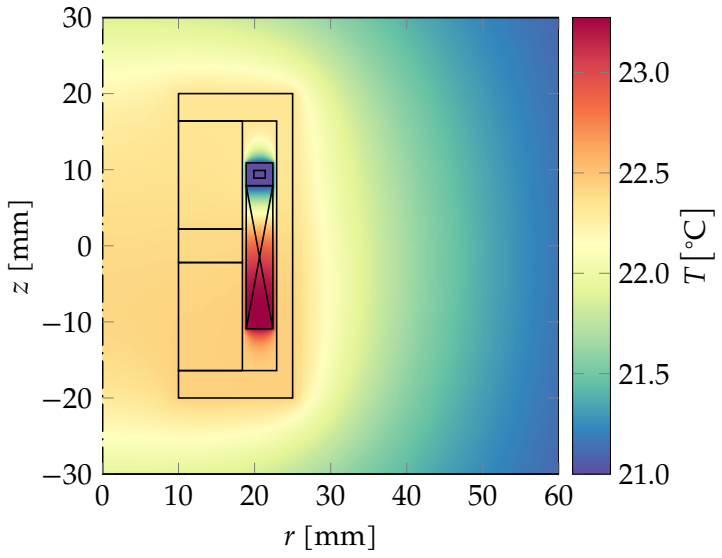

Figure 4.18: Simulation of the thermal behavior of the electromagnetic drive system for an input power of ≈300 mW and an ambient and coolant temperature of 21 °C.

4.4 Aerostatic Vertical Guiding

In this section simulations are used to check, whether the desired guiding geometry is capable of carrying the expected loads. For this linear guiding an aerostatic bushing type was chosen. In section 3.9 was decided, that the bushing shall have the same diameter as the pneumatic cylinder, namely 17 mm. The presented simulations and data are mainly results from [107], which based its models on [108].

First the expected loads are identified. The vertical guiding will have no permanent load (the load from tilting is neglected due to the small tilting angles). Only the sliders motion with the inertia of the base assembly of the LAU creates a force on the guiding, see fig. 4.19. This load results in a radial force, as well as in a torque on the bushing. The mass of the base assembly was estimated conservatively with 1 kg and a safety factor of 2 is used. Hence, the maximum planar acceleration of 250 mm/s^2 gives a radial force of 0.5 N. The worst case lever length h_l is estimated from conceptual CAD implementations with 35 mm, where the LAU is fully extended ($z = 10\,mm$), giving a torque of 35 mN m.

In the simulations from [107] different air feeding types and dimensions of bushings were examined. The resulting pressure distributions for the two radial and tilting case can be seen in fig. 4.20. A quarter model was used to simulate the radial load via an eccentric shaft. A maximum radial load of circa 25 N and a stiffness of about 3.3 $N/\mu m$ were derived. For the tilting case a simulation of a half model was set up with an angular deflection of 1 mrad. This gave a maximum moment of ≈850 mN m with a stiffness of 0.8 $N\,m/mrad$. Thus, the presumed dimensions are sufficient to handle the small loads. With these large reserves the LAU can be lifted and turned over, without risking a crash between the bushing and the shaft.

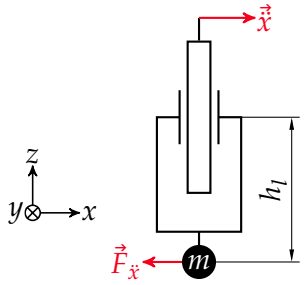

Figure 4.19: Radial load on the vertical guiding

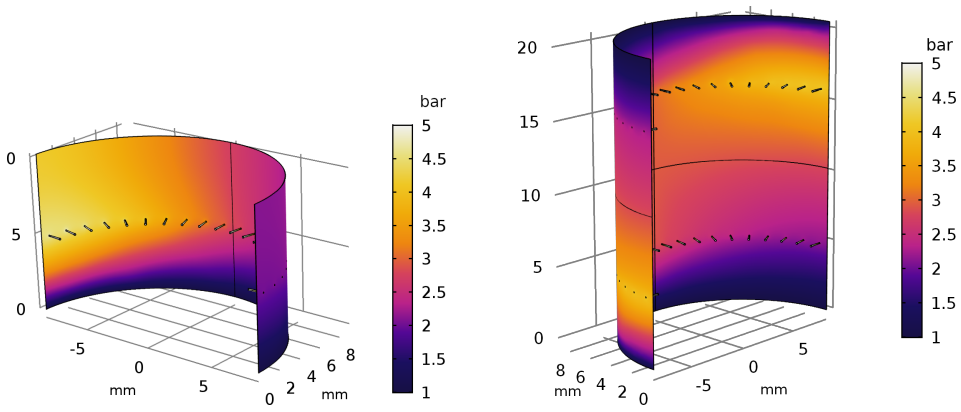

(**a**) Quarter model, radially load (**b**) Half model, tilting load

Figure 4.20: Pressure distribution in the air gap between bushing and shaft [107]

All major components of the LAU are modeled and their functional dimensions are set. Based on these results, the following chapter describes the design of the physical parts.

Chapter 5

Mechanical Design of the Functional Assemblies

The previous chapter derived the functional dimensions for the WFC and electromagnet drive. The next step in the design process is the mechanical design and integration of the components into the design space based on the derived dimension.

The results of this design process can be seen in fig. 5.1. The LAU is shown at its bottom (a) and top most position (b) of its vertical travel. In fig. 5.1c a cut-away

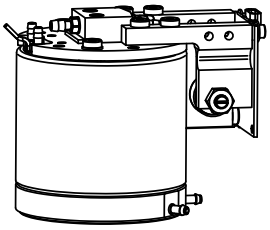

(**a**) LAU at its bottom position

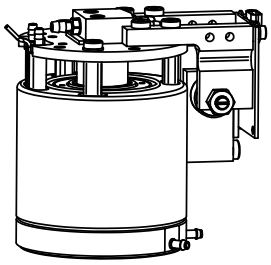

(**b**) LAU at its top position

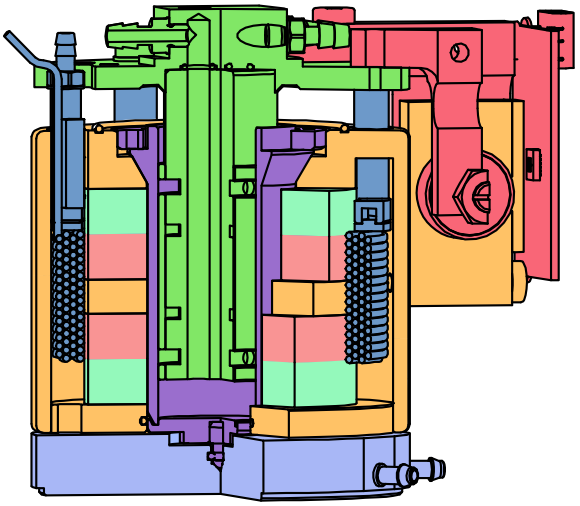

(**c**) Cut-away view of the LAU at its middle position. Each subassembly is colored corresponding to fig. 3.12.

Figure 5.1: Outside and cut-away view of the LAU at different travel positions.

view of the LAU is displayed, where its subassemblies are colored according to fig. 3.12.
The LAU consists of two main assemblies. The top assembly is fixed to the slider and therefore executes no relative motion to it. Its parts are colored in red, green and dark blue. The second assembly is the base assembly, which remains on the stator but moves with the slider along in the *xy*-plane. It is formed by the planar aerostatic bearing pad on the bottom in light blue, the permanent magnets in red and green, the orange and the purple parts.

The following sections illustrate these assemblies and subassemblies and describe their main features and central design decisions.

5.1 Base Assembly

The parts of the LAUs base assembly can be seen in fig. 5.2. The following descriptions will refer to the parts names as they are labeled in this graphic. All

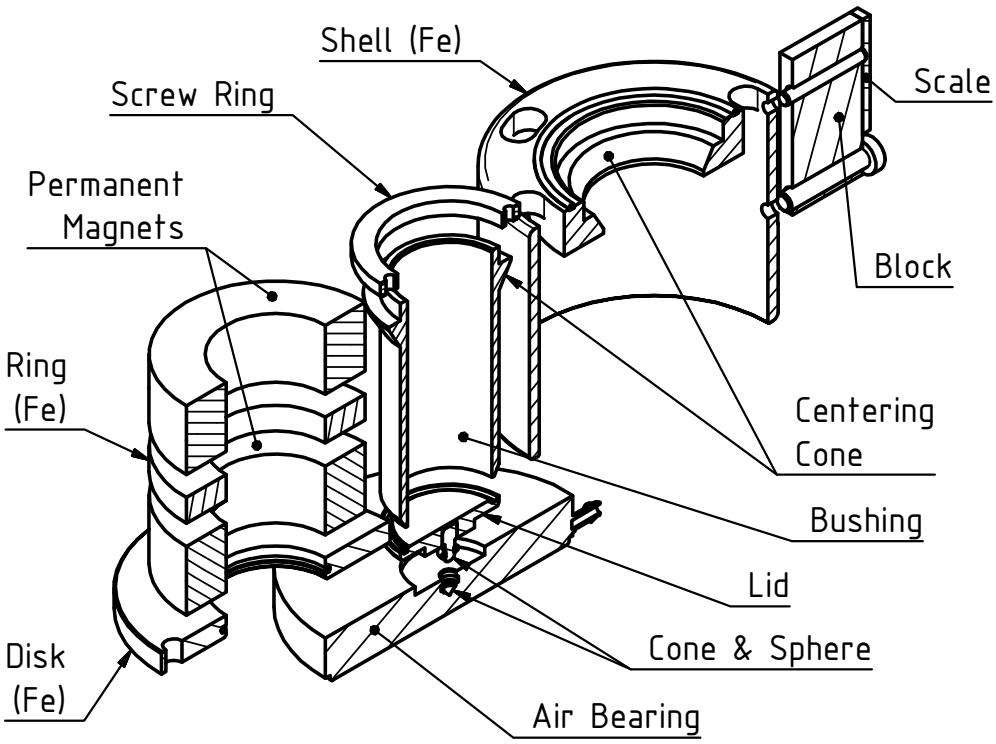

Figure 5.2: Explosional, cross-sectional view of the components of the passive base assembly

parts are non-ferromagnetic except the parts noted with *Fe*. Their material is selected in section 5.1.2.
During vertical motion of the slider, the base assembly rests on the stator. Thus, the slider moves relative to the base assembly. This assembly is composed of all the passive parts of the functional components. This is done to avoid the introduction of disturbing forces by moving and flexing wires and hoses. The only hose that is connected to the base is the air supply for the planar air bearing. This bearing pad has a cone shaped recess in its center. A spherical pin sits in this groove which gives the bearing the required tilting freedoms [39] to adjust itself to the underlying surface. This way a cardan joint is formed, which is very compact, simple to manufacture and assemble and very resistant to overloads. The following subsections describe the remaining subassemblies in detail.

5.1.1 Bushing and Pressure Chamber

As motivated in section 3.9 the cylinder of the WFC and the bushing are formed by the same part. This bushing part requires a high manufacturing precision to ensure its guiding function. This process dictates, that the bushing can not be a blind hole, therefore a lid is added on the bottom to enclose the pressure chamber. Therefore, this connection needs to be sealed.
This is a simple resting seal. A standard sealing with a rubber O-ring requires squeezing and pretensioning. This would result in stress and deformation of the bushing part. This is undesirable since any deformation acts on the tight tolerances of the bushing, resulting in a reduced or failed function.
To seal the gap between these two components a glue sealing was designed. Since the chamber air transmits the weight force from the piston to the lid, theoretically there is no load on this connection apart from the chamber pressure. Thus, it can be designed very simple and compact. In the lid a ring slot is machined, which fits the beveled bottom edge of the bushing. First the slot is filled with the required amount of glue and than the bushing is placed into this sump. This allows an airtight connection of the components with minimal stress and spacial demands. The downsides are the complex mounting process and the fact that the components cannot be separated from each other anymore. Additionally, the strength of the adhesive bond was checked with different calculation methods from [109] and the data from [110].

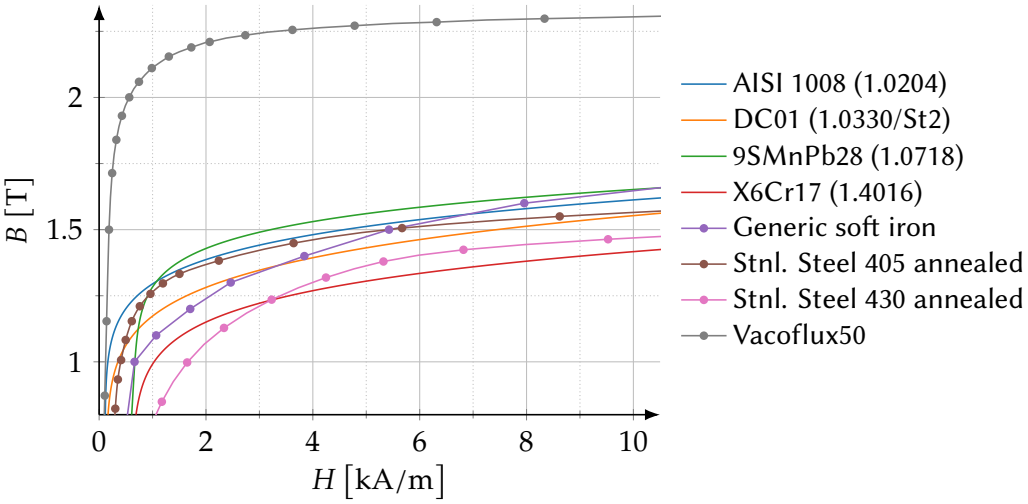

Figure 5.3: Selection of initial magnetization curves of the investigated ferromagnetic materials [111–114]

5.1.2 Passive Magnetic Circuit

In section 4.3 the topology and its geometries were derived. The parameter values were rounded to tenths of a millimeter to simplify manufacturing. In a rerun of the optimization these slight changes in the parameters resulted in only a very minor decrease in the F2P, since the converged optimum is flat.

In the topology ferromagnetic components are included that enclose the coil. This setup complicates the design and mounting procedure. The components from fig. 5.2 that make up the passive magnetic circuit are the two permanent magnets, the iron ring, disk and shell. For the ring, disk and shell a ferromagnetic material with high saturation has to be selected. The hysteresis itself is of minor importance since the parts are only magnetized in one direction by the permanent magnets. The initial magnetization curves of some of the investigated materials from [102, 111–114] are shown in fig. 5.3. The purple line shows the material data for a generic soft iron which was used in section 4.3. The material with the highest flux capacity is Vacoflux50, which saturates above 2 T [114]. The major downsides of this material are that it is cost intensive and problematic to machine with the desired milling and turning processes. Low alloy steels (1.0204, 1.0330, 1.0718) have a high saturation [111] but need to be coated after machining to protect against corrosion. In contrast, a high grade steel (stainless steel 405, stainless steel 430, 1.4016) [112] is appealing since no coating is required. Unfortunately, 1.4016 has a comparably low saturation magnetization, whereas the variants 405 and 430 need to be heat treated (annealed)

after machining to achieve their magnetic properties.
Thus, the standard machining steel 9SMnPb28 (1.0718) is chosen. A chemical nickel coating is applied, since the resulting layer has a uniform thickness. Therefore, the tolerances on the parts are adjusted. With these material properties the optimization was rerun but resulted in no significant geometry changes.

The two permanent magnets are mounted with their north poles onto the middle iron ring. To center these components they are put onto an aluminum shaft. In general the magnetic attraction force provides a strong connection between the ferromagnetic parts and the magnets. But after the first permanent magnet (PM) is put on the ring it will repel the second magnet. The mounting forces have been simulated and result in a peak repelling force of $\approx$39 N at a distance of 3 mm. Interestingly, by further approaching the other components, the repelling force reduces and flips at 0.2 mm to an attracting force with 10 N pull at contact. Subsequently, the iron disk is put onto this stack. When mounting this stack into the shell stronger attraction forces occur and would separate the components. Therefore, the above connections are reinforced by applying adhesive on the contacting surfaces. When the adhesive bond is subjected to pulling forces a standard nickel plating tends to rip off the magnet base material. Instead the magnets are coated with a phosphate coating, which is stronger and creates a better adhesive base.

Prior to enclosing the magnetic circuit, the coil assembly needs to be put in into the shell. Then the previously used shaft-tool is centered in the cone of the shell. The magnet stack is kept from snapping into the shell via a retention nut. Threads in the shaft and nut allow a controlled approaching motion. The stack does not need to be fixed in another way since the simulated attraction force reaches about 280 N. This way the passive magnetic circuit can be disassembled in the reverse order to access the coil assembly.

An O-ring is placed in a groove on top of the shell. This acts as a soft bottom end-stop for the top assembly.

5.1.3 Mechanical Interfaces and Installation of the Subassemblies

After the passive magnetic circuit is assembled the bushing assembly can be installed. The previously mentioned cone in the shell mates with a cone on the bushing. In this way a centric and axially parallel position of assemblies is ensured. A ring screws into the shell, thereby fixing the bushing. The bushing

is situated inside the magnet stack. The thermal expansion coefficient of these components differs significantly. To not introduce disturbing stress on the bushing, a narrow gap is left around it. This results in a big free length of the bushing. To prevent damages on the bushing from handling the LAU a soft support is introduced in the disk via an O-ring.

The pin with the sphere of the lid protrudes the disk so the air bearing can be attached. A precision machined block, which acts as the mating surface for the aerostatic rotational locking, is mounted on the side of the shell. Its location is fixed via a pin on the top end and its guiding direction can be adjusted via a thorough hole on the lower end to the guiding direction of the bushing. An imperfect adjustment results in a helical movement. The measurement scale is located front side of this block.

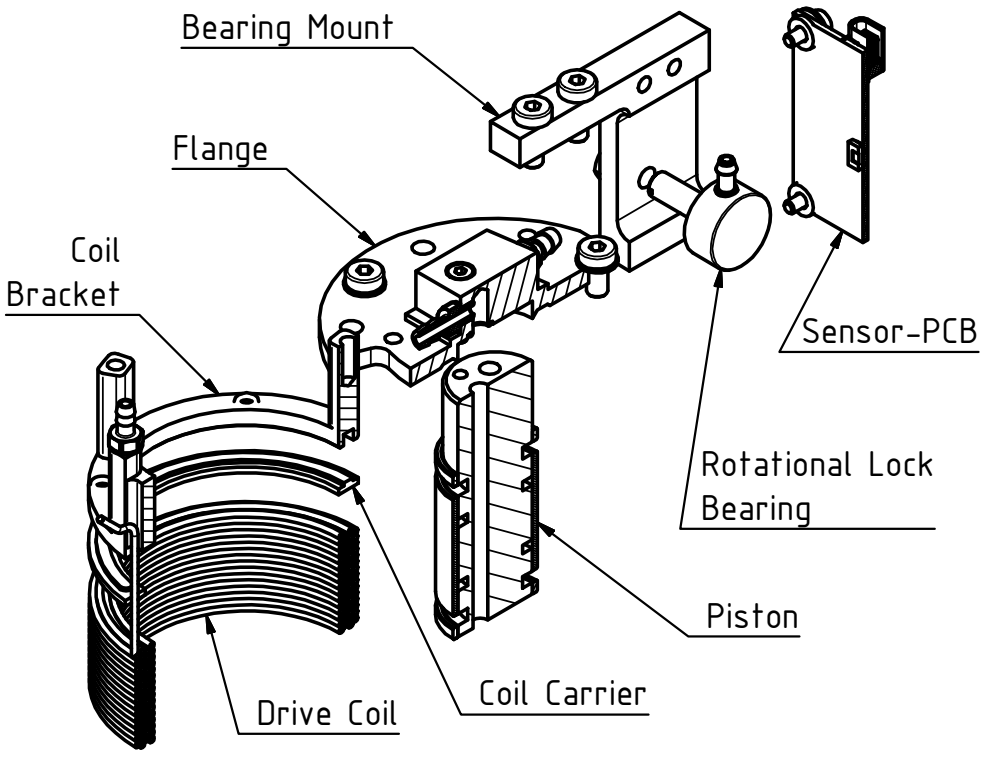

Figure 5.4: Explosional, cross-sectional view of the components of the active top assembly

5.2 Top Assembly

The parts of the LAUs top assembly can be seen in fig. 5.4. It is fixed to the slider and accommodates all active components. Therefore, the necessary hoses and wires are routed from the slider to this top assembly.
The following subsections outline the design decisions made to integrate all components and their interaction with the base assembly.

5.2.1 Piston and Shaft

The central component in this assembly is the piston for the pneumatic WFC. The length of it is chosen to minimize the non-displaceable volume of the chamber, as requested in section 4.2.3. At the bottom end-stop the remaining gap between the piston and the lid is about 0.5 mm. The air to pressurize the chamber is fed via a channel inside the piston into the chamber, thereby realizing the design option from fig. 3.8c.
The piston doubles as the shaft for the aerostatic bushing guiding. The air for this guiding is also supplied via an piston-internal channel to the inside of a sleeve around the piston. This sleeve incorporates throttling features, which are necessary for the aerostatic guiding. Above and below this sleeve grooves are machined into the piston. These grooves are connected via a third channel in the piston to the atmospheric pressure. Thereby, the functional elements, the vertical guiding and the chamber pressure, are decoupled from each other. Additional rings on the piston reduce the open cross-section to the bushing wall, forming the leakage sealing.

The piston is a separate part from the flange. This way the volume of the precision machined part is reduced to the piston and shaft. Further, the machining of the internal channels is simplified. Also, the ports for the channels can be oriented freely on the flange. To not protrude with the hoses into the measurement region of the laser interferometers the ports exit the flange horizontally. The piston is housed in the flange via a tolerated cylindrical recess.

5.2.2 Coil Assembly

The coil assembly contains the drive coil, the coil carrier and the coil bracket. The coil bracket has two functions. First, it protrudes through the shell and couples the coil with the flange via three stems. Second, it incorporates the

cooling channel and includes the input and output port for the coolant. The wires and supply tubing connect to another stem which also passes through the shell. The channel is machined into the bottom of the ring shape and leads once around the coil circumference. It is capped by the coil carrier. The coil is fastened to this carrier with a specialized thermally conductive and mechanically stiff adhesive. The parts are centered during the mounting process via a cylindrical tool.

On top of the coil bracket, O-rings are used as an end stop for the top-most position.

5.2.3 Mechanical Interface Between Piston and Coil Assembly

After the coil assembly is placed in the shell, three stems protrude from openings in the top face of the shell. These stems connect to the flange via screws. A 3D printed gage is used to adjust their relative position. Due to fabrication and mounting tolerances the coil might be in contact to the enclosing components. The enlarged through holes for the stem screws allow an adjustment to achieve a frictionless motion.

5.2.4 Rotational Locking and Vertical Measurement System

On the side of the flange two bearing mounts hold the air bearing pads which lock the rotational freedom. Very small bearings with a diameter of 12 mm are used, since no rotational load is expected. These pads interface the block on the base assembly. Their proximity to it can be adjusted via threads in the bearing mounts. The bearing mount shown in fig. 5.4 acts as a fixed bearing, whereas the other bearing mount is narrowed down to work like a flexure hinge, which can be seen in fig. 5.1. Hence, the associated air bearing acts as a soft preload for the opposing one.
Preloading the fixed bearing with permanent magnets was investigated but cannot be realized without parasitic vertical forces, due to hysteresis or the nonlinear field distribution of permanent magnets.

Already existing position dependent effects may be used to derive the LAUs current vertical position. The flux field of the magnetic circuit is such an effect. A hall probe can be implemented at a place where the fields magnitude change

is large. From the previous FEM simulations it was found that the outside stray flux of the drive is too weak for hall probes to achieve the required positional resolution. Inside the magnetic rings the flux gradient is large enough but the coil introduces additional notable flux components here, thus compromising the measurement. Further, in [115, 116] methods to use the coils of electromagnetic drives are investigated. The coils position is reconstructed via its change in inductance. The required resolution cannot be achieved, hence a measurement system needs to be added.
An overview of the variety of distance measurement methods can be found in [117]. For this application only contact-free, frictionless methods are eligible, which do not influence the surrounding systems and fit the spacial restrictions. Due to these strong limitations only optical systems are feasible. Incremental encoders are a proven and especially compact devices. Further, catalog products can be obtained which communicate directly with the existing control system, thus reducing the overhead for signal processing and power supply dramatically. The downside is that the sensor needs to be aligned properly to the scale, thus requiring adjustment capabilities. Therefore, an encoder [118] with high angular tolerances of up to 2° is used. The sensor has an internal interpolator and puts out analog and digital encoder signals, thus very few additional electrical components are needed on the electronics board. Its circuit board bridges the two bearing mounts and is adjusted via through holes in the corners.

Chapter 6

Conclusion & Thoughts on Future Research

This chapter concludes the most relevant results of this thesis. Further, suggestions and notions for future research fields are given.

6.1 Results of This Work

In *chapter 1* existing nanoprecision devices were presented. Especially the vertical guiding and drive systems were elaborated and their performance considered. Further, the NPPS100 planar drive system was presented in detail, with its setup and major components described and its specifications listed. Following, the source and magnitude of the vertical and tilting errors of the slider in this drive system were described.
The idea of actively compensating these errors and increasing the functionality through additional vertical DOFs of the drive system was presented as the main motivation for the following chapters.

The rigid body model of the NPPS100 and its measurement, guiding and drive subsystem were presented in *chapter 2*. New degrees of freedom need to be introduced into the system to allow the requested compensation motions. It was analyzed what possible methods and locations exist to integrate these new drive and guiding systems. Through a discussion and comparison of the found variants it was discovered that the most promising method is to introduce three identical Lifting and Actuating Units, one at each corner of the slider body.

Chapter 3 addressed the used constructive development process, which was used to develop these units, and described its preliminary steps. Thereby, via its overall function it was found, that the unit has a multitude of inputs which needs to be considered during the design. Further, the output quantities, as well as different kinds of requirements were elaborated. From these results the functional components and their structural interaction was formulated. The drive and the guiding were found to be the major components which enable the motion. A list of feasible actuation effects for the drive component was composed. These effects were compared and evaluated based on application relevant criteria, resulting in the Lorentz-force effect scoring best. Via a pre-investigation it was found that carrying the sliders mass solely with a Lorentz-force drive exceeds limitations on introduced heat.
Based on the studies in chapter 1 the approach of adding an actuator with no local heat emission was pursued. Practical actuation effects for this task were composed and evaluated with the result that a pneumatic weight force compensation is applied. Further, seal methods for the pneumatic chamber were reviewed.
The possible guiding methods were investigated under the scope of precision positioning. The aerostatic method was found to be most suitable for this spatially limited precision application. Further, topological implementation variants were examined.
These results are concluded in the setup of the technical principle of the Lifting and Actuating Unit. It presents that the four major components (weight force compensation, Lorentz-force drive, aerostatic guiding and internal measurement system) are all arranged in parallel. Based on these findings the design space, the overall shape and the arrangement of the components in it was discussed. It resulted in the concentric arrangement of the components and the dimensional integration of the pneumatic weight force compensation and the aerostatic guiding.
In conclusion an appropriate development process for a lifting module has been layed out and presented. Since the lifting task is a common challenge in the field of engineering, this process could be reused to develop similar units adapted to future requirements.

Chapter 4 focused on the derivation of the central functional dimensions and obtained a deeper understanding of the system behavior. First the different loads on one unit were clarified and their quantity recorded.
Following, the components of the pneumatic weight force compensation are abstracted and their major mathematical representations derived and compiled. The links between the chamber geometry dimensions and the equilibrium pres-

sure, acceleration potential, as well as chamber stiffness and eigenfrequency were pointed out. Through these investigations it was determined, that the non-displaceable volume should be minimized to reach a higher natural frequency and stiffness. Afterwards, the models for the piston sealing, the pneumatic transmission line, as well as the pneumatic valve were introduced and composed into one model. From this, the state space representation and transfer function were derived, which gave insight on the achievable dynamic performance. Making precise statements about the behavior of the future device is difficult since a lot of parameters influence the state variables. From the valve equation it was found that an intermediate equilibrium pressure is favorable because the mass flow will be the same in the loading and unloading process of the chamber. Via this request the chamber diameter was set.
With the inner chamber dimensions the surrounding electromagnetic drive could be designed. Commencing, the primary design goal for this actuator was defined: The heat dissipated during operation should be minimal; therefore the output force was set in relation to the input power. This ratio was further elaborated and served as objective function for the upcoming optimization. With analytic equations for the magnetic field of permanent magnets, the geometries of various iron-free drive topologies were optimized. Further topologies with ferromagnetic components were drafted and implemented into a finite element system. From their optimization the best suitable drive geometry was found. With the given coil dimensions a parameter study on all available wire diameters was conducted and their influence on a multitude of coil and drive parameters evaluated. Finally, the thermal behavior of this topology and the performance of an added cooling system were assessed.
Following, the load on the aerostatic guiding was estimated. The simulational results from another work [107] showed that the projected size of the guiding elements provides large reserves over the assumed load case.

Subsequently, *chapter 5* presented the design of the mechanical parts and the functional assemblies. Thereby, the base assembly includes all the passive components. By the rotational symmetric design the number of mounting elements could be reduced and the alignment was simplified. The parts were designed in a way, that disturbing loads on the bushing part are minimized. The material options for the ferromagnetic parts were analyzed. Further, a special focus was set on the mounting of the permanent magnets with the ferromagnetic parts, as these components are subjected to large push and pull forces.
The top assembly is composed of mostly the active components. First the integration of the piston and the shaft is described. Thereafter, the assembly of the coil and the cooling channel is explained and their adjustable interface to the

other components clarified. Finally the arrangement and adjusting features of the rotational locking system are reviewed and the selection of the measurement system was examined.
It was shown that multiple functional elements can be integrated into a device with such strong spatial constraints. This was enabled by reducing the design to very few parts, which reduced the mechanical complexity and the otherwise required adjustment elements. Further, it was demonstrated that even simple geometries allow the design of a high performance actuator.

6.2 Future Work

Unfortunately, due to extended manufacturing time of some components the Lifting and Actuating Unit could not be set up in the scope of this thesis. Thus, the primary task in the future is, to mount and setup the unit and conduct first tests to check its functionality. The predicted performance parameters of the electromagnetic drive (maximum force, electrical resistance, inductance, force-to-power ratio, current sensitivity) and the pneumatic piston (maximum force, pressure dynamics, stiffness, natural frequency) will be validated.

When all parameters have been validated, the system behavior shall be analyzed. Based on the findings in sections 4.2.7 and 4.3.5 a first controller can be implemented and tested on a testbed. Due to the overactuated nature of the device many advanced control methods are available. Thus, the mode of operation could be adjustable depending on the dynamic and precision requirements as well as thermal constraints. A strong focus should be set on investigating the pneumatic valve with its controller and their effect on the achievable precision and dynamics.

6.2.1 Integration of the Lifting and Actuating Unit Into a Nanopositioning and Nanomeasuring Device

As soon as the results of the single controlled unit are satisfactory three of these can be implemented into the NPPS100 drive system. A new overall control scheme has to be set up since the slider now is actuateable in all six degrees of freedom. The crosstalk between the planar and vertical drive system has to be evaluated and the existing coupling needs to be implemented into the control algorithm.

With such an advanced control system the stator-related flatness errors, which motivated the development, can be compensated. Furthermore, possible other disturbing effects, such as static and dynamic deflection of the slider and imperfections of the bottom mirror, could be neutralized.

6.2.2 Nanofabrication

With such a precisely moving device fabrication processes–such as Two-Photon-Polymerization [119], Field Emission Scanning Probe Lithography [120], Nanoimprint Lithography [121] and Direct Laser Writing [122]–can be performed on large objects. Possibly multiple processes can be combined [123, 124] to structure large surfaces with nanometer scale features, allowing components with new functions and properties. The expected processing loads are very small and can be counteracted easily.

6.2.3 Remarks on a Possible Redesign

If in the future the limiting loads or travel ranges of the upgraded NPPS100 should be exhausted, a new, more capable device will be needed. Thereby, the proposed design process can be reused with adapted boundary conditions.

Throughout the design of this Lifting and Actuating Unit many design ideas were composed. Some of which could be combined, whereas some exclude each other.
If the low natural frequency of the pneumatic weight force compensation element needs to be increased a mechanical spring could be implemented in parallel, possibly inside the chamber. This could also be retrofitted to the existing system, which would increase the load capacity.
A contactfree method to increase the stiffness and dynamics of the piston would be to implement a double acting piston (shown in fig. 3.8d). As this piston is situated between the two pressure chambers increases the complexity and difficulty of sealing and guiding it.
Possibly a ferrofluidic sealing could be implemented, thus the piston would need to conduct some electromagnetic flux. New electromagnetic drive topologies need to be found which can benefit from this kind of setup. Another aspect is, to use such fluids to increase the magnetic flux in the air gap, thus improving the performance of the electromagnetic drive. Possibly a damping will be introduced, which needs to be investigated. Further, these ideas could be combined,

making the bottom surface of the coil act as the piston surface. The coil would need to be airtight and sealed to the surrounding passive magnetic components. Thus, the electromagnetic drive would be strongly integrated with the pressure chambers, possibly allowing miniaturization.
Another option to improve the pneumatic dynamics would be to have the proportional valve on board of the slider, directly connected to the chamber. This could minimize the pressure delay in the chamber. Further, the number of pneumatic lines onto the slider is reduced (which is especially attractive for double acting setups, as they require more tubes) but additional wires would be necessary. Also the power output of the valves needs to be considered. Thus, low power, high dynamic valves would be needed (e.g. piezo-driven).
The measurement system could also be integrated into the electromagnetic drive. E.g. a coil with multiple tabs could be set up as a linear variable differential transformer, which has a position dependent inductance. That would lead to challenges in the signal processing during operation of the drive, as well as the manufacturing of such a coil.

Bibliography

[1] M. Kühnel, T. Fröhlich, R. Füßl, M. Hoffmann, E. Manske, I. Rangelow, J. Reger, C. Schäffel, S. Sinzinger, and J.-P. Zöllner. "Towards alternative 3D nanofabrication in macroscopic working volumes". In: *Measurement Science and Technology* 29.11 (2018), p. 114002.

[2] E. Manske, G. Jäger, T. Hausotte, and R. Füßl. "Recent developments and challenges of nanopositioning and nanomeasuring technology". In: *Measurement Science and Technology* 23.7 (2012), 10pp.

[3] *Evaluation of measurement data – Guide to the expression of uncertainty in measurement*. JCGM Guide 100:2008. Also published as ISO/IEC Guide 98-3:2008. Joint Committee for Guides in Metrology, 2008. URL: https://www.bipm.org/en/publications/guides/gum.html.

[4] E. K. Abbe. "Messapparate für Physiker". In: *Zeitschrift für Instrumentenkunde* 10 (1890), pp. 446–447. URL: https://archive.org/details/zeitschriftfrin00dorngoog/page/n456.

[5] G. Jäger, E. Manske, T. Hausotte, H.-J. Büchner, and R. Grünwald. "A novel approach to positioning- and measuring technique for nanometrology". In: *International Conference Sensors and Systems*. Vol. 24. 2002-06-24, p. 27.

[6] R. Leach. *Fundamental Principles of Engineering Nanometrology*. 2nd ed. Elsevier, 2014.

[7] T. Hausotte. "Nanopositionier- und Nanomessmaschine". PhD thesis. Technische Universität Ilmenau, 2002-03.

[8] T. Hausotte. "Nanopositionier- und Nanomessmaschinen – Geräte für hochpräzise makro- bis nanoskalige Oberflächen- und Koordinatenmessungen". Habilitation. Technische Universität Ilmenau, 2011-03.

[9] J. K. van Seggelen. "NanoCMM: A 3D Coordinate Measuring Machine with low moving mass for measuring small products in array with nanometer uncertainty". eng. PhD thesis. Technische Universiteit Eindhoven, 2007-02-15. DOI: 10.6100/IR616667.

[10] R. Henselmans. "Non-contact Measurement Machine for Freeform Optics". PhD thesis. Technische Universiteit Eindhoven, 2009-04-02.

[11] TNO Technical Sciences Instrument Manufacturing Optical Components. *Nanomefos Freeform Measuring*. 2012. URL: https://www.tno.nl/media/2662/nanomefos-leaflet.pdf (visited on 2020-03-07).

[12] H. A. M. Spaan, R. L. Donker, and I. Widdershoven. "ISARA 400: Enabling ultra-precision coordinate metrology for large parts". In: 50 (2010-01), pp. 231–234.

[13] H. A. M. Spaan, R. L. Donker, and I. Widdershoven. "Isara 400: development of an ultraprecision CMM for 3D measurement of large parts". In: *Proc. ASPE spring meeting*. 2009.

[14] R. Donker, I. Widdershoven, D. Brouns, and H. A. M. Spaan. "Realization of ISARA 400: A Large Measurement Volume Ultra-Precision CMM". In: *Proc. of the 24th Annual Meeting of The American Society for Precision Engineering ASPE* (2009).

[15] IBS Precision Engineering bV. *ISARA 400 Datasheet*. URL: www.ibspe.com/public/uploads/content/files/Isara400_Webversion.pdf (visited on 2019-12-31).

[16] A. J. M. Moers and M. C. van Riel Edwin J.C. Bos. "Design and verification of the TriNano ultra precision CMM". In: *International Scientific Colloquium* 56 (2011-09-12). URL: https://nbn-resolving.org/urn:nbn:de:gbv:ilm1-2011iwk-092:8.

[17] E. Bos, T. Moers, and M. van Riel. "Design and verification of an ultra-precision 3D-coordinate measuring machine with parallel drives". In: *Measurement Science and Technology* 26.8 (2015-07), p. 085904. DOI: 10.1088/0957-0233/26/8/085904.

[18] F. Balzer. "Entwicklung und Untersuchungen zur 3-D-Nanopositioniertechnik in großen Bewegungsbereichen". PhD thesis. Technische Universität Ilmenau, 2013.

[19] E. Manske, G. Jäger, T. Hausotte, A. Müller, and F. Balzer. "Nanopositioning and nanomeasuring machine NPMM-200 — sub-nanometer resolution and highest accuracy in extended macroscopic working areas". In: *Proc. of the 17th Int. Conf. of the European Society for Precision Engineering and Nanotechnology* 17 (2017), 81pp.

[20] C. Schäffel, M. Katzschmann, H.-U. Mohr, R. Glöss, C. Rudolf, C. Mock, and C. Walenda. "6D planar magnetic levitation system - PIMag 6D". In: *Bulletin of the JSME Mechanical Engineering Journal* 3 (2015). DOI: 10.1299/mej.15-00111.

[21] M. Torralba, M. Valenzuela, J. Yagüe-Fabra, J. Albajez, and J. Aguilar. "Large range nanopositioning stage design: A three-layer and two-stage platform". In: *Measurement* 89 (2016-07), pp. 55–71. DOI: 10.1016/j.measurement.2016.03.075.

[22] A. Bos, R. Henselmans, P. C. J. N. Rosielle, M. Steinbuch, and M. J. A. te Voert. "Design of an E-ELT M1 segment measurement machine with nanometer accuracy". In: *Advances in Optical and Mechanical Technologies for Telescopes and Instrumentation*. Ed. by R. Navarro, C. R. Cunningham, and A. A. Barto. SPIE, 2014-07. DOI: 10.1117/12.2055143.

[23] I. Widdershoven, R. L. Donker, and H. A. M. Spaan. "Realization and calibration of the "Isara 400"ultra-precision CMM". In: *Journal of Physics: Conference Series* 311 (2011-08), p. 012002. DOI: 10.1088/1742-6596/311/1/012002.

[24] G. Jäger, T. Hausotte, E. Manske, H.-J. Büchner, R. Mastylo, N. Dorozhovets, and N. Hofmann. "Nanomeasuring and nanopositioning engineering". In: *Measurement* 43.9 (2010), pp. 1099–1105. DOI: 10.1016/j.measurement.2010.04.008.

[25] Eitzenberger Luftlagertechnik GmbH. *Z-Hubmodul*. 2019. URL: https://www.eitzenberger.com/de/produkte/linearachsen-kreuztische/z-hubmodul.html (visited on 2020-03-07).

[26] S. Gorges, B. Leistritz, S. Hesse, I. Ortlepp, G. Slotta, and C. Schäffel. "Development of an integrated guiding and actuation element for high dynamic nanopositioning systems". In: *Proceedings of the 59th Ilmenau Scientific Colloquium*. 2017. URL: https://nbn-resolving.org/urn:nbn:de:gbv:ilm1-2017iwk-077:4.

[27] H. Eitzenberger and J. Harnisch. "Positioning device, x-y table, and lifting unit". WO2014090291A1. 2014-06. URL: https://worldwide.espacenet.com/publicationDetails/biblio?CC=WO&NR=2014090291A1&KC=A1&FT=D#.

[28] S. Hesse, C. Schäffel, H.-U. Mohr, M. Katzschmann, and H.-J. Büchner. "Design and performance evaluation of an interferometric controlled planar nanopositioning system". In: *Meas. Sci. Technol.* 23 (2012).

[29] C. Schäffel. "Untersuchungen zur Gestaltung integrierter Mehrkoordinatenantriebe". PhD thesis. Technische Universität Ilmenau, 1996-06.

[30] S. Hesse, C. Schäffel, M. Katzschmann, T. Maass, and H.-U. Mohr. "Planar motor concept for positioning with nanometer positioning uncertainty". In: *Proc. of the 8th Int. Conf. of the European Society for Precision Engineering and Nanotechnology* 1 (2008), pp. 150–154.

[31] SCHOTT AG. *ZERODUR® Extremely Low Expansion Glass Ceramic*. Ed. by SCHOTT North America Inc. 2019. URL: https://www.us.schott.com/advanced_optics/english/products/optical-materials/zerodur-extremely-low-expansion-glass-ceramic/zerodur/index.html (visited on 2019-12-13).

[32] New Way Air Bearings, Inc. *S205001 – 50mm VPL Air Bearing*. URL: https://www.newwayairbearings.com/catalog/product/50mm-vpl-air-bearings/ (visited on 2020-01-04).

[33] *Laserinterferometer*. 2019. URL: https://sios.de/produkte/laengenmessysteme/laserinterferometer/ (visited on 2019-12-10).

[34] S. Gorges, S. Hesse, C. Schäffel, I. Ortlepp, E. Manske, E. Langlotz, and D. Dontsov. *Integrated Planar 6-DOF Nanopositioning System*. 2019-09-04. DOI: 10.1016/j.ifacol.2019.11.693.

[35] O. Dannberg, I. Ortlepp, and E. Manske. "FPGA-based signal processing of a heterodyne interferometer". In: *Proceedings of the 59th Ilmenau Scientific Colloquium*. Vol. 59. 1.1.P2. 2017-09-11. URL: https://nbn-resolving.org/urn:nbn:de:gbv:ilm1-2017iwk-117:6.

[36] L.-W. Tsai. *Robot Analysis: The Mechanics of Serial and Parallel Manipulators*. Wiley-Interscience, 1999.

[37] K. Roth. *Konstruieren mit Konstruktionskatalogen*. 3rd ed. Vol. 1. Springer, 2000. DOI: 10.1007/978-3-642-17466-7.

[38] P. Naefe. *Einfuhrung in das Methodische Konstruieren. Für Studium und Praxis*. 2nd ed. Springer Vieweg Verlag, 2012. DOI: 10.1007/978-3-658-00002-8.

[39] W. Krause. *Konstruktionselemente der Feinmechanik*. 4th ed. München: Hanser, 2018. ISBN: 978-3-446-44796-7.

[40] *Entwicklung technischer Produkte und Systeme - Modell der Produktentwicklung*. VDI guideline 2221:1. Verein Deutscher Ingenieure, 2019. URL: https://www.vdi.de/richtlinien/details/vdi-2221-blatt-1-entwicklung-technischer-produkte-und-systeme-modell-der-produktentwicklung.

[41] *Entwicklungsmethodik für mechatronische Systeme*. VDI guideline 2206. Verein Deutscher Ingenieure, 2004-06. URL: https://www.vdi.de/richtlinien/details/vdi-2206-entwicklungsmethodik-fuer-mechatronische-systeme.

[42] *Konstruktionsmethodik - Methodisches Entwickeln von Lösungsprinzipien*. VDI guideline 2222:1. Verein Deutscher Ingenieure, 1997. URL: https://www.vdi.de/richtlinien/details/vdi-2222-blatt-1-konstruktionsmethodik-methodisches-entwickeln-von-loesungsprinzipien.

[43] W. Krause, A. Holfeld, J. Thümmler, and G. Röhrs. *Grundlagen der Konstruktion für Feinwerk- und Elektrotechniker*. 3rd ed. Springer Verlag, 1984.

[44] E. Kallenbach, T. Ströhla, O. Birli, K. Feindt, and M. Kallenbach. "Configuration in the Mechatronic Design Process - Represented by Fast Acting Magnetic Actuators". In: 2000-09-19, pp. 313–322.

[45] T. Erbe. "Beitrag zur systematischen Aktor- und Aktorprinzipauswahl im Entwicklungsprozess". PhD thesis. Technische Universität Ilmenau, 2013.

[46] G. Bönsch and E. Potulski. "Measurement of the refractive index of air and comparison with modified Edlén's formulae". In: *Metrologia* 35.2 (1998-04), pp. 133–139. DOI: 10.1088/0026-1394/35/2/8.

[47] National Aeronautics and Space Administration, National Oceanic and Atmospheric Administration, and United States Air Force. *U.S. Standard Atmosphere*. Report. Washington, D.C.: U.S. Government Printing Office, 1976-10. URL: https://ntrs.nasa.gov/archive/nasa/casi.ntrs.nasa.gov/19770009539_1977009539.pdf.

[48] P. Tipler and G. Mosca. *Physik für Wissenschaftler und Ingenieure*. Ed. by J. Wagner. 7th ed. Springer Spektrum, 2015. DOI: 10.1007/978-3-642-54166-7.

[49] Deutscher Wetterdienst. *Wetterrekorde*. URL: https://www.dwd.de/SharedDocs/broschueren/DE/presse/wetterrekorde.pdf (visited on 2020-01-28).

[50] B. Leistritz. "Luftlagerelement für ein Präzisionspositioniersystem im Grobvakuum". Diploma Thesis. Technische Universität Ilmenau, 2007.

[51] JPE - Janssen Precision Engineering. *Precision Point: Vacuum - Rules of Thumb*. 2016. URL: https://www.janssenprecisionengineering.com/page/precision-point/vacuum-rules-thumb/ (visited on 2020-02-29).

[52] H. Janocha. *Actuators. Basics and Applications*. Springer, 2004.

[53] R. Munroe. *What if? Serious Scientific Answers to Absurd Hypothetical Questions*. Houghton Mifflin Harcourt, 2014-09-02. URL: https://whatif.xkcd.com/book/.

[54] D. Shu, Y. Han, T. Toellner, and E. Alp. "Linear actuator system with 1-angstrom closed-loop control resolution and 50-mm travel range". In: *Proceedings of SPIE - The International Society for Optical Engineering* 4771 (2002-09). DOI: 10.1117/12.482148.

[55] PI Ceramic GmbH. *Electric Operation of Piezo Actuators*. URL: https://www.piceramic.com/en/piezo-technology/properties-piezo-actuators/electrical-operation/ (visited on 2020-01-13).

[56] T. Raparelli, L. Mazza, and A. Trivella. "Study of a non-conventional sealing system for low-friction pneumatic cylinders". In: vol. 76. 2012-09, pp. 55–64. ISBN: 9781845646103. DOI: 10.2495/TD120051.

[57] W. Haas. *Grundlehrgang Dichtungstechnik*. Lecture script. Institut für Machinenelemente Universität Stuttgart, 2009-07. URL: https://www.ima.uni-stuttgart.de/dokumente/forschung/dichtungstechnik/skript_dichtungstechnik.pdf (visited on 2020-01-28).

[58] BEI KIMCO Magnetics Division. *Cylindrical Frameless Linear Voice Coil Actuator LA28-22-001A*. Specification Drawing. 2020-02-14. URL: https://www.sensata.com/sites/default/files/media/documents/2018-06-25/ourproducts_voice-coil-actuator-linear-frameless-la28-22-001a_PDF_Drawing.pdf (visited on 2020-02-14).

[59] T. Hackel. "Grundlegende Untersuchungen zu vertikalen Positioniersystemen für Nanopräzisionsmaschinen". PhD thesis. Technische Universität Ilmenau, 2010-06.

[60] J. L. Janssen. "Extended analytical charge modeling for permanent-magnet based devices : practical application to the interactions in a vibration isolation system". English. PhD thesis. Technische Universiteit Eindhoven, 2011-12-13. DOI: 10.6100/IR719555.

[61] LinMot GmbH. *Anwendungsbereich MagSpring*. Technical application brochure. 2019-08-21. URL: https://linmot.com/wp-content/uploads/2019/08/Anwendungsbericht-MagSpring_DE.pdf (visited on 2020-01-15).

[62] H. K. Müller and B. S. Nau. *Fachwissen Dichtungstechnik: Magnetflüssigkeits-Dichtungen*. URL: http://www.fachwissen-dichtungstechnik.de/PDFs_01_2020_mit_PW/fw-dt_Kapitel20_01_20.pdf (visited on 2020-02-23).

[63] H. K. Müller and B. S. Nau. *Fachwissen Dichtungstechnik: Drosseldichtungen für Gase*. URL: http://www.fachwissen-dichtungstechnik.de/PDFs_01_2020_mit_PW/fw-dt_Kapitel17_01_20.pdf (visited on 2020-01-28).

[64] S. Zschäck, S. Hesse, A. Amthor, M. Katzschmann, C. Schäffel, and C. Ament. "Vergleich der Scan-Performance bei Nanopositioniersystemen mit großem Bewegungsbereich". In: *Technisches Messen* 81 (6 2014-06-28), pp. 335–342. DOI: 10.1515/teme-2014-0358.

[65] S. Linß, P. Schorr, and L. Zentner. "General design equations for the rotational stiffness, maximal angular deflection and rotational precision of various notch flexure hinges". In: *Mechanical Sciences* 8.1 (2017-03-15), pp. 29–49. DOI: 10.5194/ms-8-29-2017.

[66] S. Linß, S. Henning, and L. Zentner. "Modeling and Design of Flexure Hinge-Based Compliant Mechanisms". In: *Kinematics*. Ed. by J. Mizrahi. Rijeka: IntechOpen, 2019-04. Chap. 3. DOI: 10.5772/intechopen.85224.

[67] R. Ravaud, G. Lemarquand, and V. Lemarquand. "Force and Stiffness of Passive Magnetic Bearings Using Permanent Magnets. Part 1: Axial Magnetization". In: *IEEE Transactions on Magnetics* 45 (7 2009), pp. 2996–3002. ISSN: 0018-9464,1941-0069. DOI: 10.1109/tmag.2009.2016088.

[68] F. Dohnal and R. Markert. "Enhancement of External Damping of a Flexible Rotor in Active Magnetic Bearings by Time-Periodic Stiffness Variation". In: *Journal of System Design and Dynamics* 5 (5 2011), pp. 856–865. ISSN: 1881-3046. DOI: 10.1299/jsdd.5.856.

[69] W. B. Rowe. *Hydrostatic, aerostatic, and hybrid bearing design*. Elsevier, 2012. DOI: 10.1016/B978-0-12-396994-1.00001-2.

[70] New Way Air Bearings, Inc. *NEWWAY End-supported Air Slides*. URL: https://www.newwayairbearings.com/catalog/end-supported-air-slides/ (visited on 2020-02-25).

[71] TECNOTION GmbH. *Eisenkern und Eisenlose Linearmotoren*. Product catalog. 2019-07-31. URL: https://www.tecnotion.de/downloads/katalog-iron-core-/-ironless-motors.pdf (visited on 2020-01-15).

[72] P. Beater. *Pneumatic Drives. System Design, Modelling and Control*. Springer, 2007.

[73] A. Ilchmann, O. Sawodny, and S. Trenn. "Pneumatic cylinders: modelling and feedback force-control". In: *International Journal of Control* 79.6 (2006), pp. 650–661. DOI: 10.1080/00207170600645875.

[74] E. Richer and Y. Hurmuzlu. "A High Performance Pneumatic Force Actuator System: Part I—Nonlinear Mathematical Model". In: *Journal of Dynamic Systems, Measurement, and Control* 122.3 (1999-06), pp. 416–425. DOI: 10.1115/1.1286336.

[75] E. Richer and Y. Hurmuzlu. "A High Performance Pneumatic Force Actuator System: Part II—Nonlinear Controller Design". In: *Journal of Dynamic Systems, Measurement, and Control* 122.3 (1999-06), pp. 426–434. ISSN: 0022-0434. DOI: 10.1115/1.1286366.

[76] S. Gorges and S. Hesse. "Design and Modeling Approach for a Lifting and Actuating Unit for the Application in Nano-Precision Machines". In: *Proceedings of the 33rd Annual Meeting of the American Society for Precision Engineering (ASPE)*. 2018-11-04.

[77] G. Merziger, G. Mühlbach, D. Wille, and T. Wirth. *Formeln + Hilfen zur höheren Mathematik*. 4th ed. Binomi Verlag, 2004.

[78] H. K. Müller and B. S. Nau. *Fachwissen Dichtungstechnik: Fluidströmungen im engen Dichtspalt*. URL: http://www.fachwissen-dichtungstechnik.de/PDFs_01_2020_mit_PW/fw-dt_Kapitel04_01_20.pdf (visited on 2020-01-28).

[79] Verein Deutscher Ingenieure. *VDI-Wärmeatlas*. 11th ed. Vieweg+Teubner Verlag, 2013. DOI: 10.1007/978-3-642-19981-3.

[80] *Pneumatic fluid power — Determination of flow-rate characteristics of components using compressible fluids — Part 3: Method for calculating steady-state flow-rate characteristics of systems*. International standard 6358-3:2014. International Organization for Standardization, 2014. URL: https://www.iso.org/standard/56616.html.

[81] J. Lunze. *Regelungstechnik 1: Systemtheoretische Grundlagen, Analyse und Entwurf einschleifiger Regelungen*. 11th ed. Springer Berlin Heidelberg, 2016.

[82] C. Ament. *Regelungstechnik 2*. Lecture script. Fakultät für Angewandte Informatik Universität Augsburg, 2017-06. URL: https://www.informatik.uni-augsburg.de/lehrstuehle/rt/lehre/Skript/Skript-Regelungstechnik-2---08.pdf (visited on 2020-02-03).

[83] Y. Kawakami, J. Akao, S. Kawai, and T. Machiyama. "Some considerations on the dynamic characteristics of pneumatic cylinders". In: *Journal of Fluid Control* 19.2 (1988-09), pp. 22–36.

[84] T. Mizuno, M. Kawai, F. Tsuchiya, M. Kosugi, and H. Yamada. "An examination for increasing the motor constant of a cylindrical moving magnet-type linear actuator". In: *IEEE Transactions on Magnetics* 41.10 (2005-10), pp. 3976–3978. DOI: 10.1109/TMAG.2005.855160.

[85] B. P. Ruddy. "High force density linear permanent magnet motors:"electromagnetic muscle actuators"". PhD thesis. Massachusetts Institute of Technology, 2012.

[86] E. Kallenbach, R. Eick, T. Ströhla, K. Feindt, and M. Kallenbach. *Elektromagnete. Grundlagen, Berechnung, Entwurf und Anwendung*. Ed. by O. Radler. 5th ed. Springer Fachmedien Wiesbaden, 2018. DOI: 10.1007/978-3-658-14788-4.

[87] P. R. Eckert and E. C. Goltz. "Influence of segmentation of ring-shaped NdFeB magnets with parallel magnetization on cylindrical actuators". In: *Sensors* 14.7 (2014), pp. 13070–13087.

[88] S. Babic and C. Akyel. "Improvement in the analytical calculation of the magnetic field produced by permanent magnet rings". In: *Progress In Electromagnetics Research C* 5 (2008-09), pp. 71–82.

[89] H. C. Roters. *Electromagnetic Devices*. John Wiley and Sons, Inc, 1941.

[90] TDK Corporation. *Magnetic Circuit Design*. Tech. rep. 2012. URL: https://product.tdk.com/en/products/magnet/pdf/e371_circuit.pdf (visited on 2020-02-28).

[91] R. Schinzinger and P. A. Laura. *Conformal Mapping: Methods and Applications*. Dover Books on Mathematics. Dover Publications, 2003.

[92] E. Ilhan, E. T. Motoasca, J. J. Paulides, and E. A. Lomonova. "Conformal mapping: Schwarz-Christoffel method for flux-switching PM machines". In: *Mathematical Sciences* 6 (2012-07). DOI: 10.1186/2251-7456-6-37.

[93] B. Merit, G. Lemarquand, and V. Lemarquand. "Performances and Design of Ironless Loudspeaker Motor Structures". In: *Journal of Applied Acoustics* 71.6 (2010-01), pp. 546–555. DOI: 10.1016/j.apacoust.2009.12.004.

[94] T. Wang, Z. Jiao, L. Yan, C. Chen, and I. Chen. "Design and analysis of an improved Halbach tubular linear motor with non-ferromagnetic mover tube for direct-driven EHA". In: *Proceedings of 2014 IEEE Chinese Guidance, Navigation and Control Conference*. 2014-08, pp. 797–802. DOI: 10.1109/CGNCC.2014.7007311.

[95] Seok-Myeong Jang, Jang-Young Choi, Han-Wook Cho, and Sung-Ho Lee. "Thrust analysis and measurements of tubular linear actuator with cylindrical halbach array". In: *IEEE Transactions on Magnetics* 41.5 (2005-05), pp. 2028–2031. DOI: 10.1109/TMAG.2005.846266.

[96] D. Benyoucef, T. Rachid, M. Helaimi, and B. Belmadani. "Analytical Calculation of Magnetic Field Created by a Ring Magnet Used in Magnetron RF Reactor". In: 2014-12. DOI: 10.13140/RG.2.1.5181.7203/1.

[97] F. W. J. Olver, D. W. Lozier, R. F. Boisvert, and C. W. Clark. *NIST handbook of mathematical functions*. Ed. by National Institute of Standards and Technology (U.S.) Cambridge University Press, 2010.

[98] National Institute of Standards and Technology (U.S.) *Digital Library of Mathematical Functions*. 2019-12-15. URL: https://dlmf.nist.gov/19.8 (visited on 2020-02-17).

[99] D. Kraft. *A Software Package for Sequantial Quadratic Programming*. Research rep. Deutsche Forschungs- und Versuchsanstalt für Luft- und Raumfahrt, 1988.

[100] J. Nocedal and S. Wright. *Numerical Optimization*. 2nd ed. Springer Series in Operations Research and Financial Engineering. Springer New York, 2006.

[101] The SciPy community. *SciPy Reference Guide*. 2019-12-19. URL: https://docs.scipy.org/doc/scipy/reference/generated/scipy.optimize.minimize.html (visited on 2020-02-17).

[102] K. Weise. "Advanced Modeling in Lorentz Force Eddy Current Testing". PhD thesis. Technische Universität Ilmenau, 2016-03-23. URL: https://nbn-resolving.org/urn:nbn:de:gbv:ilm1-2016000122.

[103] Heermann GmbH. *Kupferlackdrähte - Allgemeine Anforderungen nach DIN EN IEC 60317-0-1*. 2020. URL: https://www.heermann-gmbh.de/sites/default/files/tabellen/Kupferlackdraehte-Allgemeine-Anforderungen-nach-DIN-EN-IEC-60317-0-1.pdf (visited on 2020-02-19).

[104] L. Siesing, A. Reinap, and M. Andersson. "Thermal properties on high fill factor electrical windings: Infiltrated vs non infiltrated". In: *International Conference on Electrical Machines (ICEM)*. 2014-09, pp. 2218–2223. DOI: 10.1109/ICELMACH.2014.6960492.

[105] L. Idoughi, X. Mininger, F. Bouillault, L. Bernard, and E. Hoang. "Thermal Model With Winding Homogenization and FIT Discretization for Stator Slot". In: *IEEE Transactions on Magnetics* 47.12 (2011-01), pp. 4822–4826. ISSN: 1941-0069. DOI: 10.1109/TMAG.2011.2159013.

[106] BR Technik Kontor GmbH. *Eigenschaften und Kennzahlen von NdFeB-Magneten*. URL: https://www.magnetkontor.de/content/de/ueber-NdFeB-Magnete.html (visited on 2020-03-02).

[107] P. Frentzel. "Untersuchungen und Auslegung einer aerostatischen Buchsenführung für Präzisionsantriebe". Bachelor thesis. Technische Universität Ilmenau, 2019-06-05.

[108] N. Heidler. "Untersuchungen zylindrischer Gasführungselemente für Hochvakuumanwendungen". PhD thesis. Technische Universität Ilmenau, 2015-05-07.

[109] G. Habenicht. *Kleben: Grundlagen, Technologien, Anwendungen*. 6th ed. Springer Berlin Heidelberg, 2009. DOI: 10.1007/978-3-540-85266-7.

[110] Henkel AG & Co.KGaA. *LOCTITE EA 3421*. technical data sheet. 2014-10. URL: https://www.henkel-adhesives.com/de/de/produkt/structural-adhesives/loctite_ea_3421_ab.html (visited on 2020-02-26).

[111] Modelica Association. *Modelica Standard Library Documentation*. Comp. software. 2019-09-25. URL: https://doc.modelica.org/Modelica%203.2.3/Resources/helpOM/Modelica.Magnetic.FluxTubes.Material.SoftMagnetic.html (visited on 2020-02-27).

[112] COMSOL Inc. *Comsol Multiphysics 5.3 Material Database*. Comp. software. 2017-04-25.

[113] Informationsstelle Edelstahl Rostfrei. *Magnetische Eigenschaften nichtrostender Stähle*. Merkblatt 827. 2013. URL: https://www.edelstahl-rostfrei.de/fileadmin/user_upload/ISER/downloads/MB_827.pdf (visited on 2020-02-27).

[114] VACUUMSCHMELZE GMBH & CO. KG. *Weichmagnetische Kobalt-Eisen-Legierungen*. Material Data Sheet. 2001. URL: https://www.sekels.de/fileadmin/PDF/Deutsch/31_Broschuere_CoFe-Legierungen__VAC_.pdf (visited on 2020-02-27).

[115] C. Clauß. "Sensorische Eigenschaften elektrodynamischer Lineardirektantriebe mit Kurzspulsystemen". PhD thesis. Universität Stuttgart, 2006.

[116] D. Pawelczak. "Nutzung inhärenter Messeffekte von Aktoren und Methoden zur sensorlosen Positionsmessung im Betrieb". PhD thesis. Universität der Bundeswehr München, 2005. URL: https://d-nb.info/975390597/34.

[117] D. Wibbing. "Wegmess-System für Miniatur-Linearmotoren (SensMiLi)". PhD thesis. Universität Stuttgart, 2012. DOI: 10.18419/opus-4512.

[118] iC-Haus GmbH. *ic-PR Series*. 2015. URL: https://www.ichaus.de/product/iC-PR%20Series (visited on 2020-02-28).

[119] L. Weidenfeller. "Kombination von zweiphotonenbasiertem direktem Laserschreiben mit großflächiger und hochpräziser Nanopositionierung". PhD thesis. Technische Universität Ilmenau, 2020.

[120] C. Lenk et al. "Nanofabrication by field-emission scanning probe lithography and cryogenic plasma etching". In: *Microelectronic Engineering* 192 (2018-05), pp. 77–82. DOI: 10.1016/j.mee.2018.01.022.

[121] S. Supreeti. "Soft Nanoimprint lithography on Curved Surfaces". PhD thesis. Technische Universität Ilmenau, 2020.

[122] J. Kirchner. "Grundlegende Entwicklungen und Untersuchungen zur Mikro- und Nanostrukturierung durch Direct Laser Writing in Nanopositionier- und Nanomessmaschinen". PhD thesis. Technische Universität Ilmenau, 2020.

[123] L. Weidenfeller, M. Hofmann, J. Kirchner, S. Supreeti, I. W. Rangelow, S. Sinzinger, and E. Manske. "Micro- and nanofabrication technologies using the nanopositioning and nanomeasuring machines". In: *Optical Measurement Systems for Industrial Inspection XI*. Ed. by P. Lehmann, W. Osten, and A. A. Gonçalves. SPIE, 2019-06. DOI: 10.1117/12.2528136.

[124] M. Hofmann, L. Weidenfeller, S. Supreeti, S. Mechold, M. Holz, C. Reuter, S. Sinzinger, E. Manske, and I. W. Rangelow. "Mix-and-match lithography and cryogenic etching for NIL template fabrication". In: *Microelectronic Engineering* 224 (2020-03), p. 111234. DOI: 10.1016/j.mee.2020.111234.

List of Figures

List of Tables

Appendix

A.1 Dimensions of the NPPS100

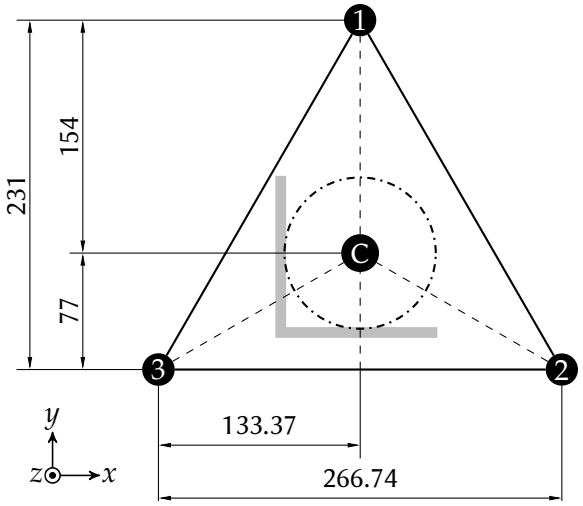

Figure A.1: Functional dimensions of the NPPS100 slider in the scale 1 : 5 in millimeters. The LAUs are numbered 1 to 3.

A.1.1 Required Resolution for the LAU-internal Measurement System

The LIFs have an angular resolution of $\pm 1.5'$ [33]. The worst case lever length l is 77 mm, see fig. A.1. Thus, the angular range $\Delta\varphi$ of $3'$ corresponds to a vertical range of:

$$\begin{aligned} \Delta z &= l \tan(\Delta\varphi) \\ \Delta z &= 67.2\,\mu\text{m} \end{aligned} \tag{A.1}$$

With a safety factor of 3 (one increment on the lower end, one increment on the high end, one in the good middle range) a required resolution of 22.4 µm is given.

A.1.2 Dynamics of a Point to Point Tilting Motion

The general accelerated rotational motion is described in [48] with:

$$\varphi(t) = \frac{\alpha}{2} t^2 \tag{A.2}$$

In the relevant application an angle φ_1 shall be reached in the time t_1 while the motion stops at φ_1. The first half of the time is accelerated, whereas the second half is deaccelerated. Assuming equal acceleration and deacceleration $\varphi_1/2$ needs to be reached in $t_1/2$.

$$\frac{\varphi_1}{2} = \frac{\alpha}{2}\frac{{t_1}^2}{2} \tag{A.3}$$

If φ_1 and t_1 are given, α equals:

$$\alpha = 4\frac{\varphi_1}{{t_1}^2} \tag{A.4}$$

A.1.3 Evaluation of Weight Force Compensation Effects

Table A.1: Evaluation of the physical WFC effects. The abbreviations stand for the following effects: *CW*: counter weight, *ME*: mechanical spring, *MA*: magnetic spring, *PN*: pneumatic. The Criteria are described in section 3.5.1.

Criteria	CW	ME	MA	PN
Transmission	−2	−1	−2	+2
Design Freedom	0	+1	+2	0
Integrability	−2	−2	−2	0
Adjustment	−2	+1	−1	−2
Energy Transformation	+2	0	0	+2
Control Complexity	−2	+2	−2	0
Manufacturing Cost	+1	0	+1	+2
$\sum$	−5	+1	−4	+4

A.1.4 Jerk of a Pneumatic Piston

To hold a mass at a fixed position the drive needs to react quickly to deviations. On the one side a fast reacting controller with a high sampling rate is necessary. But also the actuator needs to be able to build up the demanded correction forces very quickly. This force change can be characterized by the jerk, the time

derivative of the acceleration.
For this pneumatic system the jerk $j = \dddot{z}$ is derived from eq. (4.9).

$$j = \frac{A_c}{m_L}\dot{p}_c \tag{A.5}$$

To obtain $\dot{p}_c$ the ideal gas law from eq. (4.11) is derived with respect to the time t.

$$\dot{p}_c = R_S T_c \dot{\rho}_c \tag{A.6}$$

Here an isothermal process is assumed (T_c is independent of the time t). This is a reasonable approximation for investigations considering only an operating point [83]. Otherwise, an additional energy equation would be necessary. The change of the airs density $\dot{\rho}_c$ is composed of its mass and volume change, see eq. (4.12):

$$\dot{\rho}_c = \frac{\mathrm{d}}{\mathrm{d}t}\left(\frac{m_c}{V_c}\right) = \frac{\dot{m}_c h_c - m_c \dot{h}_c}{A_c {h_c}^2} \tag{A.7}$$

The continuity equation states, that the change of air mass m_c in the chamber equals the input minus the output mass flow. Here the valves feeds air into the chamber and through the leakage air is discharged from the chamber:

$$\dot{m}_c = \dot{m}_t - \dot{m}_g \tag{A.8}$$

By neglecting the transmission line effects (assuming a very short line) these two mass flows are found in eq. (4.26) and eq. (4.32). Further, m_c is replaced with eq. (4.11). This gives for $\dot{p}_c$:

$$\dot{p}_c = \frac{1}{A_c h_c}\Big(R_S T_c\Big(\dot{m}_v(u, p_c) - \dot{m}_g(p_c)\Big) - p_c A_c \dot{h}_c\Big) \tag{A.9}$$

A.1.5 State Space Representation of the Pneumatic WFC

In section 4.2.7 the state space representation for a pneumatic actuator was given with:

$$\boldsymbol{A} = \begin{pmatrix} a_{11} & a_{12} & 0 \\ a_{21} & 0 & 0 \\ 0 & 1 & 0 \end{pmatrix}, \quad \boldsymbol{B} = \begin{pmatrix} b_1 \\ 0 \\ 0 \end{pmatrix}, \quad \boldsymbol{C} = \begin{pmatrix} 0 & 0 & 1 \end{pmatrix}, \quad \boldsymbol{D} = 0 \tag{4.45}$$

The resulting transfer function is:

$$G(s) = \frac{Y(s)}{U(s)} = \frac{a_{21}b_1}{s^3 - a_{11}s^2 - a_{12}a_{21}s} \tag{4.46}$$

with

$$\begin{aligned} a_{11} &= -\frac{k_g R_S T_c}{A_c h_c^* \psi(p_c^*)} \left(2p_c^* \psi(p_c^*) + \left({p_a}^2 - {p_c^*}^2 \right) \frac{\mathrm{d}}{\mathrm{d}p_c^*} \psi(p_c^*) \right) \\ a_{12} &= -\frac{p_c^*}{h_c^*}; \qquad a_{21} = \frac{A_c}{m_L}; \qquad b_1 = \frac{k_v R_S T_c p_u}{A_c h_c^*} \psi(p_c^*) \end{aligned} \tag{A.10}$$

and the poles are:

$$p_1 = 0 \qquad p_{2,3} = \frac{1}{2} \left(a_{11} \pm \sqrt{{a_{11}}^2 + 4a_{12}a_{21}} \right) \tag{A.11}$$

For a choked flow with $p_c^*/p_u < b$, ψ from eq. (4.31) equals 1. Thus, a_{11} and b_1 simplify to:

$$a_{11} = -\frac{2k_g R_S T_c p_c^*}{A_c h_c^*}; \quad b_1 = \frac{k_v R_S T_c p_u}{A_c h_c^*} \tag{A.12}$$

Assuming subsonic flow gives:

$$\begin{gathered} a_{11} = -\frac{k_g R_S T_c}{A_c h_c^*} \frac{\Delta p_k \left({p_a}^2 - {p_c^*}^2 \right) + 2p_c^* \left(-{\Delta p_k}^2 + {p_u}^2 (b-1)^2 \right)}{-{\Delta p_k}^2 + {p_u}^2 (b-1)^2} \\ \text{with} \quad \Delta p_k = b p_u - p_c^* \end{gathered} \tag{A.13}$$

and b_1 results in:

$$b_1 = \frac{k_v R_S T_c p_u}{A_c h_c^*} \sqrt{1 - \left(\frac{\frac{p_c^*}{p_u} - b}{1 - b} \right)^2} \tag{A.14}$$

A.1.6 Jerk of a Voice Coil Drive

The available jerk j of a voice coil drive is given as:

$$j = \dot{a} \tag{A.15}$$

$$j = \frac{\dot{F}_z}{m_L} \tag{A.16}$$

With the simplified LORENTZ-force equation eq. (4.51) it is transformed to:

$$j = \frac{B_r l_w}{m_L} \dot{I}$$

The inductance of the coil is given in [48]:

$$U(t) = L\dot{I} \tag{A.17}$$

Further, the inductance of a coil in an electromagnetic circuit is given in [86]:

$$j = \frac{B_r l_w}{m_L} \frac{U}{L} \tag{A.18}$$

$$\text{with } L = N^2 G_m \tag{A.19}$$

$$j = \frac{B_r l_w}{m_L} \frac{U}{N^2 G_m} \tag{A.20}$$

where G_m is the permeance of the electromagnetic circuit [86].